

**An Evaluation of a Second Moment
Time Dependent Turbulence Model**

by
Frederick Toepfer

Department of Atmospheric Science
Colorado State University
Fort Collins, Colorado



**Department of
Atmospheric Science**

Paper No. 304

AN EVALUATION OF A SECOND MOMENT TIME DEPENDENT TURBULENCE MODEL

by

Frederick Toepfer

Research supported by the
National Science Foundation
under Grant ATM 77-09770
and Grant DES 75-13310

Department of Atmospheric Science
Colorado State University
Fort Collins, Colorado

December, 1978

Atmospheric Science Paper No. 304

ABSTRACT OF THESIS

AN EVALUATION OF A SECOND MOMENT TIME DEPENDENT TURBULENCE MODEL

The Manton-Cotton approximate equations governing dry convection are studied. These equations are numerically integrated on a horizontally homogeneous vertical finite difference grid of the planetary boundary layer. The integration is both forced and unforced by a time varying profile of surface temperature for approximately 1/2 of a diurnal cycle. The resulting profiles of mean momentum and temperature, momentum and temperature flux, and momentum and temperature variance are then studied with the dual objective of determining the capability of the model to describe the dry planetary boundary layer and to evaluate its intended objective of modelling deep tropospheric convection in a mesoscale model. Model results in the forced case are compared with observations from Day 33 of the Wangara Experiment.

Results suggest that the model does well in describing the dry planetary boundary layer, in spite of apparent inadequacies in the formulation of the unified closure assumption employing a turbulent time scale. The rate of entrainment of the inversion is underpredicted by an order of magnitude. Flux profiles couple nicely with those diagnosed by the surface layer parameterization scheme. Profiles of variance suggest that the local equilibrium assumption for the surface layer scheme may be invalid. Overall model results suggest the need for including buoyancy in the closure approximation for the turbulent

transport triple correlation products prior to extending the model to deep tropospheric convection.

Frederick Toepfer
Atmospheric Science Department
Colorado State University
Fort Collins, Colorado 80523
Summer, 1978

ACKNOWLEDGMENTS

The encouragement of Dr. William Cotton in the preparation of this work is gratefully acknowledged. Many fruitful discussions with Robert Banta were indispensable.

Ms. Kathy Malewicz did an excellent job in typing the manuscript and Ms. Lucy McCall and Ms. Bonnie Tripoli did an equally outstanding job in drafting the figures.

This work was supported under NSF Grant ATM77-09770 and NSF Grant DES75-13310.

TABLE OF CONTENTS

<u>Section</u>	<u>Page</u>
ABSTRACT OF THESIS.....	ii
ACKNOWLEDGMENTS	iv
TABLE OF CONTENTS.....	v
LIST OF FIGURES.....	vii
 <u>Chapter</u>	
1 INTRODUCTION.....	1
2 THEORETICAL DEVELOPMENT.....	5
2.1 Governing Equations.....	5
2.2 Reynolds Averaged Equations.....	7
2.2.1 Definition of Reynolds Averaging Process.....	7
2.2.2 Equations for the First Moments.....	10
2.2.3 Equations for the Second Moments.....	10
2.3 Closure of the Second Moment System.....	13
2.3.1 Dissipation.....	14
2.3.2 Pressure Correlation Terms.....	15
2.3.3 Turbulent Transport Terms.....	17
2.3.4 Turbulent Time Scale.....	21
3 EXPERIMENTAL PROCEDURE.....	23
3.1 The Horizontally Homogeneous Model.....	23
3.2 General Numerical Procedure.....	26
3.2.1 Time Differencing.....	26
3.2.2 Spatial Differencing.....	27
3.2.3 Criteria for Numerical Stability.....	29
3.3 Boundary Conditions.....	30
3.3.1 Upper Boundary Conditions.....	30

TABLE OF CONTENTS (Cont'd)

<u>Chapter</u>	<u>Page</u>
3.3.2 Lower Boundary Conditions.....	31
3.4 Calculation of the Turbulent Time Scale.....	35
4 RESULTS.....	36
4.1 Sensitivity Tests and Internal Consistency Checks...	36
4.1.1 Model Initialization.....	36
4.1.2 Calibration of Coefficients.....	37
4.2 Neutral Case Study.....	39
4.2.1 Model Initialization.....	39
4.2.2 Results of Integration.....	39
4.2.3 Discussion.....	48
4.3 Wangara Day 33 Case Study.....	55
4.3.1 Description of Day 33.....	56
4.3.2 Model Initialization.....	61
4.3.3 Results of Integration.....	64
4.3.4 Comparison with Observations and Other Simulation Studies.....	83
5 SUMMARY.....	89
5.1 Summary and Conclusions.....	89
5.2 Suggestions for Further Research.....	91
REFERENCES.....	93
APPENDIX A.....	98
APPENDIX B.....	99

LIST OF FIGURES

<u>Figure</u>	<u>Page</u>
2-1 Filtering of a component wavelength, λ due to a moving integral filter of length, H , as a function of $H\pi/\lambda$	9
3-1 Schematic depiction of the staggered grid. Mean variables are defined at the open circles; turbulent quantities are defined at the x's.....	28
4-1 The vertically averaged Turbulent Kinetic Energy (T.K.E.) and friction velocity, u_* as a function of time of integration. $\Delta_1 u_*$ and $\Delta_2 u_*$ estimate the amplitude of the damped oscillation.....	40
4-2 Vertical profiles of the turbulent kinetic energy intensity ($\text{ergs}\cdot\text{cm}^3$) at $T=12$ hours and at $T=18$ hours for neutrally stratified case study.....	42
4-3a Vertical profiles of the Turbulent Time Scale (T.T.S.) at $T=12$ hours and $T=18$ hours.....	43
4-3b Vertical profiles of the associated dissipation at $T=12$ hours for the neutrally stratified case study.....	44
4-4 Vertical profiles of the individual components of the Turbulent Kinetic Energy; $\overline{u''u''}$ (dotted), $\overline{v''v''}$ (dash-dot), and $\overline{w''w''}$ (solid), at $T=12$ hours for the neutrally stratified case study.....	45
4-5 Vertical profiles of model predicted east-west, $\rho \bar{u}$, and north-south, $\rho \bar{v}$, mean momentum per unit volume. The constant $\rho \bar{u}g$ (solid line) is also shown. $\rho \bar{v}g$ is identically zero.....	46
4-6 Vertical profiles of the vertical turbulent momentum flux at $T=12$ hours in the neutrally stratified case study.....	47
4-7 Degree of frictional turning of 100m wind as a function of time of integration for values of $z_0=1.0\text{cm}$ (dotted), $z_0=2.0\text{cm}$ (solid) and $z_0=5.0\text{cm}$ (dashed) for the neutrally stratified case study.....	49
4-8 Friction velocity, u_* , as a function of time of integration for $z_0=2.0\text{cm}$ (dotted) and $z_0=5.0\text{cm}$ (solid) for the neutrally stratified case study.....	50
4-9 Vertically averaged Turbulent Kinetic Energy (T.K.E.) as a function of time of integration for $z_0=2.0\text{cm}$ (dotted) and $z_0=5.0\text{cm}$ (solid) for the neutrally stratified case study.....	51

LIST OF FIGURES (Cont'd)

<u>Figure</u>	<u>Page</u>
4-10a Traditional Ekman spiral from first-order theory.....	52
4-10b Ekman spiral as calculated for $z_0=2.0\text{cm}$ (upper) and $z_0=5.0\text{cm}$ (lower) at $T=20$ hours for the neutrally stratified case study.....	54
4-11 Observed three-hourly vertical profiles of potential temperature, beginning at 0600LST on Day 33 of the Wangara Experiment (Clarke et. al. 1971).....	57
4-12a Observed vertical profiles of the u and v components of the mean wind at 0600 LST.....	58
4-12b Superimposed upon the 0900 profiles if the vertical profile of the geostrophic wind derived from the observed thermal wind.....	59
4-13 Observed time series of the observed surface geostrophic wind components for Day 33 of the Wangara Experiment.....	60
4-14 Variation of the diagnosed surface $\theta(z=z_0)$ and the observed screen height temperature as a function of time of integration. $t_0=0715\text{LST}$	65
4-15 Variation of the diagnosed surface heat flux (solid) and friction velocity as a function of time of integration....	66
4-16 Computed mean/momentum components at $z=50\text{m}$ as a function of time of integration for the Wangara Experiment, Day 33 simulation.....	68
4-17 Computed vertical profiles of \bar{u} at $T=5$ hours (dash-dot), $T=7.5$ hours (solid), $T=10$ hours (dotted) and $T=13.75$ hours (dashed).....	70
4-18 Same as in Figure 4-17, except for \bar{v}	71
4-19 Initial (long-dash) and computed vertical profiles of mean potential temperature, $\bar{\theta}$, at $T=2$ hours (dashed), $T=3$ hours (solid), $T=5$ hours (dash-dot), $T=8$ hours (bold-dot) and $T=11$ hours (small-dot).....	72
4-20 Computed vertical profiles of the vertical heat flux, $\overline{\theta''w''}$ at $T=3$ hours (solid), $T=5$ hours (dash-dot), $T=8$ hours (bold-dot), $T=10$ hours (small-dot) and $T=10.5$ hours (dashed).....	74

LIST OF FIGURES (Cont'd)

<u>Figure</u>	<u>Page</u>
4-21a Computed vertical profiles of turbulent momentum flux $u''w''$ at T=5 hours (dash-dot), T=8 hours (bold-dot) T=10 hours (small-dot), T=11 hours (short-dash) and T=12 hours (long dash).....	75
4-21b Computed vertical profiles of turbulent momentum flux $v''w''$ at T=5 hours (dash-dot), T=8 hours (bold-dot) T=10 hours (small-dot, T=11 hours (short=dash) and T=12 hours (long dash).....	76
4-22 Same as in Figure 4-21 except for the Turbulent Kinetic Energy, $\rho_0 q^2$	78
4-23 Predicted profiles of the vertical velocity variance, $\overline{w''w''}$ (dashed) and horizontal velocity variance, $(\overline{u''u''} + \overline{v''v''})/2$ at T=5 hours (lowest maximum), T=8 hours (middle maximum) and T=11 hours (highest maximum).....	79
4-24 Computed profiles of temperature variance, $\overline{\theta''\theta''}$ at T=5 hours (dash-dot), T=8 hours (dotted), T=10 hours (dashed) and T=11 hours (solid).....	81
4-25 Computed profiles of the turbulent time scale at T=5 hours (dash-dot), T=8 hours (bold-dot), T=10 hours (small dot) T=11 hours (short-dashed), T=12 hours (long dashed) and T=14 hours (solid).....	82
4-26 Hourly variation of the computed and observed surface heat flux as a function of time of Day 33; dashed line, Deardorff (1974); thin-solid line, observed; dotted, Yamada and Mellor (1975); and bold solid line, this study.....	84

1. INTRODUCTION

Atmospheric flow regimes are governed by a system of equations which are not tractable in their full form, either analytically or numerically. Research has followed a dual approach: (1) Formulate the equations in some approximate form in order to eliminate the non-linear aspects of the problem under study thereby making it analytically tractable; or (2) try to exact a solution via the more brute force method utilizing finite difference techniques on a computer. Each method alone, and more often together, has been used to a reasonable degree of success for laminar flow regimes. Atmospheric flows, however, are often times characterized by high Reynolds number, and with high Reynolds number flow, turbulence can and most often does play a major role in the transport and mixing properties of the flow.

The attempt to directly simulate turbulent flows computationally has led researchers to realize that computational costs are prohibitive. This is especially true when one attempts to model the intermediate meteorological scales. Modelling a mesoscale system containing deep tropospheric convection where a coupling of all the different scales of motion and kinetic energy generation is apparent would be a Herculean task if direct simulation of the turbulent flow structure were to be used. Practical considerations require that a grid scale be used lying within the energy-containing scales of the turbulence structure. In an attempt to deal with this, and other problems of a similar nature, atmospheric researchers have chosen to follow the lead of physicists when confronted with a similar problem. They have chosen to conceptually think of turbulent flows as stochastic in nature. The concept of treating

turbulent flows as some random process occurring about a quantifiable, deterministic or mean state has proven useful in discerning the character of the turbulence. In the stochastic interpretation, a flow variable is denoted $\phi(\underline{x}, t; \alpha)$ (Dutton, 1976) where α is a random variable. Then $p(\alpha)$ would denote the probability of a particular value of α . Since functions of random variables are themselves random, the flux variables can be considered stochastic; that is, a variable whose value in space and in time is describable in terms of some probability density function. Then, in terms of modelling, one can think of predicting the moments of the distributions of the variables. The effect of turbulence on the larger atmospheric systems is felt only through the statistical properties of the turbulence, much in the same way, that temperature at some point is a statistical measure of molecular kinetic energy in a gas.

The stochastic approach to modelling atmospheric flow regimes has been widely used for many years on all scales of motion, including the global. However, most have been restricted to time dependency of the first order moments, and use what is hoped to be suitable models for the second moments. Physically, if one tries to model a system where observations show a generation of turbulent kinetic energy on scales of motion which are large and a cascade of this energy through smaller and smaller scales to be dissipated by viscosity, this approach (Tennekes, 1978) is both economical and practical (if not valid) and models the essential nature of the turbulence - i.e., dissipation of kinetic energy. However, there are atmospheric phenomena where energy is generated on small scales which in turn amplify, and one observes energy appearing in larger and larger scales of motion. No method as of yet has been

devised which will relate the second moments of the variables and allow for this upscale transport of energy. To quote Lumley: "No good direct model of second order turbulence quantities exists".

It is the claim of Lumley and Khajer-Nouri (1974) that while it is not possible to construct a rational model of the second moments, it is possible for the higher moments. But the added complexity presents new obstacles. Consider a simple dry system described by five variables: u , v , w , p , T . A fully time-dependent system of equations describing the behavior in time of the first moments of these variables would consist of five equations, namely one each for $E(u)$, $E(v)$, $E(w)$, $E(p)$, and $E(T)$. A fully time dependent system for the first and second moments would consist of 20 equations, describing the behavior of the means, variances, and covariances of the five variables. If the system is complicated further by adding an additional variable (e.g., water vapor), an additional seven equations are necessary - two for the first two moments of the new variables and five for the covariances of the new variable with the old variables. And still, the system is not closed. Some suitable model is necessary for the third moments which occur. A number of researchers have felt it necessary for their own purposes to carry the exact time dependent equations for the second moments, and model third order terms (Donaldson, 1972, 1973; Daly and Harlow, 1970; Ng and Spaulding 1972; Mellor, 1974; Wyngaard and Cote, 1974; Cotton, 1975c; Manton and Cotton, 1977b).

The majority of researchers investigating higher order turbulence closure theory have done so with the objective of modelling the dry planetary boundary layer. Others have modelled with the objective of

parameterizing turbulence on the sub-grid scale of high-resolution cumulus models, e.g., Sommeria and Deardorff (1977), or Lipps (1977). Manton and Cotton (1977) on the other hand, have formulated a higher-order turbulence model with the intended application of parameterizing the whole cellular structure of convection embedded within explicitly modelled mesoscale disturbances. Presently formulated convective parameterization schemes e.g., Arakawa and Schubert, (1974); Betts, (1973); Ooyama (1971), have been designed to parameterize convection in general circulation and synoptic scale models where there exists a large scale-separation between the explicitly modelled scales and the parameterized scales. No such scale separation exists between the mesoscale and cumulus scale, since cumulus clouds often amalgamate and merge to become mesoscale systems in their own right. Further, present convective parameterization schemes crudely, if at all, consider the vertical transport of horizontal momentum, by cumulus clouds.

The Manton-Cotton theory was thus proposed as an alternate approach to convective parameterization. This research is, therefore, a first attempt at evaluating the Manton-Cotton theory. The evaluation is done using the framework of a dry, horizontally-homogeneous planetary boundary layer (P.B.L.). It is attempted to evaluate the ability of the model to represent a dry, horizontally-homogeneous P.B.L. as well as its extension to the more general problem for which it was intended.

2. THEORETICAL DEVELOPMENT

2.1 Governing Equations

The basic model equations are as given in Manton and Cotton (1977a). Building upon previous work by Ogura and Phillips (1962) and Dutton and Fichtl (1969), Manton and Cotton have derived an approximate set of equations which are intended to be used to model deep tropospheric convection. This system of equations has a linearized equation of state and a hydrostatic, dry, horizontally homogeneous thermodynamic reference state. The system itself is anelastic and solenoidal. Implicit in the derivation of this system is the physical assumption that acoustic modes contribute little to the overall energetics of buoyancy driven systems and can be systematically neglected. Neglecting water, the basic system is

$$\frac{\partial m_i}{\partial x_i} = 0 \quad (2.1)$$

$$\frac{\partial m_i}{\partial t} + \frac{\partial}{\partial x_j} (u_j m_i) - \epsilon_{ijk} f_k m_j + \frac{\partial p'}{\partial x_i} + \rho' g \sigma_{i3} = \rho_0 v_m \nabla^2 u_i \quad (2.2)$$

$$\frac{\partial r}{\partial t} + \frac{\partial}{\partial x_j} (u_j r) + m_3 \frac{\partial}{\partial x_3} \ln \theta_0 = v_0 \nabla^2 r \quad (2.3)$$

where $m_i = \rho_0 u_i$, the momentum per unit volume; f_i is the coriolis frequency vector; $r = \frac{\rho_0 \theta'}{\theta_0}$, the potential density. $\rho_0, \theta_0, p_0, T_0$ are related by

$$\frac{\partial p_0}{\partial x_3} = -\rho_0 g \quad (2.4)$$

$$\frac{p'}{p_o} = \frac{T'}{T_o} + \frac{\rho'}{\rho_o} \quad (2.5)$$

$$\theta_o = T_o \left(\frac{P_r}{p_o} \right)^{R/c_p} \quad (2.6)$$

$$p_o = \rho_o R T_o \quad (2.7)$$

$$\frac{\theta'}{\theta_o} = \left(1 - \frac{R}{c_p} \right) \frac{p'}{p_o} - \frac{\rho'}{\rho_o} \quad (2.8)$$

where g , R , c_p , P_r have their usual meaning. (x_1, x_2, x_3) define a cartesian co-ordinate system in the usual meteorological directions, north, east and up. Equation (2.8) leads to the statement that ρ' and r are related by:

$$\rho' = \left(1 - \frac{R}{c_p} \right) \frac{p' \rho_o}{p_o} - r \quad (2.9)$$

The subscript o denotes a base or reference state for the thermodynamic variables. The reference state is an arbitrary one, constrained only by the equation of state and the hydrostatic approximation.

The stochastic thermodynamic variable is given by $T = T_o + T'$, or simply $T' + \text{constant}$, since T_o is specified as a known function of z . The linearized equation of state is given by

$$\frac{p'}{p_o} = \frac{\rho'}{\rho_o} + \frac{T'}{T_o} \quad (2.10)$$

where the cross term $\frac{T' \rho'}{\rho_o T_o}$ has been neglected.

2.2 Reynolds Averaged Equations .

2.2.1 Definition of Reynolds Averaging

In the stochastic interpretation, the desire is to describe predictively in time the trends of the flow variables. It is necessary, then, to take the expected values of the predictive flow variables. However, since the probability density functions of the variables are unknown, it is convenient to define expected values in the following manner:

$$E[u(x,y,z,t)] = \frac{1}{N} \sum_{n=1}^N \frac{1}{\tau KLM} \int_{t-\frac{\tau}{2}}^{t+\frac{\tau}{2}} \int_{x-\frac{K}{2}}^{x+\frac{K}{2}} \int_{y-\frac{L}{2}}^{y+\frac{L}{2}} \int_{z-\frac{M}{2}}^{z+\frac{M}{2}} u(x_1', x_2', x_3', t') dx_1' dx_2' dx_3' dt' \quad (2.11)$$

In contrast to Deardorff (1969), the proper interpretation of K, L, and M are scale lengths; τ is an experimentally defined time scale; and N represents the number of sample observations over the space-time domain. The expected value of the stochastic flow variable defined in the above is an ensemble average. Denoting $E[u_i]$ as \bar{u}_i , and following the notation of Manton and Cotton, u_i can be expressed

$$u_i = \bar{u}_i + u_i'' = E(u_i) + u_i'' \quad (2.12)$$

It follows directly then, that:

$$E \left[\frac{\partial u_i}{\partial x_k} \right] = \frac{\partial}{\partial x_k} E[u_i] \quad (2.13)$$

$$E \left[\frac{\partial u_i}{\partial t} \right] = \frac{\partial}{\partial t} E[u_i] \quad (2.14)$$

$$E [u_i''u_j''] = \text{cov} [u_i u_j] \quad (2.15)$$

Equation (2-15) can be shown by:

$$\begin{aligned} \text{cov}[u_i u_j] &= E[u_i u_j] - E[u_i]E[u_j] \\ &= E[(u_i - \bar{u}_i)(u_j - \bar{u}_j)] \\ &= E[u_i''u_j''] \end{aligned} \quad (2.16)$$

It should be noted here that $E(u_i)$ defined in such a manner works as a low pass filter. Consider the simplest case of a one dimensional time series at a point or a spatial cross-section at some instant in time. It is possible to describe that time series or cross-section by its Fourier representation: $u(x) = Ae^{ikx}$. Then

$$\begin{aligned} E[u(x)] &= A \frac{1}{L} \int_{x - \frac{L}{2}}^{x + \frac{L}{2}} e^{ikx'} dx' = \frac{A}{Lki} [e^{ik(x + \frac{L}{2})} - e^{ik(x - \frac{L}{2})}] \\ &= \frac{-iA}{Lk} [e^{ik \frac{L}{2}} - e^{-ik \frac{L}{2}}] e^{ikx} \\ &= \frac{-i2}{Lk} \sin h(i k L/2) u(x) \\ &= \frac{2}{Lk} \sin (kL/2) u(x) \\ &= \frac{\sin A}{A} u(x), \text{ where } A = \left(\frac{TiL}{\lambda}\right)\pi \end{aligned} \quad (2.17)$$

As is shown in Figure 2-1, the filter passes 65% of the contribution due to $\lambda = 2H$, 90% of $\lambda = 4H$, 99% of $\lambda = 10H$; filters 100% of $\lambda = H$, $H/2$, $H/3$. For values of λ , that are not eigenvalues of H , the filter filters for values of $\lambda < H/2$ more than 85% of the contribution due to that wavelength.

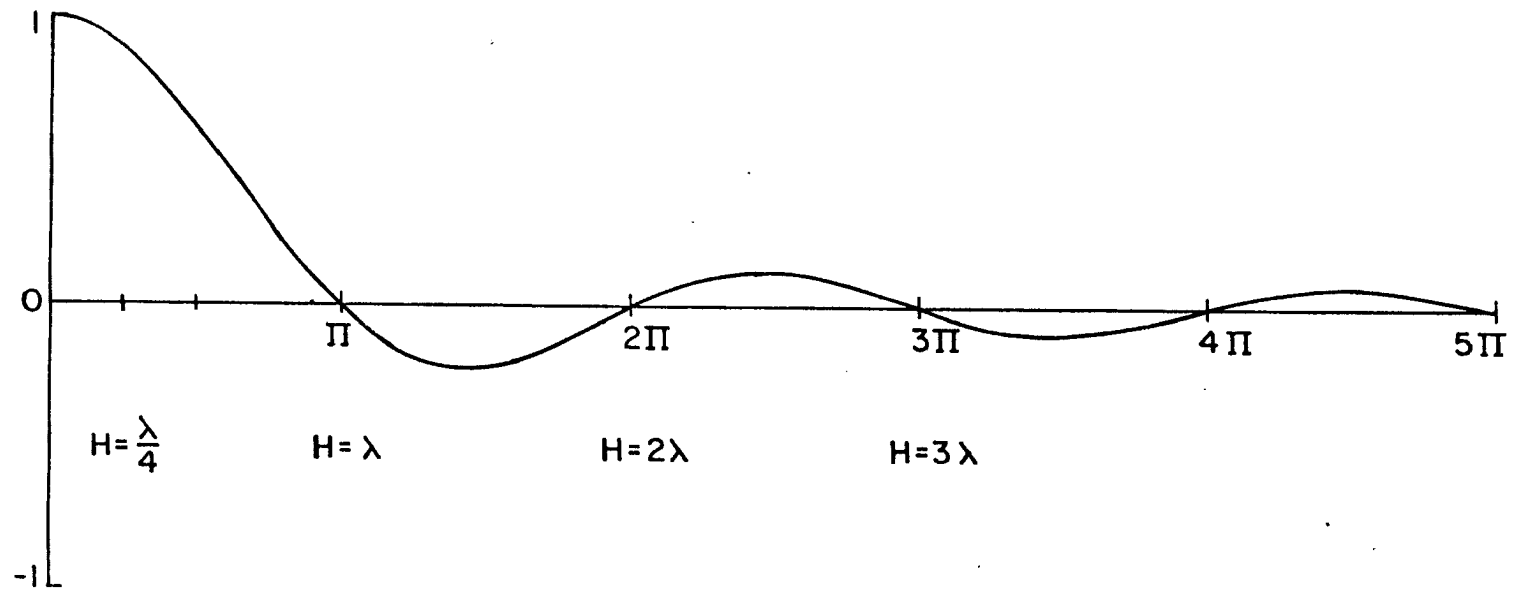


Figure 2-1. Filtering of a component wavelength, λ due to a moving integral filter of length, H , as a function of $H\pi/\lambda$.

2.2.2 Equations for the First Moments

Applying the Reynolds Averaging operator, defined in the previous section, the equations for the first moments can be written:

$$\frac{\partial}{\partial x_j} \bar{m}_j = 0, \quad (2.18)$$

$$\frac{\partial \bar{m}_i}{\partial t} + \frac{\partial}{\partial x_j} \bar{m}_i \bar{u}_j + \frac{\partial}{\partial x_j} \overline{m_i'' u_j''} - \epsilon_{ijk} f_k \bar{m}_j - \frac{\partial \bar{p}'}{\partial x_i} + \bar{\rho}' g \delta_{i3} \quad (2.19)$$

= 0,

$$\frac{\partial \bar{r}}{\partial t} + \frac{\partial}{\partial x_j} \bar{r} \bar{u}_j + \frac{\partial}{\partial x_j} \overline{r'' u_j''} + \bar{m}_3 \frac{\partial}{\partial x_3} \ln \theta_0 = 0 \quad (2.20)$$

where the bar operator denotes expected value, and the effective molecular viscosity has been neglected. $E(u_i u_j)$ has been written $E(u_i)E(u_j) + \text{cov}(u_i u_j)$. If it were possible, to express the $\text{cov}(u_i u_j)$ as known functions of $E(u_i)$ and $E(u_j)$, the system would be closed. In order to close the system, therefore, the development of a system of equations for the second moments is now done.

2.2.3 Equations for the Second Moments

Because the intended application of this model, (i.e., the modeling of atmospheric systems where strong kinetic energy generation is taking place on scales of motion contributing strongly to the $\text{var}[u_i]$), Manton and Cotton have developed a fully time-dependent system for the second moment system. Other researchers, e.g., Mellor and Yamada, 1974, have developed modified systems, with some degree of approximation. However, because closure is applied at higher-orders, the general time dependent system includes equations for the variances and covariances

of the dependent variables. The derivation of this system is lengthy and will not be included here. This system is given in Manton and Cotton (1976) as follows:

$$\begin{aligned}
& \frac{\partial}{\partial t} (\overline{u_k''m_i''}) + \frac{\partial}{\partial x_j} (\bar{u}_j \overline{u_k''m_i''}) - [\epsilon_{ijn} f_n \overline{m_j''u_k''} + \epsilon_{kjn} f_n \overline{m_j''u_i''}] \\
& + \overline{m_k''u_j''} \frac{\partial}{\partial x_j} \bar{u}_i + \overline{m_i''u_j''} \frac{\partial}{\partial x_j} \bar{u}_k \\
& + \rho_0 \frac{\partial}{\partial x_j} (\overline{u_i''u_j''u_k''}) + \frac{\partial}{\partial x_k} (\overline{p''u_i''}) + \frac{\partial}{\partial x_i} (\overline{p''u_k''}) \\
& - \overline{p'' \left(\frac{\partial}{\partial x_i} u_k'' + \frac{\partial}{\partial x_k} u_i'' \right)} + \overline{g(\rho''u_i'') \delta_{k3}} + \overline{g(\rho''u_k'') \delta_{i3}} \\
& = -2\rho_0 v_m \overline{\left(\frac{\partial}{\partial x_j} u_i'' \right) \left(\frac{\partial}{\partial x_j} u_k'' \right)}, \tag{2.21}
\end{aligned}$$

$$\begin{aligned}
& \frac{\partial}{\partial t} (\overline{u_i''r''}) + \frac{\partial}{\partial x_j} (\bar{u}_j \overline{u_i''r''}) - \epsilon_{ijk} f_k \overline{u_j''r''} + \overline{r''u_j''} \frac{\partial \bar{u}_i}{\partial x_j} \\
& + \overline{u_i''u_j''} \frac{\partial \bar{r}}{\partial x_j} + \overline{u_i''m_3''} \frac{\partial}{\partial x_3} (\ln \theta_0) + \frac{\partial}{\partial x_j} (\overline{u_j''u_i''r''}) + \left(\frac{1}{\rho_0} \right) \frac{\partial \overline{p''r''}}{\partial x_i} \\
& - \left(\frac{1}{\rho_0} \right) \overline{p''} \frac{\partial \bar{r}}{\partial x_i} + \left(\frac{g}{\rho_0} \right) \overline{p''r''} \delta_{i3} = - (v_m + v_\theta) \overline{\left(\frac{\partial u_i''}{\partial x_j} \right) \left(\frac{\partial r''}{\partial x_j} \right)} \tag{2.22}
\end{aligned}$$

$$\begin{aligned}
& \frac{\partial}{\partial t} \overline{r''r''} + \frac{\partial}{\partial x_j} (\bar{u}_j \overline{r''r''}) - \overline{r''r''} \bar{u}_3 \frac{\partial}{\partial x_3} (\ln \rho_o) + 2 \overline{r''u_j''} \frac{\partial \bar{r}}{\partial x_j} \\
& + 2 \overline{r''m''}_3 \frac{\partial}{\partial x_3} \ln \theta_o + \frac{\partial}{\partial x_j} (\bar{u}_j \overline{r''r''}) = -2v_o \overline{\left(\frac{\partial r''}{\partial x_j}\right) \left(\frac{\partial r''}{\partial x_j}\right)} \quad (2.23)
\end{aligned}$$

where:

$$\overline{u_i''m_k''} = \overline{u_k''m_i''} = \rho_o \overline{u_i''u_k''} = \rho_o \overline{u_k''u_i''} ; \quad (2.24a)$$

$$\overline{\rho''u_i''} = - \overline{r''u_i''} \quad (2.24b)$$

and,

$$\overline{\rho''r''} = - \overline{r''r''} \quad (2.24c)$$

It must be stated that in the derivation of this system, that turbulent fluctuations are assumed to behave incompressibly; i.e.,

$$\frac{\partial u_i''}{\partial x_i} \equiv 0 ; \quad (2.25)$$

and that turbulent fluctuations of pressure can be neglected when compared with turbulent fluctuations of density, i.e.,

$$\frac{\rho_o}{\theta_o} \theta'' + \rho'' = 0 \quad (2.26a)$$

or

$$r'' = -\rho'' . \quad (2.26b)$$

By contracting i and k in equation (2.21), we can form an equation for the turbulent kinetic energy:

$$\begin{aligned}
& \frac{\partial}{\partial t} \overline{\rho_o u_i'' u_i''} + \frac{\partial}{\partial x_j} (\overline{u_j} \overline{\rho_o u_i'' u_i''}) + 2 \overline{\rho_o u_i'' u_j''} \frac{\partial}{\partial x_j} \overline{u_i} \\
& + \overline{\rho_o} \frac{\partial}{\partial x_j} (\overline{u_i'' u_i'' u_j''}) + 2 \frac{\partial}{\partial x_i} \overline{p'' u_i''} - 2 \overline{p''} \frac{\partial u_i''}{\partial x_i} + 2 \overline{g \rho'' u_i''} \delta_{i3} \\
& = -2 \overline{\rho_o v_m} \frac{\partial u_i''}{\partial x_j} \frac{\partial u_i''}{\partial x_j} \quad (2.27a)
\end{aligned}$$

By defining $\overline{q^2} = \overline{u_i'' u_i''}$, this can be written

$$\begin{aligned}
& \frac{\partial}{\partial t} (\overline{\rho_o \frac{q^2}{2}}) + \frac{\partial}{\partial x_j} (\overline{u_j} \overline{\rho_o \frac{q^2}{2}}) + \overline{\rho_o u_i'' u_j''} \frac{\partial}{\partial x_j} \overline{u_i} + \overline{\rho_o} \frac{\partial}{\partial x_j} \overline{u_j''} \frac{q^2}{2} \\
& + \frac{\partial}{\partial x_i} \overline{p'' u_i''} - \overline{p''} \frac{\partial u_i''}{\partial x_i} + \overline{g \rho'' w''} = - \overline{\rho_o v_m} \left(\frac{\partial u_i''}{\partial x_j} \right) \left(\frac{\partial u_i''}{\partial x_j} \right) \quad (2.27b)
\end{aligned}$$

To close the system; a closure approximation can now be made, specifically upon the third order moments of the dependent variables and pressure velocity correlations appearing in the time dependent equations for the second order moments.

2.3 Closure of the Second Moment System

Closure of the second moment system has been an area of strong research efforts in recent years. The absence of any good model for second moments of flow variables has been the primary motivation for this research (Lumley and Khajeh-Nouri, 1974). Generally, closure at any level is based upon modeling in an insightful way the physical consequences of each term together with some unifying closure assumption. The unifying closure assumption most typically involves

the postulation of a time scale or scales and/or some length scale or scales. It must be emphasized here that while some methods of higher level closure have gained fairly widespread acceptance in recent years, others remain controversial. Because of the intended application of the theory, Manton and Cotton have attempted to keep the number of prognostic variables to a minimum, therefore the theory must be considered to be a compromise between the more general theory of Lumley and Tennekes and Donaldson, etc.

2.3.1. Dissipation

Terms containing derivatives within the correlation correspond to the dissipation scales, while terms containing derivatives external to the correlation correspond to energy containing scales. Tennekes and Lumley (1972) claim that the energy containing range of eddies have a characteristic frequency given by u'/ℓ , where $\bar{\epsilon} = u'^3/\ell$, $3u'^2 = 2q^2$, $\bar{\epsilon}$ is the mean dissipation of kinetic energy per unit mass and ℓ' is a length scale. Therefore Manton and Cotton model dissipation thusly:

$$2\nu_m \overline{\left(\frac{\partial u_i''}{\partial x_j}\right) \left(\frac{\partial u_k''}{\partial x_j}\right)} = \left(\frac{1}{3} \frac{q^2}{T_1}\right) \delta_{ik} \quad (2.28)$$

where T_1 is proportional to the external time scale of the turbulence. The formulation of T is given in Section 2.3.4. Here it must be noted that other authors (eg., Lumley and Khajeh-Nouri (1974), Wyngaard et al (1974); Wyngaard and Cote (1974)) use the above formulation as a definition for the characteristic frequency or time scale of the turbulence, and carry through time dependent equations for the dissipation. Manton and Cotton in contrast have developed

their own ad hoc formulation for the time scale of the turbulence use the Tennekes and Lumley relation to define the dissipation. Manton and Cotton assume that dissipation of turbulence occurs at scales small enough for local isotropy to apply but that the rate is controlled by the mean strain rate. Similarly Manton and Cotton take

$$\overline{\left(\frac{\partial u_i''}{\partial x_j}\right)\left(\frac{\partial r''}{\partial x_j}\right)} = 0; \quad (2.29a)$$

$$2\nu_0 \overline{\left(\frac{\partial r''}{\partial x_j}\right)\left(\frac{\partial r''}{\partial x_j}\right)} = \frac{\overline{r''r''}}{T^2} \quad (2.29b)$$

2.3.2 Pressure Correlation Terms

Following Mellor (1973), the term $\left(u_i'' \frac{\partial p''}{\partial x_k} + u_k'' \frac{\partial p''}{\partial x_i}\right)$ is rewritten

$$\frac{\partial u_k'' p''}{\partial x_i} + \frac{\partial u_i'' p''}{\partial x_k} - p'' \left(\frac{\partial u_i''}{\partial x_k} + \frac{\partial u_k''}{\partial x_i}\right) \quad (2.30a)$$

Upon contraction this becomes

$$\frac{2\partial}{\partial x_i} \overline{u_i'' p''} - 2p'' \frac{\partial u_i''}{\partial x_i}, \quad (2.30b)$$

and considering the nondivergent character of the turbulent motions, it is seen that the remaining term is a transport term. Therefore, the term, $-p'' \left(\frac{\partial u_i''}{\partial x_k} + \frac{\partial u_k''}{\partial x_i}\right)$ was called the "energy redistribution term" by Rotta (1951), which he showed can be modeled simply by

$$-p'' \left(\frac{\partial u_i''}{\partial x_k} + \frac{\partial u_k''}{\partial x_i}\right) = \left(\frac{\rho_0}{\tau_i}\right) \overline{(u_i'' u_k'')} - \frac{\overline{q}}{3} \delta_{ik} \quad (2.31)$$

Following Manton and Cotton, the reasoning is simply that the action of pressure fluctuations against the fluctuating rate of strain causes the turbulence to approach a state of isotropy. Lumley and Khajeh-Nouri on the other hand model the pressure correlation thusly:

$$\overline{u_k'' \frac{\partial p''}{\partial x_i}} + \frac{\overline{u_i \partial p''}}{\partial x_k} - \frac{2}{3} \frac{\partial}{\partial x_i} \overline{p'' u_j''} \delta_{ik} = F_{ik} (\overline{u_i'' u_k''}, \overline{\theta'' u_i''}, \bar{\epsilon}, \frac{g}{\theta_0}) \quad (2.32)$$

where F_{ik} denotes a functional. This formulation speculates that there are buoyancy and heat flux considerations in addition to the isotropic tendencies necessary in modeling this term. Whether this is so is hard to say, however when the analogous reasoning is carried over to the modeling of the analogous term in the heat flux equation, Wyngaard and Cote (1974) claim that a second term made up of the product of the mean buoyancy $\frac{g}{\theta_0}$ and the θ - variance is necessary under strongly unstable conditions. Lumley and Khajeh-Nouri would model

$$-\overline{\theta'' \frac{\partial p''}{\partial x_i}} = F_i (\overline{\theta'' u_i''}, \overline{u_i'' u_j''}, \frac{g \overline{\theta'' \theta''}}{\theta_0}, \frac{g}{\theta_0}, \bar{\epsilon}) \quad (2.33)$$

Wyngaard and Cote claim that only the first and third arguments of the functional are important. Manton and Cotton follow the argument that the proper formulation is to write

$$-\overline{r'' \frac{\partial p''}{\partial x_i}} = \frac{-\partial}{\partial x_i} \overline{p'' r''} + \overline{p'' \frac{\partial r''}{\partial x_i}} \quad (2.34)$$

and then analogous to Rotta and Mellor model :

$$\overline{p'' \frac{\partial r''}{\partial x_i}} = \frac{1}{\tau_2} \overline{r'' u_i''} \quad (2.35)$$

Wyngaard and Cote (1974) model

$$\overline{\theta'' \frac{\partial p''}{\partial x_i}} = \frac{c_1}{\tau} \overline{\theta'' u_i''} + c_2 \frac{g}{T} \overline{\theta'' \theta''} , \quad (2.36)$$

justifying the additional term incorporating the buoyancy with the claim that under strongly unstable conditions, in the lowest few hundred meters of the atmosphere, the approximate balance

$$\frac{c_1}{\tau} \overline{\theta'' w''} \cong \frac{g}{T} \overline{\theta'' \theta''} - \overline{w'' w''} \frac{\partial \bar{\theta}}{\partial z} \quad (2.37)$$

is forced. Then when the constant c_1 is properly calibrated, balance is brought about by a change in sign in $\frac{\partial \bar{\theta}}{\partial z}$ in the lowest few hundred meters. Results with this model lend some justification to the above arguments.

2.3.3 Turbulent Transport Terms

The remaining terms to model are the turbulent transport terms, namely:

$$\rho_o \frac{\partial}{\partial x_j} \overline{(u_i'' u_k'' u_j'')} + \frac{\partial}{\partial x_k} \overline{(p'' u_i'')} + \frac{\partial}{\partial x_i} \overline{(p'' u_k'')} \quad (2.38a)$$

$$\text{and, } \frac{\partial}{\partial x_j} \overline{(u_i'' r'' u_j'')} + \frac{1}{\rho_o} \frac{\partial}{\partial x_i} \overline{p'' r''} \quad (2.38b)$$

$$\text{and, } \frac{\partial}{\partial x_j} \overline{(u_j'' r'' r'')} . \quad (2.38c)$$

These result as a natural consequence of the non-linearity of the system; and are probably the least understood and most widely debated in the literature.

It should be noted that Lumley's formulation of the transport term is slightly different due to his modeling a different form of the pressure correlation term. Also Mellor (1973) neglects $\frac{\partial}{\partial x_i}(\overline{p''u_i''})$, and $\frac{\partial}{\partial x_i} \overline{p''\theta''}$ on the basis of an assertion by Hanjalic and Launder (1972), that they are small in the first place. However Manton and Cotton imply that the pressure-velocity correlation dominates in (2.30), by modeling (2.30) as:

$$\begin{aligned} & \rho_o \frac{\partial}{\partial x_j} \overline{u_i'' u_k'' u_j''} + \frac{\partial}{\partial x_k} \overline{p'' u_i''} + \frac{\partial}{\partial x_i} \overline{p'' u''_k} \\ &= \frac{1}{3} c_1 \delta_{ik} \frac{\partial}{\partial x_j} (q^2_T \frac{\partial}{\partial x_j} (\rho_o \overline{q^2})) \end{aligned} \quad (2.39)$$

This corresponds essentially to a diffusion of $\rho_o \overline{q^2}$, the turbulent kinetic energy, with an effective diffusivity of $c_1 \overline{q^2_T}$. Following similar reasoning the remaining terms are then modeled:

$$\frac{\partial}{\partial x_j} \overline{u_i'' u_j'' r''} + \frac{1}{\rho_o} \frac{\partial}{\partial x_i} \overline{p'' r''} = 0 \quad (2.40a)$$

$$\frac{\partial}{\partial x_j} \overline{u_j'' r'' r''} = - c_2 \frac{\partial}{\partial x_j} (\overline{q^2_T} \frac{\partial \overline{r'' r''}}{\partial x_j}) \quad (2.40b)$$

The formulation for the transport of the θ -variance is essentially identical to that of Mellor (1973), Mellor and Yamada (1974), Wyngaard et al (1974) and Wyngaard and Cote (1974). However, the model of the transport of the variances and co-variances of

momentum and the co-variances of momentum and temperature is much simplified. Insisting only that his model have the same general tensor properties, Mellor (1973) chose

$$\overline{u_i'' u_j'' u_k''} = -g\lambda \left[\frac{\partial}{\partial x_k} (\overline{u_i'' u_j''}) + \frac{\partial}{\partial x_j} (\overline{u_i'' u_k''}) + \frac{\partial}{\partial x_i} (\overline{u_j'' u_k''}) \right] \quad (2.41a)$$

which would lead to terms when $i = k$, (for example w -variance)

$$\frac{\partial}{\partial x_j} (\overline{u_j'' w'' w''}) = g \frac{\lambda \partial}{\partial x_j} \left(\frac{2\partial}{\partial z} \overline{u_j'' w''} + \frac{\partial}{\partial x_j} \overline{w'' w''} \right). \quad (2.41b)$$

For $\overline{u_i'' u_j'' \theta''}$, Mellor chose

$$\overline{u_i'' u_j'' \theta''} = -q\lambda^2 \left(\frac{\partial u_i'' \theta''}{\partial x_j} + \frac{\partial u_j'' \theta''}{\partial x_i} \right) \quad (2.42a)$$

which leads to an expansion (e.g., for the heat flux $\overline{-w'' \theta''}$)

$$\frac{\partial}{\partial x_j} (\overline{u_j'' w'' \theta''}) = -\frac{\partial}{\partial x_j} q\lambda^2 \left(\frac{\partial}{\partial x_j} \overline{w'' \theta''} + \frac{\partial}{\partial z} \overline{u_j'' \theta''} \right) \quad (2.42b)$$

Wyngaard and Coté (1974) use a simple ad hoc gradient diffusion model for all co-variances and variances. Note, that in Mellor's formulation above, if T is written $\frac{q}{\lambda}$, K , the effective diffusivity can be written $\frac{q^2}{c_i} T$ where $c_i = \frac{\lambda_i}{\lambda}$. Thus, the alternate formulation of K is essentially identical to Manton and Cotton.

Lumley and Khajeh-Nouri (1974) as part of their third order closure model postulate a functional relationship, in a similar manner as for the pressure correlation terms, for the turbulent transport terms or triple correlation products. Zeman and Lumley

(1976) have developed what is essentially a diagnostic scheme for the triple correlation products from application of a local equilibrium assumption applied to the time dependent set of equations for the turbulent transport terms. Their results show essentially that in the unstable environment and near the inversion, that buoyancy terms in the modeling of the turbulent transport are necessarily present and of some importance.

Zeman and Tennekes (1977) in a later article present an argument by Tennekes (1970) that

$$-\frac{\partial}{\partial z} \left(\frac{q^2 w''}{Z} \right) + \frac{1}{\rho} \overline{p'' w''} \Big|_{z=z_I} = c_F \frac{w_*^3}{h}$$

where

$$c_F = \frac{\overline{(\theta'' w'')}_{z=z_i}}{\overline{(\theta'' w'')}_{z=z_o}}$$

This is essentially the jump model formulation (e.g., Ball 1960; Lilly, 1968; Deardorff et al, 1969; Carson, 1973; Betts (1973), Tennekes, 1973), where w_* and w are scaling parameters and the downward heat flux at the inversion base is taken to be a fixed fraction of the surface heat flux. It is the claim of the above authors that the principal gain term in the kinetic energy budget at the base of an inversion capping a well-mixed layer is the turbulent transport term (and is only partially offset by the pressure divergence). The above formulation of Tennekes shows that the negative heat flux at the base of the inversion is proportional to the turbulent transport. Therefore, a careful modeling of the turbulent transport with an eye toward the physical processes is an absolute must for any turbulence model attempting to simulate buoyancy driven turbulence in a stratified atmosphere.

2.3.4 Turbulent Time Scale

Closure assumptions in this kind of system; and often in the first order system (e.g. Smagornisky 1963; Cotton, 1975) always involve the use of some physical characteristic of the fluid in an attempt to unify the closure into a physically coherent system. Higher order closure theory most often uses the postulation of a physically realizable length or height or time scale of the turbulent system. Manton and Cotton have chosen to use a characteristic time scale of the turbulence proportional to the rate of viscous dissipation of turbulent kinetic energy controlled by the mean strain rate of the fluid. Then in order to account for the effect of mean stratification, this mean strain derived time scale is modified by a dimensionless function of the flux Richardson number. Thus, the formulation is as follows:

$$\frac{1}{T^2} = \left(\frac{\partial \bar{u}_i}{\partial x_j} \right) \left(\frac{\partial \bar{u}_i}{\partial x_j} \right) \cdot \psi^2 (\eta)$$

where η is defined by

$$\eta = \frac{-\overline{\rho'' u''_3}}{m_i'' u_j'' \frac{\partial \bar{u}_i}{\partial x_j}} \cdot g$$

and is seen to be the ratio of the production terms of turbulent kinetic energy by buoyancy to the mechanical production terms. The exact functional form used in the model of ψ^2 has been inferred

from the surface layer observations of So and Mellor (1972) and Klebanoff (1955); and Wyngaard et. al. (1971). This function is given as:

$$\psi^2(\eta) = \begin{cases} 1-3.85\eta, & \eta \leq 0 \\ \exp(-3.91\eta), & \eta > 0 \end{cases}$$

Briefly, this functional form has been chosen, because it fits the following criteria:

- (1) $\psi^2(0) = 1$
- (2) ψ^2 ought to be a monotonically decreasing function of n
- (3) $\psi^2(0.21) = 0.44$
- (4) $\lim_{\eta \rightarrow -\infty} \psi^2(\eta) = -3.85$

The limiting form of T^{-1} in the presence of a stable stratification as $(\frac{\partial \bar{u}_i}{\partial x_j})^2 \rightarrow 0$ is taken to be 0. However, since the maintenance of turbulence in an unstable stratification is possible in the absence of a mean strain rate, the limiting value is found using the equivalent eddy diffusivity formulations for the turbulent fluxes and is found to be

$$\lim_{T \rightarrow \infty} T^{-2} = + 8.56 (g/\theta_o) \frac{\partial \bar{\theta}}{\partial Z} \text{ for } \eta < 0$$

The time scale has been specified under all conditions and the system is closed.

3. EXPERIMENTAL PROCEDURE

3.1 The Horizontally Homogeneous Model

General testing of the model was done with a horizontally homogeneous subset of the model equations. The large scale horizontal pressure gradient was maintained by incorporating the geostrophic wind as an externally specified input into the integration. Horizontal homogeneity was obtained mathematically by defining $\partial/\partial x_i \equiv 0$ for $i = 1, 2$.

The resulting horizontally homogeneous system is the one that was coded for numerical investigation. This system is as follows:

$$\frac{\partial}{\partial t} (\rho_o \bar{u}) = -f_3 \rho_o \bar{v} g + f_3 \rho_o \bar{v} - \frac{\partial}{\partial z} (\rho_o \overline{u''w''}) \quad (3.1)$$

$$\frac{\partial}{\partial t} (\rho_o \bar{v}) = f_3 \rho_o \bar{u} g - f_3 \rho_o \bar{u} - \frac{\partial}{\partial z} (\rho_o \overline{v''w''}) \quad (3.2)$$

$$\frac{\partial}{\partial t} \bar{r} = - \frac{\partial}{\partial z} (\overline{r''w''}) \quad (3.3)$$

$$\begin{aligned} \frac{\partial}{\partial t} (\rho_o \overline{u''u''}) = & - 2 \overline{u''w''} \frac{\partial \bar{u}}{\partial z} - (b_1/T) (\rho_o \overline{u''u''} - (\rho_o q^2)/3) - \text{Diss} \\ & + \text{Dif} + 2(f_3 \rho_o \overline{u''v''} - \rho_o \overline{u''w''}) \end{aligned} \quad (3.4)$$

$$\begin{aligned} \frac{\partial}{\partial t} (\rho_o \overline{v''v''}) = & - 2 \rho_o \overline{v''w''} \frac{\partial \bar{v}}{\partial z} - (b_1/T) (\rho_o \overline{v''v''} - (\rho_o q^2)/3) \\ & - \text{Diss} + \text{Dif} - 2f_3 \rho_o \overline{u''v''} \end{aligned} \quad (3.5)$$

$$\begin{aligned} \frac{\partial}{\partial t} (\rho_o \overline{w''w''}) = & - (b_1/T) (\rho_o \overline{w''w''} - (\rho_o q^2)/3) - \text{Diss} + \text{Dif} \\ & + 2 g \overline{r''w''} + 2 f_2 \rho_o \overline{u''w''} \end{aligned} \quad (3.6)$$

where

$$\text{Diss} = (a_1/T) (\overline{q^2/3}) ,$$

$$\text{Dif} = C_1 \frac{\partial}{\partial z} [(\overline{q^2 T}) \frac{\partial}{\partial z} (\rho_0 \overline{q^2/3})] ; \quad (3.7a)$$

$$f_2 = 2\Omega \sin\phi$$

$$(3.7b)$$

$$f_3 = 2\Omega \cos\phi$$

$$\frac{\partial}{\partial t} (\rho_0 \overline{u''w''}) = - \rho_0 \overline{w''w''} \frac{\partial \bar{u}}{\partial z} - (b_1/T) \rho_0 \overline{u''w''} + g \overline{r''u''}$$

$$+ f_3 (\rho_0 \overline{v''w''}) + f_2 (\rho_0 \overline{u''u''} - \rho_0 \overline{w''w''}) \quad (3.8)$$

$$\frac{\partial}{\partial t} (\rho_0 \overline{v''w''}) = - \rho_0 \overline{w''w''} \frac{\partial \bar{v}}{\partial z} - (b_1/T) \rho_0 \overline{v''w''} + g \overline{r''v''} - f_3 \rho_0 \overline{u''w''}$$

$$+ f_2 \rho_0 \overline{u''v''} \quad (3.9)$$

$$\frac{\partial}{\partial t} (\rho_0 \overline{u''v''}) = - \rho_0 \overline{v''w''} \frac{\partial \bar{u}}{\partial z} - \rho_0 \overline{u''w''} \frac{\partial \bar{v}}{\partial z} - (b_1/T) \rho_0 \overline{u''v''}$$

$$+ f_3 (\rho_0 \overline{v''v''} - \rho_0 \overline{u''u''}) - f_2 \rho_0 \overline{v''w''} \quad (3.10)$$

$$\frac{\partial}{\partial t} (\overline{r''u''}) = - \overline{r''w''} \frac{\partial \bar{u}}{\partial z} - \overline{u''w''} \left(\frac{\partial \bar{r}}{\partial z} + \rho_0 \frac{\partial}{\partial z} \ln\theta_0 \right)$$

$$- (b_2/T) \overline{r''u''} + f_3 \overline{r''v''} - f_2 \overline{r''w''} \quad (3.11)$$

$$\begin{aligned} \frac{\partial}{\partial t} \overline{r''v''} &= - \overline{r''w''} \frac{\partial \bar{r}}{\partial z} - \overline{v''w''} \left(\frac{\partial \bar{r}}{\partial z} + \rho_o \frac{\partial}{\partial z} \ln \theta_o \right) \\ &\quad - (b_2/T) \overline{r''v''} - f_3 \overline{r''u''} \end{aligned} \quad (3.12)$$

$$\begin{aligned} \frac{\partial}{\partial t} \overline{r''w''} &= - \overline{w''w''} \left(\frac{\partial \bar{r}}{\partial z} + \rho_o \frac{\partial}{\partial z} \ln \theta_o \right) - (b_2/T) \overline{r''w''} + (g/\rho_o) \overline{r''r''} \\ &\quad + f_2 \overline{r''u''} \end{aligned} \quad (3.13)$$

$$\begin{aligned} \frac{\partial}{\partial t} \overline{r''r''} &= - 2 \overline{r''w''} \left(\frac{\partial \bar{r}}{\partial z} + \rho_o \frac{\partial}{\partial z} \ln \theta_o \right) - (a_2/T) \overline{r''r''} \\ &\quad + c_2 \frac{\partial}{\partial z} \left[\overline{q^2 T} \frac{\partial}{\partial z} (\overline{r''r''}) \right] ; \end{aligned} \quad (3.14)$$

where the constants $a_1, b_1, c_1, a_2, b_2, c_2$ are as given in Manton and Cotton (1975a). These values are:

$$a_1 = 2b_1 / (2 + 3b_1^2) = 0.32 \quad (3.15a)$$

$$b_1 = 1.69 \quad (3.15b)$$

$$c_1 = 0.48 \quad (3.15c)$$

$$a_2 = 0.78 \quad (3.15d)$$

$$b_2 = 1.25 \quad (3.15e)$$

$$c_2 = 3.37 \quad (3.15f)$$

Implicit in the assumption of horizontal homogeneity is that $\bar{w} \equiv 0$. This can be seen by integrating the equation for mass conservation vertically to get: $\rho_o \bar{w}]_{z_{TOP}} - \rho_o \bar{w}]_{z_{BOT}} = 0$, since the net mass flux through the top boundary must be zero in the absence of horizontal convergence. And since $\rho_o(z_{TOP}) \neq \rho_o(z_{BOT})$, then the implication is that $\bar{w}(z) \equiv 0$. Then all vertical transports of heat and momentum which occur must be accounted for in the w'' field, that is all vertical transport is turbulent. Profiles of the base state thermodynamic variables are specified as an initial condition and remain constant throughout the time integration.

3.2 General Numerical Procedure

3.2.1. Time Differencing

Since the type of time operator and spatial differencing chosen in a numerical simulation can strongly bias the results, some care must be taken both in choosing a particular operator and in analyzing the results. Any numerical operator is in itself an averaging operator, and energy can be gained and/or lost in frequencies or wavelength which we are trying to model strictly through numerical error. Therefore, some knowledge of the characteristics of the particular operators used is necessary, when attempting to apply some interpretation to the results of a time integration. For these experiments, the Matsuno (Matsuno, 1966) or Euler backward time differencing scheme was chosen. The Matsuno is an inherently damping operator, with stronger damping at the higher frequencies and tending to less damping at longer time periods. This type of

operator enhances numerically the natural energy cascade into higher and higher frequencies by extracting it from the smallest scales. Conversely, if one is trying to model physical systems whereby there is also an up scale transport of kinetic energy, the operator can work against you.

3.2.2 Spatial Differencing

Spatial differences are centered in space on a staggered grid. Centered differences are neutral in their damping characteristics. Staggering the grid provides better control of nonlinear computational instability and at the same time yields an operator which is flux-conservative. As shown in Fig. 3-1, first order moments or mean fields were defined at ZM(1) . . . , ZM(KMAX), and second order moments or turbulence fields were defined at ZT(1) . . . , ZT(KMAX). In this manner, the spatial derivatives of the fluxes are defined at the mean grid points.

In this particular coding of the model, the capability for a nonconstant grid interval was maintained. This was done by specifying a particular height or vertical coordinate for each individual point on the ZT grid. Then the ZM grid points with the same index were defined at a point equidistant between the corresponding ZT grid point and the next higher one. This formulation also allowed variation of the specified height for the lower boundary--a constant flux surface layer model.

A few experiments were run with a non-constant grid interval for sensitivity testing, however, most were run with a constant grid interval of 50 or 100 meters. The constant flux surface layer then

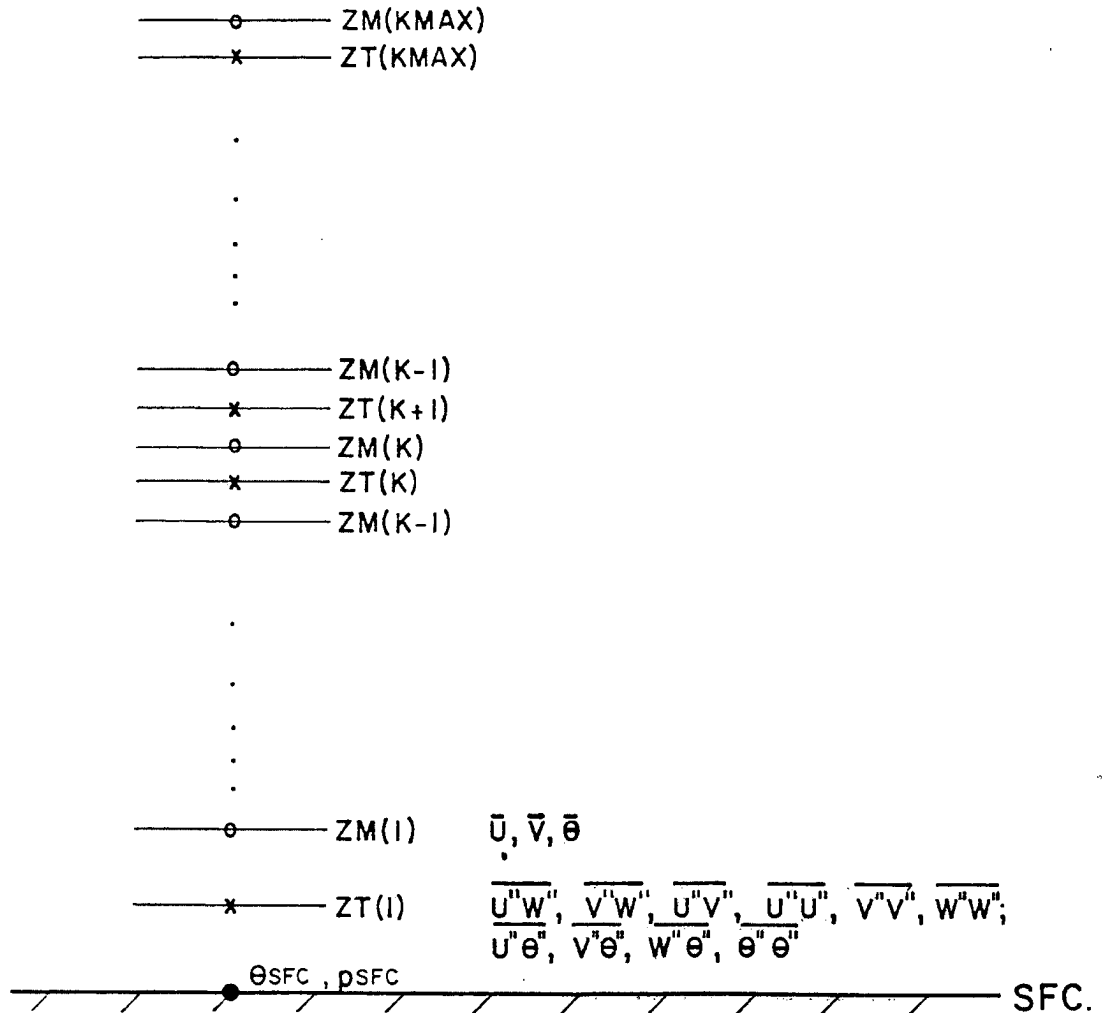


Figure 3-1. Schematic depiction of the staggered grid. Mean variables are defined at the open circles; turbulent quantities are defined at the x's.

represents approximately the lowest 50 or 100 meters, respectively. The second order spatial differences which occur in the diffusion terms are formed as given in the following examples:

$$\frac{\partial^2 Q(z)}{\partial z^2} \approx \left(\frac{Q(ZT(K+1)) - Q(ZT(K))}{ZT(K+1) - ZT(K)} - \frac{Q(ZT(K)) - Q(ZT(K-1))}{(ZT(K) - ZT(K-1))} \right) / (ZM(K) - ZM(K-1)) \quad (3.16)$$

Where values defined on one grid are needed to be defined on the other grid, (e.g., diffusion coefficients), a simple average was used:

$$Q(ZT(K)) = \frac{Q(ZM(K-1)) + Q(ZM(K))}{2} \quad (3.17)$$

3.2.3 Criteria for Numerical Stability

The numerical stability of the time integration was maintained by two methods:

- (1) integrating the diffusion terms in a strictly forward manner; and
- (2) insuring that K , the diffusion coefficient is maintained within the linear stability criteria (see Haltiner, 1971) for transport terms ($K \leq 2\Delta z^2/\Delta t$).

The uses of second order spatial differences in the calculation of the time derivative places certain restrictions on the time operator used, namely a strictly forward operator is the only stable operator. Hence, in the second Matsuno pass, corrected second order differences were not calculated but values obtained on the first pass were saved and used in the second pass to insure a strictly forward time step on

these terms. The following criterion was applied to the turbulent time-scale, T . Since $K_i = \overline{q^2} T c_i$, the following check was made:

$$T^{-2} \geq C_{i_{\max}} \left(\frac{2 * \overline{q^2} [ZT(K)] * \Delta t}{[ZM(K) - ZM(K-1)]^2} \right) ; \quad (3.18)$$

if yes, then T^{-2} was left unchanged; if not, then T^{-2} was adjusted accordingly. Fortunately this adjustment was rarely needed, since T was seen to vary inversely with $\overline{q^2}$. The reasons for applying the stability criteria in this manner were twofold: (1) the theoretical formulation of T does contain some uncertainty (see Manton and Cotton, 1977b), and (2) in order to make valid comparisons among different model runs it was much more important to work with reproducible grid elements and time steps in order to systematize the truncation error.

3.3 Boundary Conditions

3.3.1 Upper Boundary Conditions

Values defined at $ZM(KMAX)$, the upper boundary of the model, on the mean grid were assumed to represent the free atmosphere above the planetary boundary layer. Accordingly, they were left alone and remained constant throughout the integration at their specified values. In particular $\overline{\theta'}$ was defined to be zero and remained zero. Top values of the fluxes, defined at $ZT(KMAX)$, were not specified, and were allowed to vary with time. The contention here was to not force an arbitrary anchor point for the turbulent profiles, but to let them find their own natural zero. If the model is deep enough, these quantities should find it naturally. No flux or transport of momentum

or temperature variance was allowed through the top. This was accomplished by calculating the diffusion for the variances defined at ZT(KMAX) in the following manner:

$$\text{DIFF(VAR)} = \frac{0 - K(Z\text{MAX}) [\rho_0 \overline{Q^2} (K\text{MAX}) - \rho_0 Q^2 (K\text{MAX} - 1)]}{(\Delta z)^2} \quad (3.19)$$

3.3.2 Lower Boundary Conditions

Since the existence of the turbulence in the planetary boundary layer is due to the presence of the earth at the bottom of the atmosphere, proper specification of the lower boundary is critical to the overall success of a model of this sort. In this model surface values (i.e. those defined at $z = z_0$, where z_0 is the roughness length) for the mean variables are specified. At the lowest grid point for the mean fields, ZM(1), values are predicted by the model and no specification is necessary. The second order moments however need to be specified at the lowest grid point for the turbulence variables, ZT(1). This was done by assuming that the level defined by ZT(1) is within a constant flux surface layer. Then, the turbulent fluxes and variances can be specified by some convenient scheme.

Several diagnostic schemes for defining fluxes in the constant flux surface layer have been published in recent years, for example see Mellor (1973), Lewellen and Teske (1973). However, because of its obvious compatibility with this model, the one chosen is given in Manton and Cotton (1977a). This constant flux surface layer model assumes an equilibrium surface layer (i.e. the local rate of production of T.K.E. is exactly balanced by the local rate of dissipation of T.K.E.). Turbulent transport of the variances and co-variances has

been neglected. It provides explicit algebraic equations for the variances and co-variances of momentum and temperature which the authors claim provide realistic values of these variances and co-variances. These values are then used to specify the lower values for the turbulence variables at ZT(1) at each time step.

The lower boundary values as given by this surface layer parameterization scheme are updated each time step in the following manner. Appendix A shows the total scheme. Since in the surface layer the velocity is assumed to act in the X_1 direction, the mean wind at ZM(1) is reformulated into polar coordinates. This is done in order to define the X_1 direction and the angle δ , of rotation of the surface layer coordinate system with respect to the model coordinate system (which is defined in the usual meteorological sense). Implicit in this assumption is that there is no frictional turning of the mean wind in the surface layer. The mean variables are assumed to vary according to the well-known profiles of Monin and Yaglom (1971):

$$\frac{\partial \bar{u}_m}{\partial z} = \frac{u_*^*}{kz} \phi_m \left(\frac{z}{L} \right) = \frac{u_*^*}{kz} \phi_m (\xi) \quad (3.20)$$

$$\frac{\partial \theta}{\partial z} = \frac{\theta_*^*}{kz} \phi_h \left(\frac{z}{L} \right) = \frac{+H}{ku_*^*z} \phi_h (\xi) \quad (3.21)$$

where u_*^* is the friction velocity, $H = \theta_*^* u_*^*$, k is von Karman's constant, and ϕ_m and ϕ_h are universal functions of $\xi = z/L$, where L is the Obukhov length. The heat flux, $\overline{\theta''w''}$ and the momentum flux $\overline{v_h''w''}$ are defined in terms of u_*^* and H by

$$\overline{v_h''w''} = - u_*^{*2} \quad (3.22)$$

$$\overline{\theta''w''} = - H \quad (3.23)$$

Equations (3.20) and (3.21) have been integrated (Paulson, 1970) to give:

$$\overline{u}_m(z) = \frac{u_*^*}{k} \left[\ln\left(\frac{z}{z_0}\right) - \psi_m(\xi) \right] \quad (3.24)$$

$$\overline{\theta}(z) - \overline{\theta}(z_0) = \frac{.74H}{u_*^*k} \left(\ln\left(\frac{z}{z_0}\right) - \psi_H(\xi) \right) \quad (3.25)$$

where the exact functional forms of ψ_m and ψ_h are determined from the functional form used for ϕ_m and ϕ_h . Appendix B gives the exact functional form for ϕ_m , ϕ_h , ψ_m , and ψ_h used for these equations. Those for ϕ_m and ϕ_h , from which ψ_m and ψ_h are derived are essentially that given by Businger, et al. (1971), but were revised slightly by Manton and Cotton (1977a) to fit data presented by Carl, et al. (1973) for values of $\xi \leq -0.5$. Equations (3.24) and (3.25) are then inverted to obtain values of u_* and H in the surface layer, in terms of \overline{u} , and $\overline{\theta}$ defined at ZM(1) and the externally specified surface temperature at z_0 . Since ψ_H and ψ_m are functions of z/L and L is a function of u_* and H, the inversion is accomplished numerically by an iterative process. An initial estimate is made of u_* and H which is used to calculate ξ . This value of ξ is used in equations (3.24) and (3.25) to give new estimates of u_* and H. This procedure was then repeated until the new estimate of u_* did not differ from the previous one by more than 1%. Experiments with the model show that convergence for this iterative calculation is fairly rapid, but that there do exist regions of the $(\overline{u}, \Delta\theta)$ plane where convergence does not occur. Surface temperature was specified in a tabular form of time and temperature and a simple linear interpolation was performed by the model to obtain a specific surface temperature between 2 points at

each time step of model integration. Surface temperatures were tabulated at frequent enough intervals (usually one hour) in order to achieve a good reproduction of an observed profile in time. Once updated values of u_* and H were obtained, they were used to evaluate $\phi_m(\xi)$ and $\phi_h(\xi)$ at $ZT(1)$ (though u_* and H are considered constant in the constant flux layer-- ξ is not). The Manton-Cotton surface layer parameterization was then used to predict the variances and co-variances at $ZT(1)$ in the rotated coordinate system. Finally the coordinate system is rotated back to the standard meteorological system. Let subscript R denote the values obtained from the surface layer model; and let the derived values in the model coordinate system be unsubscripted. Then we have:

$$\overline{u''w''} = (\overline{u''w''})_R \cos(\delta) = -u_*^2 \cos(\delta) \quad (3.26)$$

$$\overline{v''w''} = (\overline{u''w''})_R \sin(\delta) = -u_*^2 \sin(\delta) \quad (3.27)$$

$$\overline{u''\theta''} = (\overline{u''\theta''})_R \cos(\delta) \quad (3.28)$$

$$\overline{v''\theta''} = (\overline{u''\theta''})_R \sin(\delta) \quad (3.29)$$

$$\overline{w''\theta''} = (\overline{w''\theta''})_R = -H \quad (3.30)$$

$$\overline{u''v''} = [(\overline{u''u''})_R - (\overline{v''v''})_R] * \sin(\delta) * \cos(\delta) \quad (3.31)$$

$$\overline{u''u''} = (\overline{u''u''})_R * \cos^2(\delta) + (\overline{v''v''})_R \sin^2(\delta) \quad (3.32)$$

$$\overline{v''v''} = (\overline{v''v''})_R * \cos^2(\delta) + (\overline{u''u''})_R \sin^2(\delta) \quad (3.33)$$

$$\overline{w''w''} = (\overline{w''w''})_R \quad (3.34)$$

$$\overline{\theta''\theta''} = (\overline{\theta''\theta''})_R \quad (3.35)$$

Thus all flow variables are specified at the lower boundary.

3.4 Calculation of the Turbulent Time Scale

In keeping with the stability criteria outlined in section 3.3.1 above, the turbulent time scale was calculated only once each time step because of its use in calculation of the diffusion coefficient K . In the absence of any mean stress, numerical considerations dictate that T^{-2} cannot become zero, therefore a lower bound of 10^{-8} was used, limiting T and keeping the magnitude of K below the maximum value permissible in order to maintain computational stability for a specified Δt and Δz .

4. RESULTS

The Manton-Cotton model, as described in Chapters 2 and 3 of this paper, was integrated numerically on a vertical finite difference grid on the NCAR 7600 computer. An attempt was made to run the model under various conditions in order to determine if the model was: (1) stable and well behaved, (2) well coupled with the surface layer scheme used as a lower boundary condition, and (3) able to couple the fields of thermal and momentum flux in a physically realistic manner. To this end, the model was run under a neutral stratification with moderate and high wind fields, under a stable stratification with a moderate wind field, a stable stratification and a low wind field with surface heating, and finally in order to test the overall predictability of the model, runs were made using data from the Wangara Experiment (Clark, et al., 1971).

4.1 Sensitivity Tests and Internal Consistency Checks

Preliminary simulation attempts were made under various initial conditions, the results of which, though not conclusive, lend direction to further research effort and point out deficiencies in the mathematical and/or computational structure of the model.

4.1.1 Model Initialization

In the integrations to be described in this paper, model initialization was intentionally unspecified for the flux profiles of momentum and heat. Attempts made to initialize the profiles of variance and covariance in the presence of a stable atmosphere led to strong oscillations in the variance of vertical velocity. The oscillation proceeded as a damped sine wave, as the suppression of the turbulence

by the stable stratification overcame the other balancing terms in the time dependent equation for vertical velocity variance. It is this author's opinion that this result is indicative of a limitation of the pressure-velocity covariance parameterization. In a stably stratified atmosphere, the occurrence of turbulence would be strongly suppressed; but the turning of the turbulence into the horizontal plane of motion would occur on the same effective characteristic time scale. Since the model did not react in this manner, this is suggestive of the need for a buoyancy related term in the pressure-velocity correlation parameterization. This has been previously hinted at in the work of Wyngaard and Cote (1974) and Lumley and Khajeh-Nouri (1974).

4.1.2 Calibration of Coefficients

The constants, as given in section 3.1, equation 3.15 are found by calibrating the model with the surface layer observations of So and Mellor (1972), Businger et al (1971) and Wyngaard et al. (1971). The extension of these coefficients into the planetary boundary layer above the surface is assumed to be the function of the generalized turbulent time scale, T .

Preliminary testing with the model showed that in general this was an invalid assumption. The model would not run with dissipation calibrated in the surface layer. Nothing could get started above the surface layer, and all heating was confined to the lowest 3 grid points. All later model runs were run with dissipation at 1/10 its calculated value. Variation of the dissipation about this value would alter the maximum of the turbulent kinetic energy profile but not its shape or the height of the maximum above the surface.

The coefficients of diffusion, $C_i q^2 T$, were also too large. The effect of using values calibrated from the surface layer observations of Wyngaard et. al. (1971) under steady unstable conditions was to completely wash out the inversion causing it to completely lose its definition. The resulting profiles were seen to vary smoothly and continuously from the surface to the top boundary of the model. Reducing the diffusion coefficient to 1/10 its original value maintained the sharpness of the inversion, but the resulting entrainment across the inversion of the potentially warmer dryer air above into the well mixed layer below and the subsequent negative heat flux was almost negligible. In an attempt to maximize the negative heat flux at the inversion, yet maintain the sharpness of the inversion, a final value of approximately 1/5 the calibrated value was chosen. This result leads to the conclusion that when all vertical transports are turbulent, the simple gradient diffusion closure model for the triple correlation products is insufficient to properly model the dynamics of entrainment across the inversion.

In an effort to maintain a higher percentage of the convectively generated turbulent kinetic energy in the vertical component, the coefficient of isotropization in the pressure-velocity parameterization was reduced. An order of magnitude reduction in this co-efficient led to only slightly more energy in the vertical component, and negligible increase in the magnitude of the negative heat flux above the inversion. In the neutrally stable case, however, any reduction greater than a factor of 2 led to highly unrealistic profiles of momentum variances and covariances. Since the original coefficients were of order unity,

the final choice was to leave the values unchanged because there appeared to be no valid reason for altering the values.

4.2 Neutral Case Study

In this, the simplest case considered, the model was integrated with an eye toward considering only the momentum terms of the system. Therefore a neutrally stratified atmosphere was used in order to decouple the buoyant generation and suppression of turbulence from the strictly mechanical generation terms. A moderate strength geostrophic wind of 10 msec^{-1} was used with no thermal wind. The magnitude of the Coriolis frequency, f , was defined at 45° north latitude. Surface heating was specified as identically zero and the model integrated toward mechanical equilibrium.

4.2.1 Model Initialization

No profiles for the turbulent quantities were specified, hence they were assumed identically zero. The mean \bar{u} and \bar{v} profiles were initialized at the geostrophic values. Lower boundary conditions for the turbulence fields were as predicted from the surface layer parameterization with the selected $\bar{u}_m[ZM(1)] = 10 \text{ msec}^{-1}$, the geostrophic wind speed. The selected grid interval was a constant 100 m with $ZT(1)$ defined at a height of 50 m. Therefore $ZM(1)$ was at a height of 100 m. The time step was set a constant value of 2 seconds.

4.2.2 Results of Integration

A time plot for the vertically averaged turbulent kinetic energy intensity is shown in Figure 4-1. As is shown, a maximum in the turbulent kinetic energy intensity is achieved only after 12 hours of integration, and then the intensity is seen to decay slightly. The

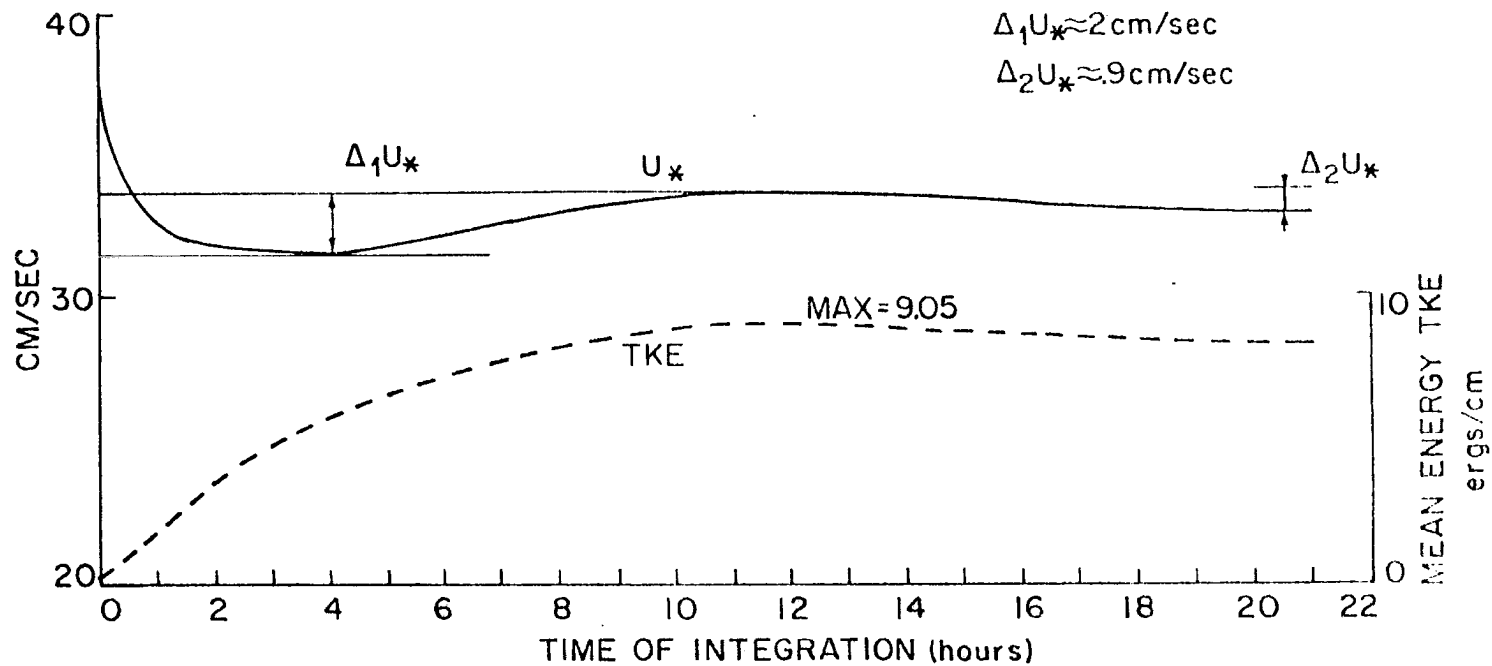


Figure 4-1. The vertically averaged Turbulent Kinetic Energy (T.K.E.) and friction velocity, u_* as a function of time of integration. $\Delta_1 u_*$ and $\Delta_2 u_*$ estimate the amplitude of the damped oscillation.

slow decay is a result of sustained dissipation. Figure 4-2, compares profiles of turbulent kinetic energy at 12 hours and 18 hours. The decay in the turbulent intensity is relatively uniform through the vertical profile with slightly more decay toward the top. Dissipation in the model was modelled proportional $\overline{q^2}/T$. A 500% change in the profile of the time scale is seen between the surface layer and the free atmosphere value with approximately half of the change occurring at the level where the frictional turning of the mean wind begins at approximately 300 meters in height (Fig. 4-3). The important thing to note is that dissipation acts in such a way that the general shape of the profile does not change but only the magnitude. The smoothness of the predicted profiles above the surface layer is very encouraging.

In Figure 4-4, profiles of the individual components of the T.K.E. are shown at Time $T = 12$ hours. The maximum in the profile of $\overline{u''u''}$ is shown to be slightly lower in height and about 15% greater in magnitude than the maximum in the other 2 components. This presumably is because the dominant generation term is the shear of the u component of the mean wind. The north-south variance $\overline{v''v''}$ is slightly larger than the vertical component because there is some slight shear in the northerly component of the mean wind (Figure 4-5). Also note that the surface layer values are substantially smaller than the model predicted values. The predicted profiles of the mean wind are shown in Figure 4-5 at $T = 12$ hours. The predicted \bar{u} component exhibits strong shear in the lowest few hundred meters and is then essentially constant and supergeostrophic above that for about 500 meters. The \bar{u} component then slowly converges to the geostrophic value to the top. The momentum flux profiles are shown in Figure 4-6. In contrast to the

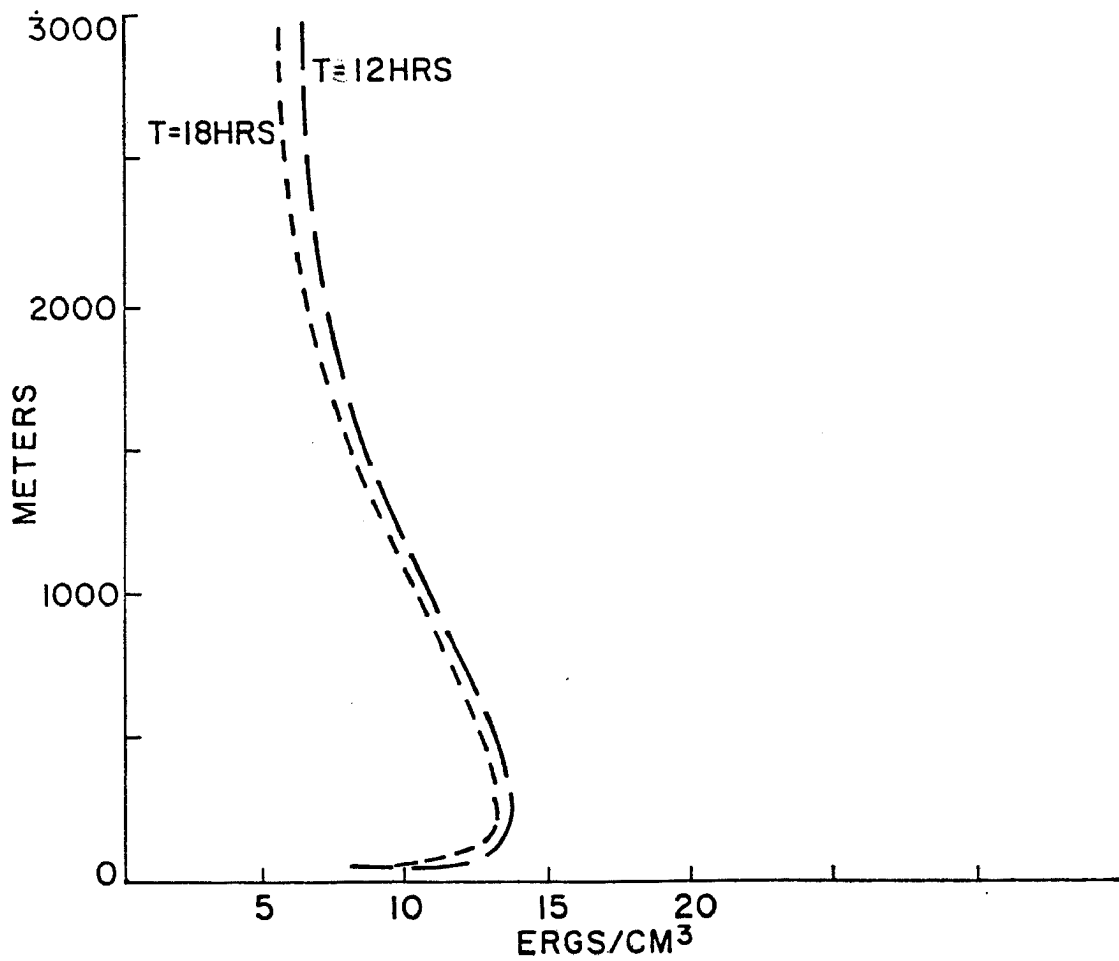


Figure 4-2. Vertical profiles of the turbulent kinetic energy intensity (ergs·cm³) at T=12 hours and at T=18 hours for neutrally stratified case study.

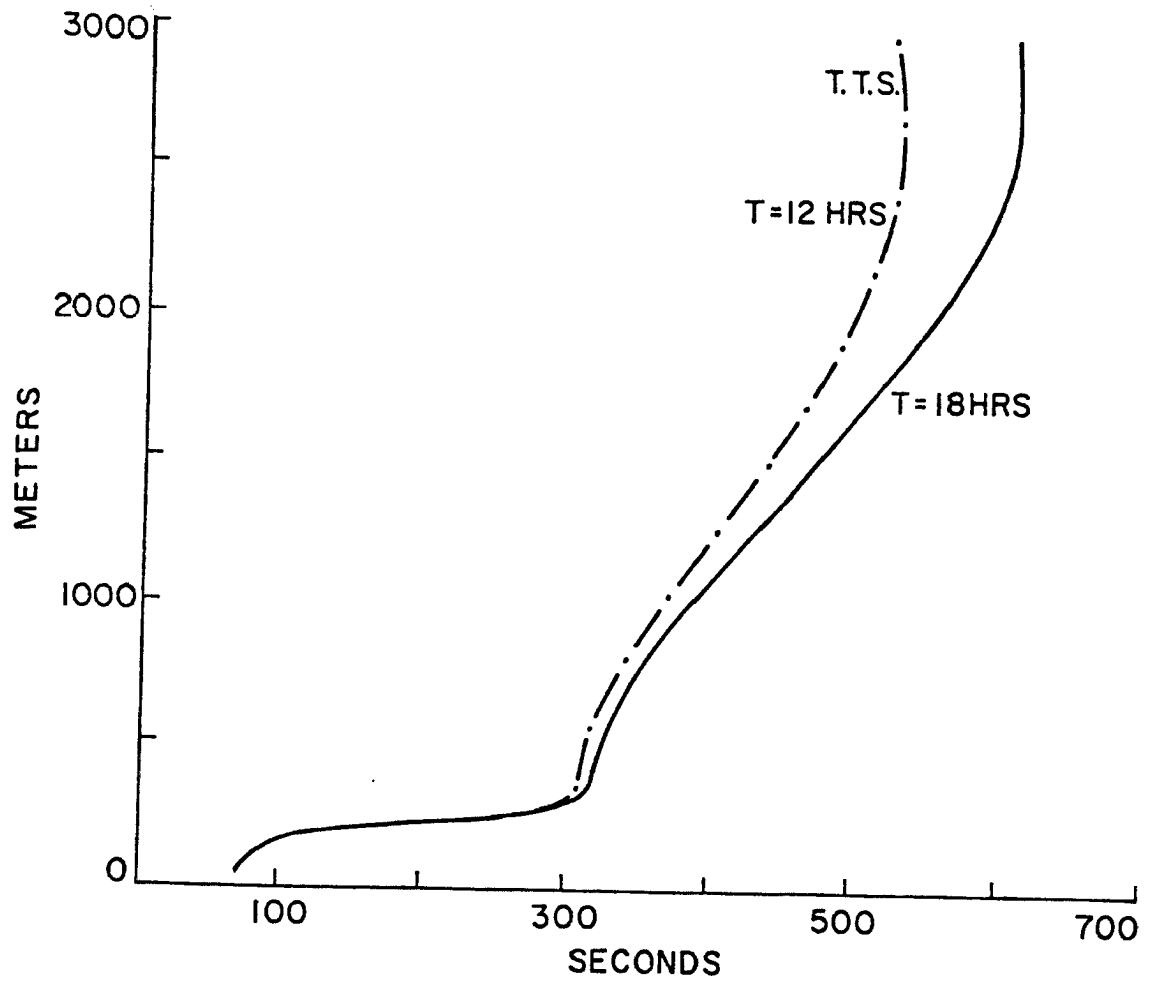


Figure 4-3a. Vertical profiles of the Turbulent Time Scale (T.T.S) at T=12 hours and T=18 hours.

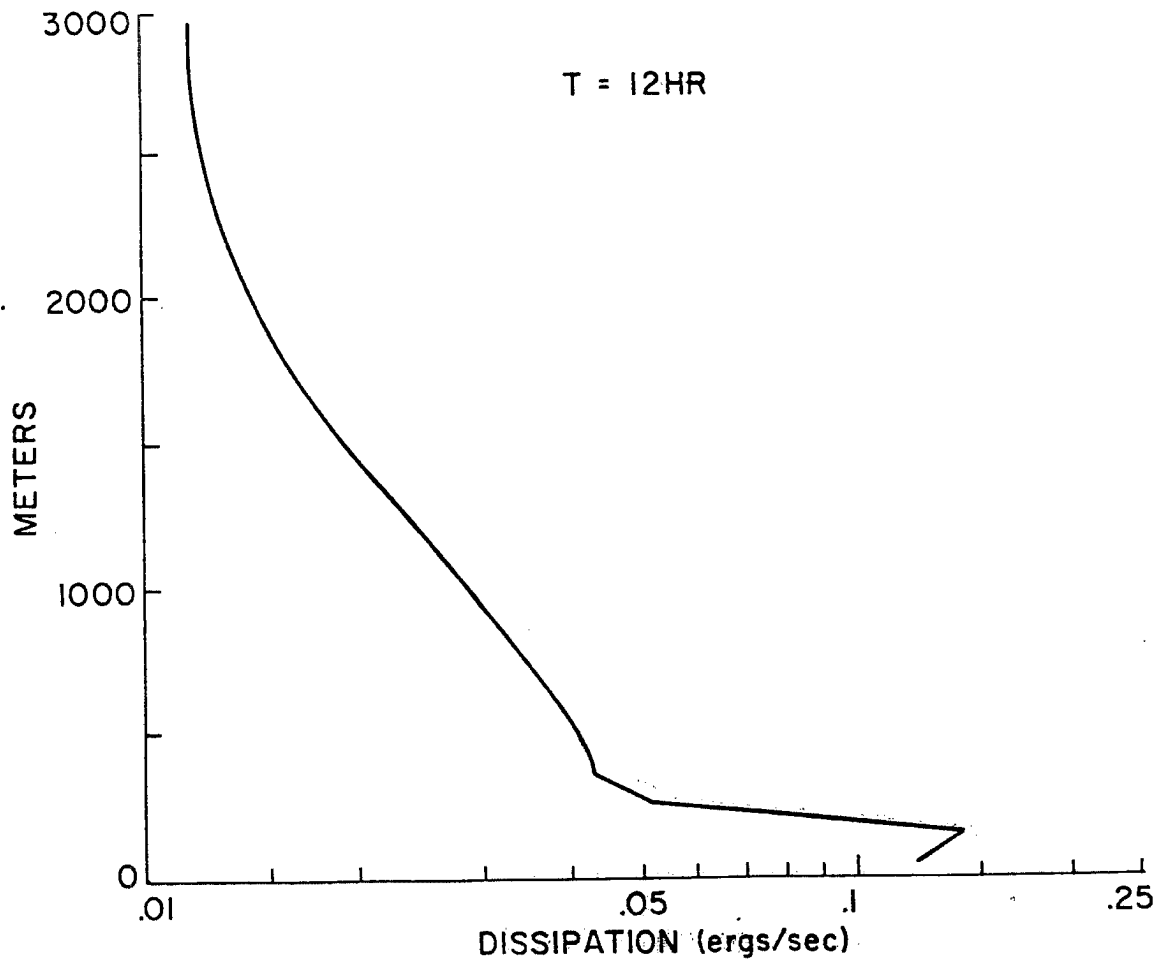


Figure 4-3b. Vertical profiles of the associated dissipation at T=12 hours for the neutrally stratified case study.

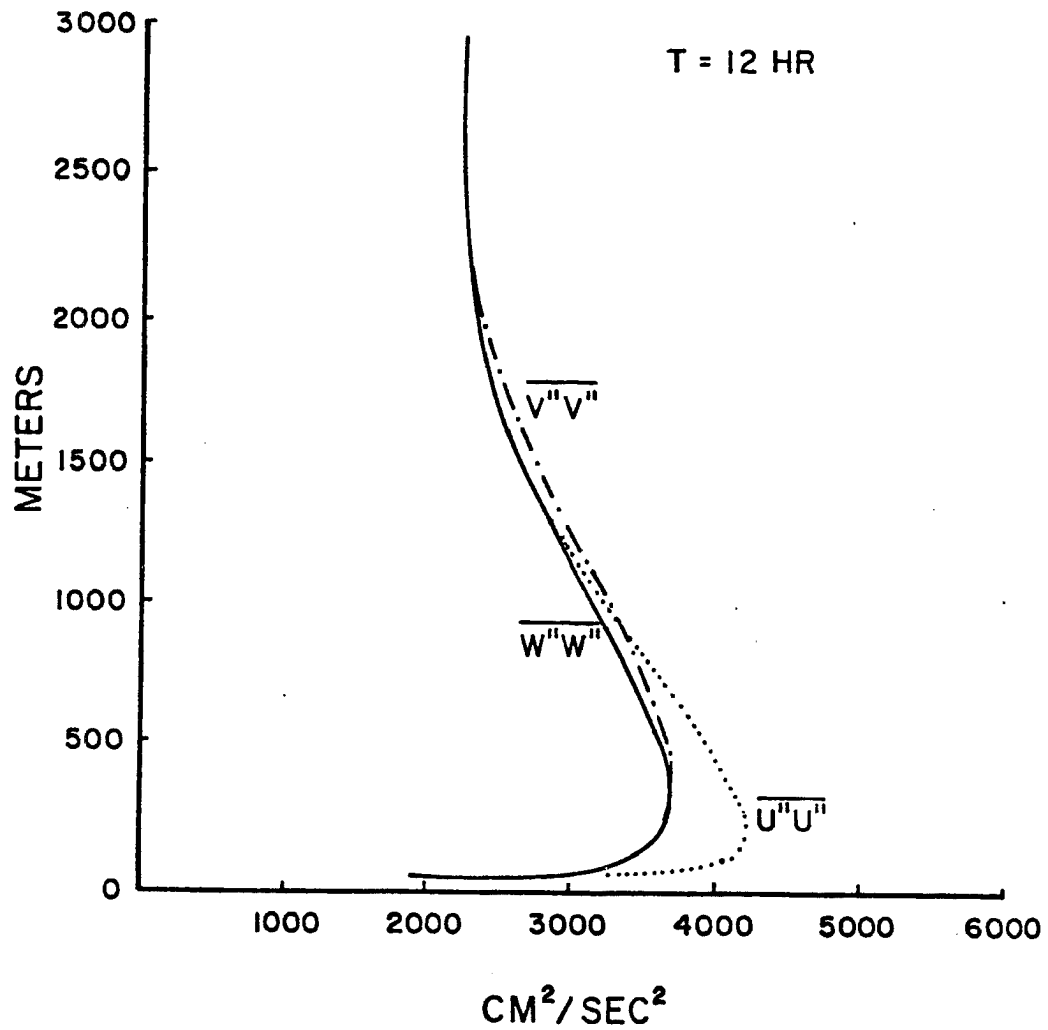


Figure 4-4. Vertical profiles of the individual components of the Turbulent Kinetic Energy; $\overline{u''u''}$ (dotted), $\overline{v''v''}$ (dash-dot), and $\overline{w''w''}$ (solid), at T=12 hours for the neutrally stratified case study.

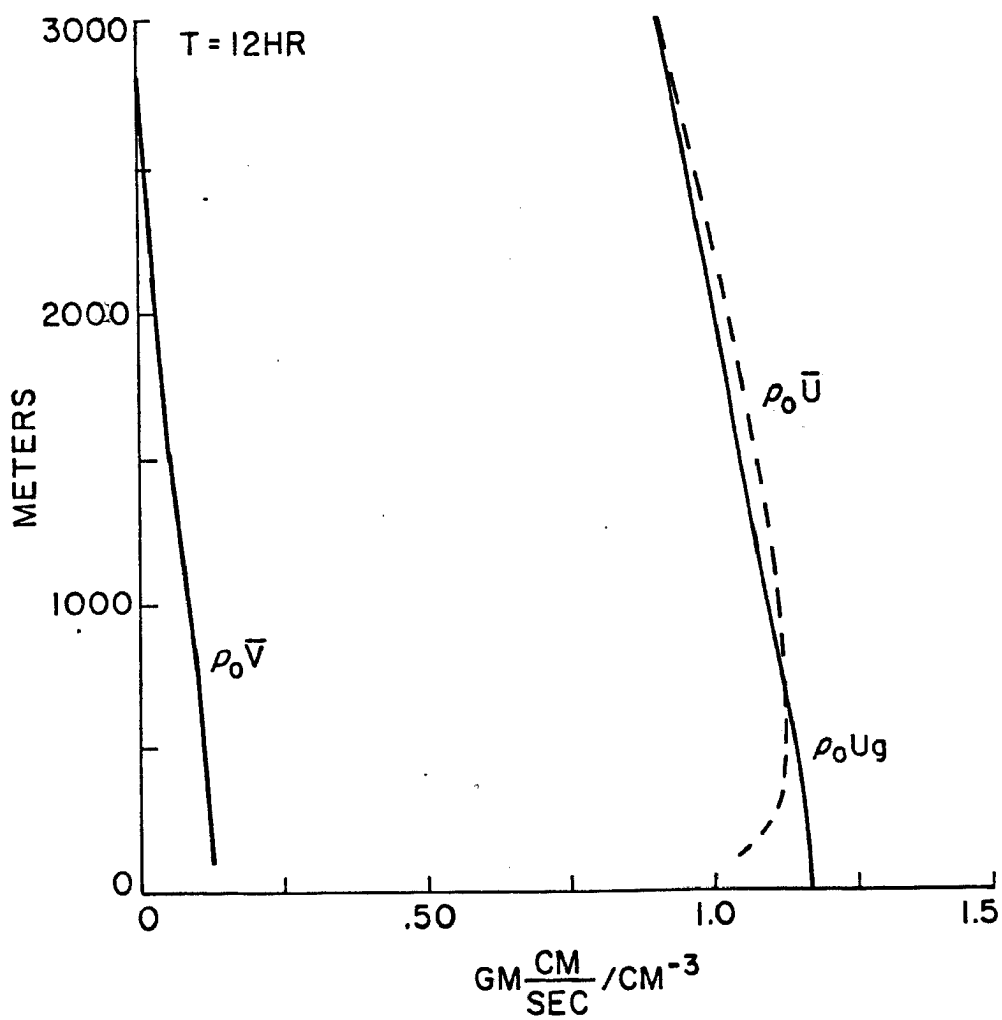


Figure 4-5. Vertical profiles of model predicted east-west, $\rho_0 \bar{u}$, and north-south, $\rho_0 \bar{v}$, mean momentum per unit volume. The constant $\rho_0 \bar{u}_g$ (solid line) is also shown. $\rho_0 \bar{v}_g$ is identically zero.

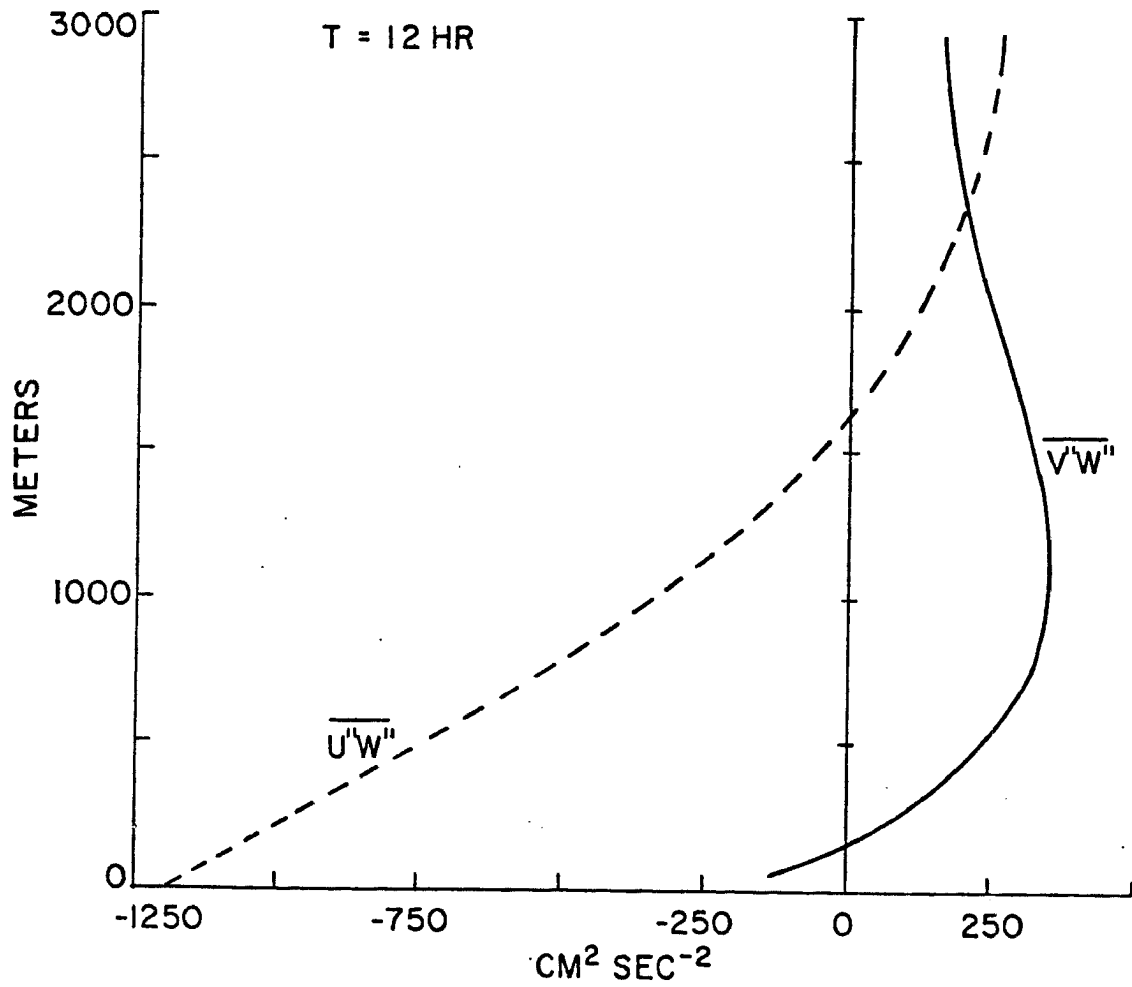


Figure 4-6. Vertical profiles of the vertical turbulent momentum flux at T=12 hours in the neutrally stratified case study.

profiles of T.K.E., these profiles are seen to merge very smoothly with surface layer values. Of particular interest is the fact that the vertical derivative of the $\overline{u''w''}$ profile does not change sign but goes smoothly to zero. The derivative of the $\overline{v''w''}$, on the other hand, has two zero values; one at the top as expected and one in the PBL layer. This is indicative of a net convergence of v momentum in the lower part of the layer, and a net divergence in the upper part of the layer. This occurs even though the flux is seen to be always down-gradient and must be the factor maintaining the linear profile of \bar{v} in the layer.

Figure 4-7 shows a time plot for the frictional turning of the wind at 100 m, for values of z_0 , = 1.0, 2.0, and 5.0 centimeters respectively. The predicted damped inertial oscillation has a period of approximately $2\pi/f$ or approximately 18 hours. The amplitude of the oscillation appears not to vary with z_0 , though it is seen that the degree of frictional turning is functionally dependent on z_0 . Figure 4-8 and Figure 4-9 show a time series of u_* , the frictional velocity and the layer-averaged turbulent kinetic energy respectively. In both cases, the magnitude of the surface stress and column average turbulent energy is seen to increase with z_0 . There is also evidence of an inertial oscillation in the surface stress, and it appears to be exactly 90° out of phase with the inertial oscillation of the mean wind.

4.2.3 Discussion

A boundary layer wind spiral (from unpublished work by Reid and Cotton), obtained using the traditional eddy viscosity closure for the momentum flux terms in the equation for mean momentum is shown in Figure 4-10a. A description of the model is given in Pielke and Mahrer (1975). It exhibits the typical Ekman Spiral with the greatest

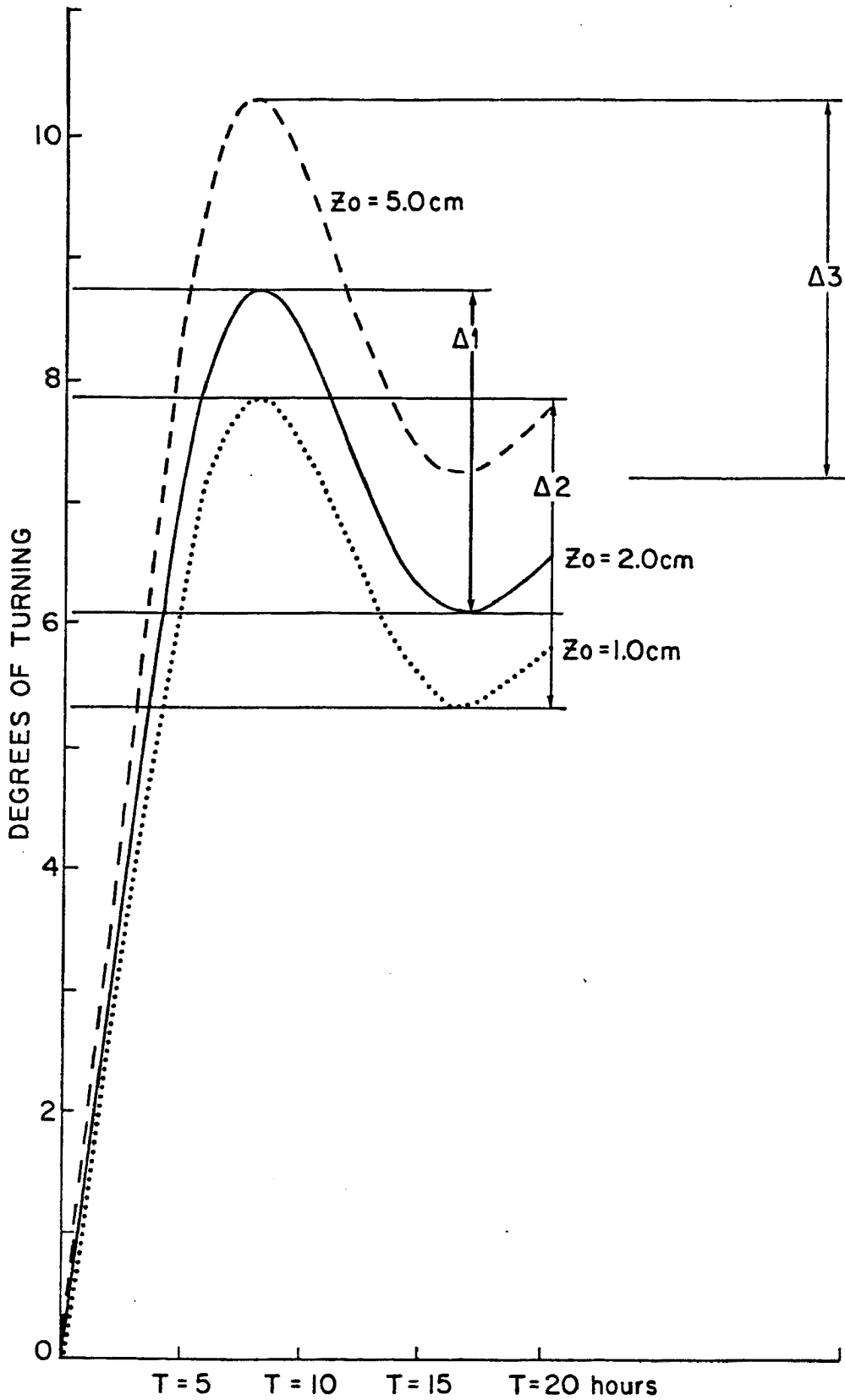


Figure 4-7. Degree of frictional turning of 100m wind as a function of time of integration for values of $z = 1.0\text{cm}$ (dotted) $z = 2.0\text{cm}$ (solid) and $z = 5.0\text{cm}$ (dashed) for the neutrally stratified case study.

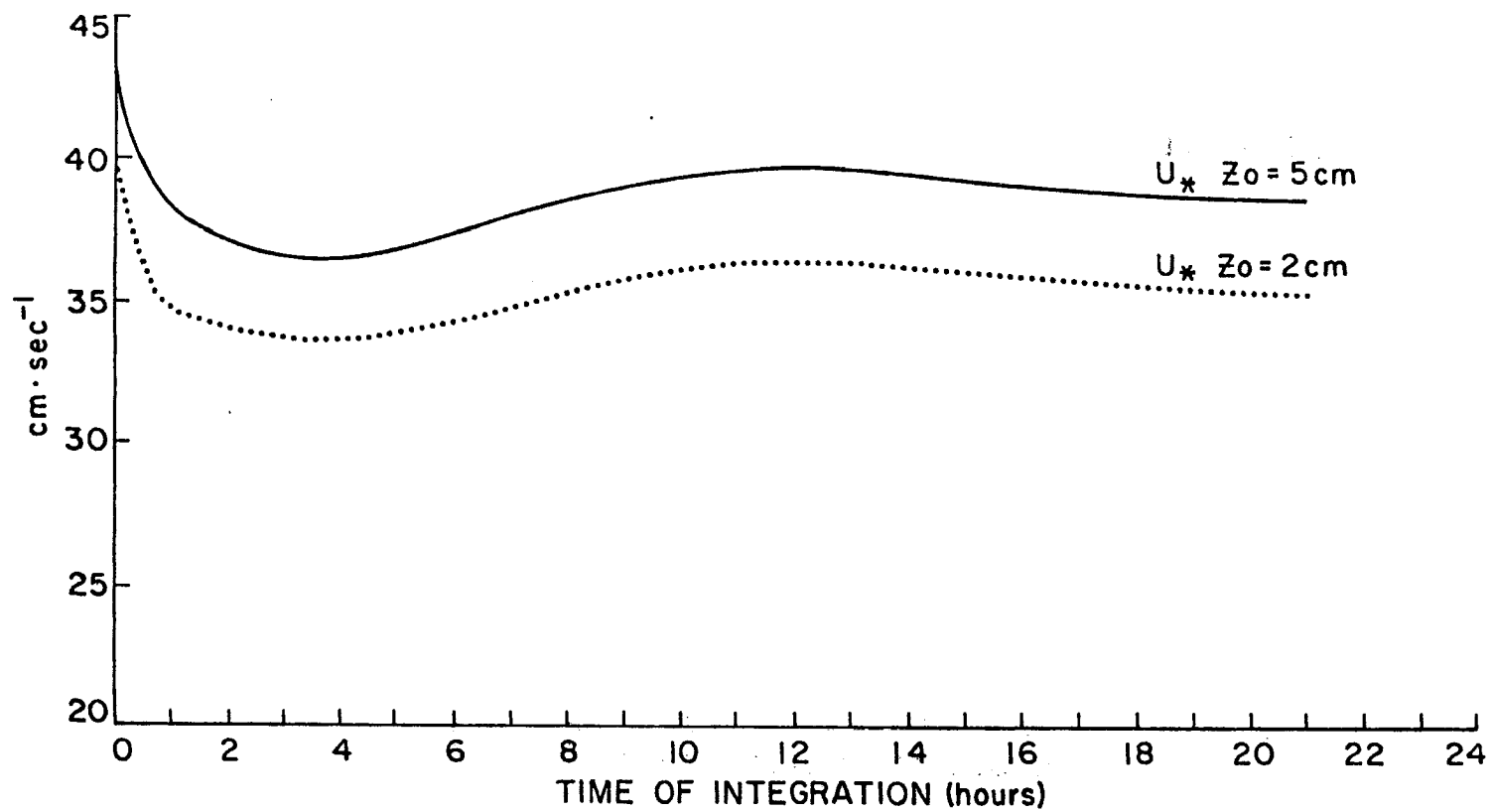


Figure 4-8. Friction velocity, u_* , as a function of time of integration for $z_0 = 2.0 \text{ cm}$ (dotted) and $z_0 = 5.0 \text{ cm}$ (solid) for the neutrally stratified case study.

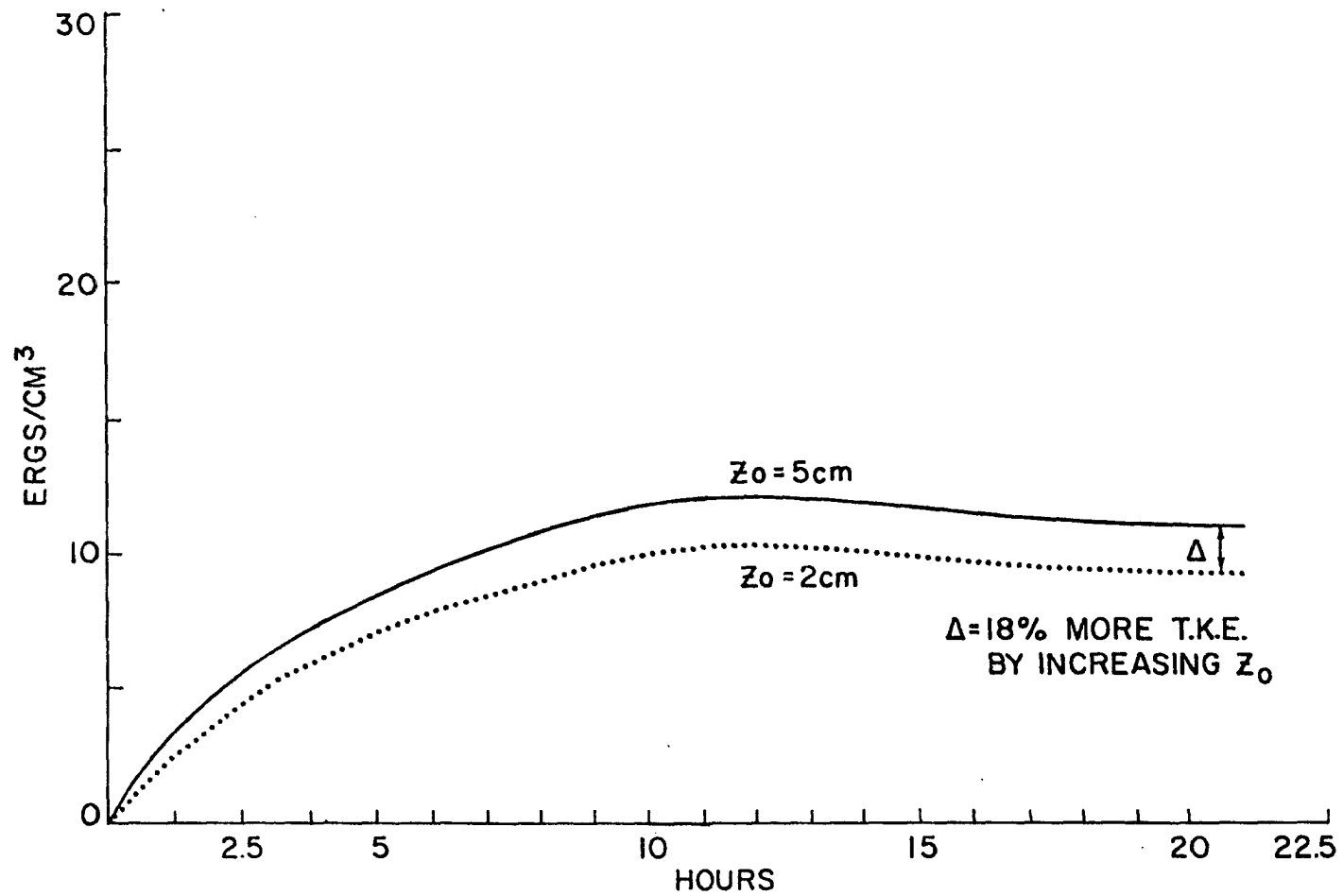


Figure 4-9. Vertically averaged Turbulent Kinetic Energy (T.K.E.) as a function of time of integration for $z_0 = 2.0$ cm (dotted) and $z_0 = 5.0$ cm (solid) for the neutrally stratified case study.

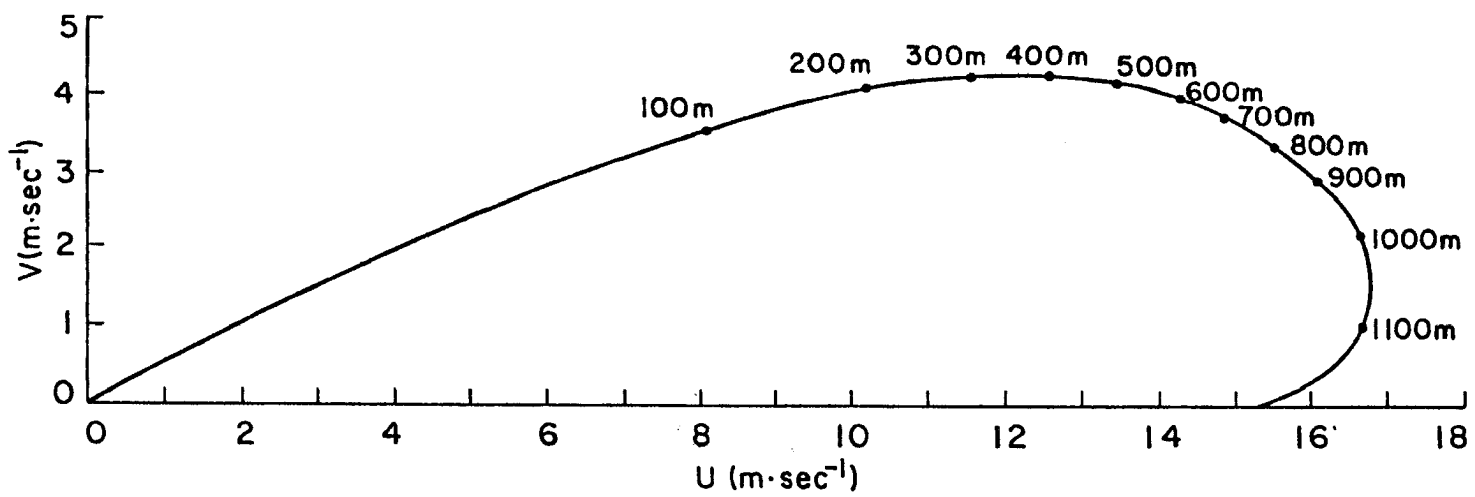


Figure 4-10a. Traditional Ekman spiral from first-order theory.

degree of frictional turning in the surface layer of approximately 26° east of north. Figure 4-10b exhibits a similar plot of \bar{u} and \bar{v} from the Manton-Cotton model. Of immediate interest is the maintenance of the overall spiral shape, indicative of an overall movement of mass with a component against the pressure gradient. However, the degree of frictional turning is much less and constant through the surface layer, as would be expected. The other significant difference is that the position of the height points is much further around on the spiral than in the eddy viscosity case. In this case the u-component of the wind is only slightly more than 50% of the geostrophic value whereas in the higher order model, it is approximately 85% of its geostrophic value. A simple comparison between the two is insufficient to make any conclusion at all as to which is the better model; both cases are descriptive of an atmosphere which is rarely if ever experienced.

Observational evidence to support the computational results of a horizontally-homogeneous model in a neutral stratification is extremely difficult to get. In general, the observed structure of the planetary boundary layer is not taken in a horizontally-homogeneous atmosphere. However, two studies, one by Mendenhall (1967) and the second by Gray (1972) of very large data sets have attempted to establish the degree of frictional veering in the planetary boundary layer. Both studies have attempted to arrive at an estimate of the frictional turning of the wind in the planetary boundary layer by systematically analyzing for and eliminating other causes of turning, e.g. large scale thermal advection. Mendenhall concludes that the actual frictional veering of the winds over the oceans is about 10° ; and over land, 20° . Gray, after analyzing over 100,000 pibal and

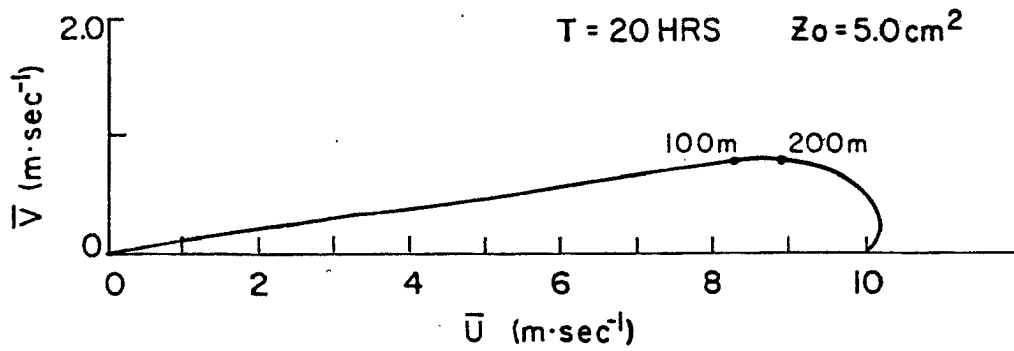
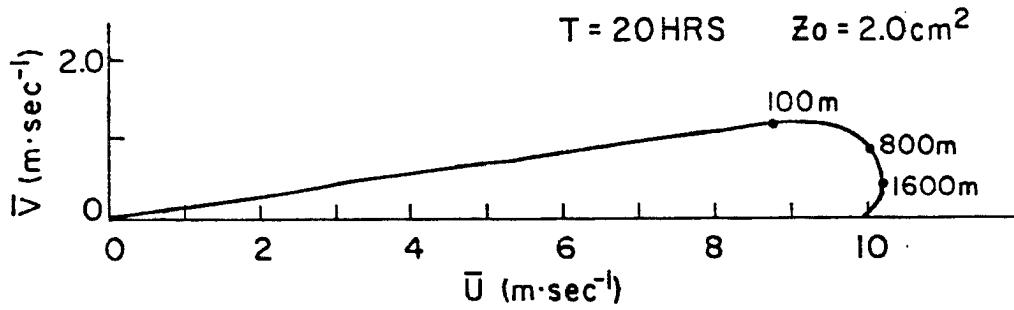


Figure 4-10b. Ekman spiral as calculated for $z_0 = 2.0 \text{ cm}$ (upper) and $z_0 = 5.0 \text{ cm}$ (lower) at $T = 20$ hours for the neutrally stratified case study.

rawinsondes observations finds an average veering in lowest kilometer of 8-12 degrees and 0-3 degrees in the second kilometer thick layer above the surface. To the extent that their analysis methods approximate the degree of horizontal-homogeneity imposed upon this model, the results of this model tend to look more and more realistic, more so than the first order model. The established increased frictional turning over land supports the models results of increased turning with increase in roughness length, since the land with an irregular surface, would lead to an overall bigger effective z_0 in the horizontally-homogeneous limit.

The important consideration of this evaluation is the effect of buoyancy upon the model derived structure of the planetary boundary layer. A discussion of this in the context of the observations made as part of the Wangara Experiment (Clark, et.al., 1971) follows.

4.3 Wangara Day 33 Case Study

Day 33 (16th of August, 1967) of the Wangara Experiment has been used by a number of authors to evaluate their modelling efforts (e.g., Deardorff 1974a,b; Wyngaard and Cote 1974; Pielke and Mahrer 1975; Yamada and Mellor 1975; Mahrt and Lenschow 1976; Zeman and Tennekes 1977). Several of these attempts, specifically Wyngaard and Cote and Yamada and Mellor, used some form of higher order closure in their model.

This particular day was an absolutely clear winter day over the plains of southeastern Australia, Hay N.S.W., Australia, 35°S , to be exact, with light winds and dry soil. It has been chosen by many authors because of the marked lack of baroclinic activity and large scale advection of heat and moisture, thus coming as close to horizontal homogeneity as is possible in any extant data set. There was evidence

of some large scale subsidence, however ($0.01-0.02 \text{ m}\cdot\text{sec}^{-1}$) during the middle of the afternoon.

4.3.1 Description of Day 33

Three-hourly profiles of $\bar{\theta}$ measured during Day 33 are shown in Figure 4-11 beginning at 0600 local time. Sunrise was at 0712 local time. The 0600 sounding shows a strong night-time radiation induced surface inversion below a well mixed layer, most likely a remnant of the previous day. The well mixed layer is capped by a stable temperature inversion, possibly due to large-scale subsidence. The progression of daytime heating is seen first to destroy the surface stable layer and then to heat the well mixed layer uniformly. By 1800, 45 minutes after sunset, the night-time radiation surface inversion is seen to be forming. The warming of the profiles above the mixed layer can be attributed to the mean subsidence as evidenced on Day 33. For additional comment and analysis of the mean vertical velocity pattern, the reader is referred to Hess and Clark (1973) and Yamada and Mellor (1975). It suffices here only to take notice of the fact that a mean subsidence of about $2 \text{ cm}\cdot\text{sec}^{-1}$ was observed. Because of this subsidence in the afternoon, the rate of deepening of the well-mixed layer was considerably slowed.

Figure 4-12 shows profiles of the mean wind at 0600L and 0900L. Superimposed upon the 0900 profile is the geostrophic wind profiles as determined from thermal wind corrections taken 0-1 km and 1-2 km as estimated from Bureau of Meteorology rawinsonde network. A time plot of the surface geostrophic wind is shown in Figure 4-13. These values have been estimated from a 19 station network over southeastern Australia. Though somewhat noisy, definite trends are easily identifiable.

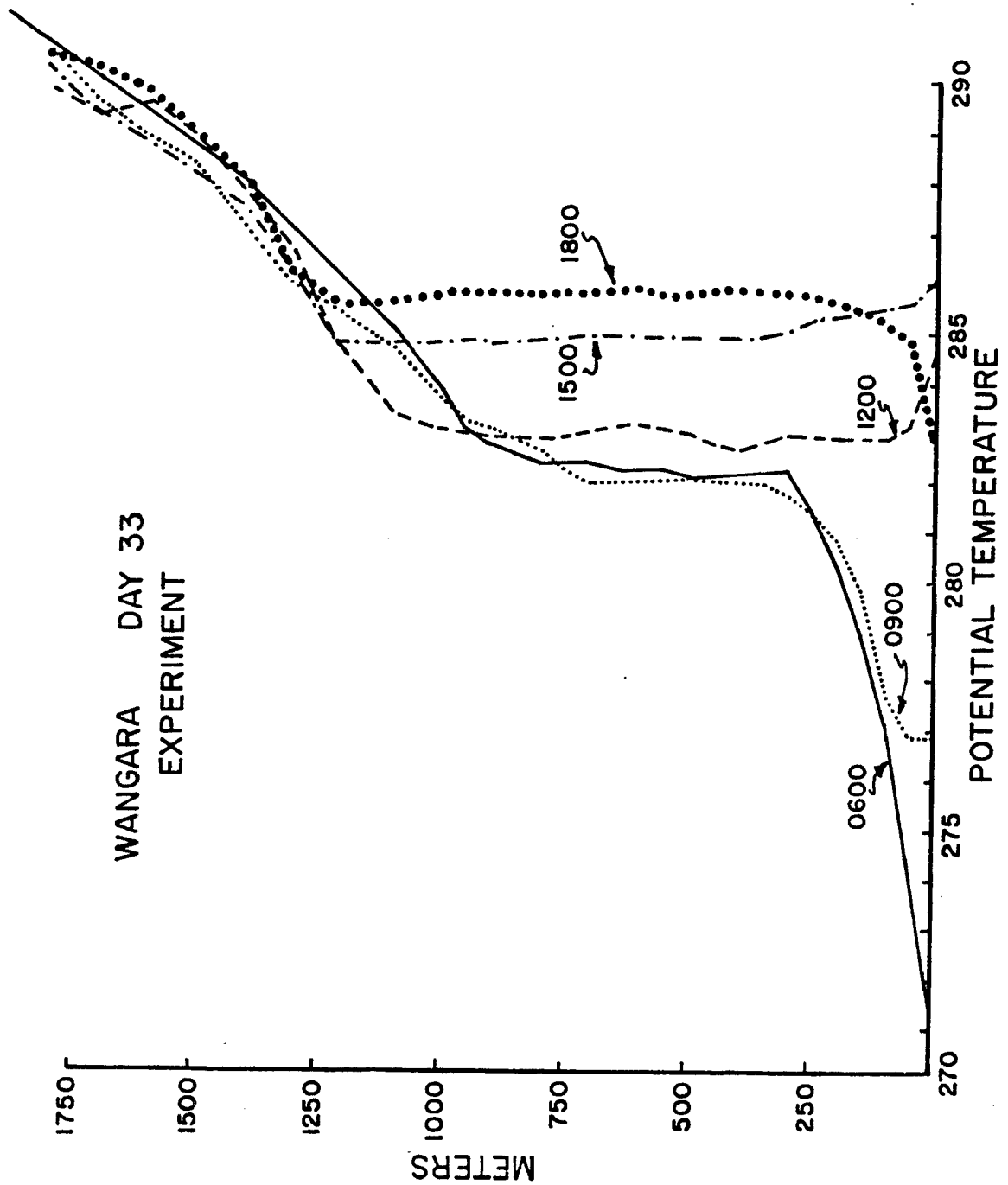


Figure 4-11. Observed three-hourly vertical profiles of potential temperature, beginning at 0600 LST on Day 33 of the Wangara Experiment (Clarke, et. al. 1971).

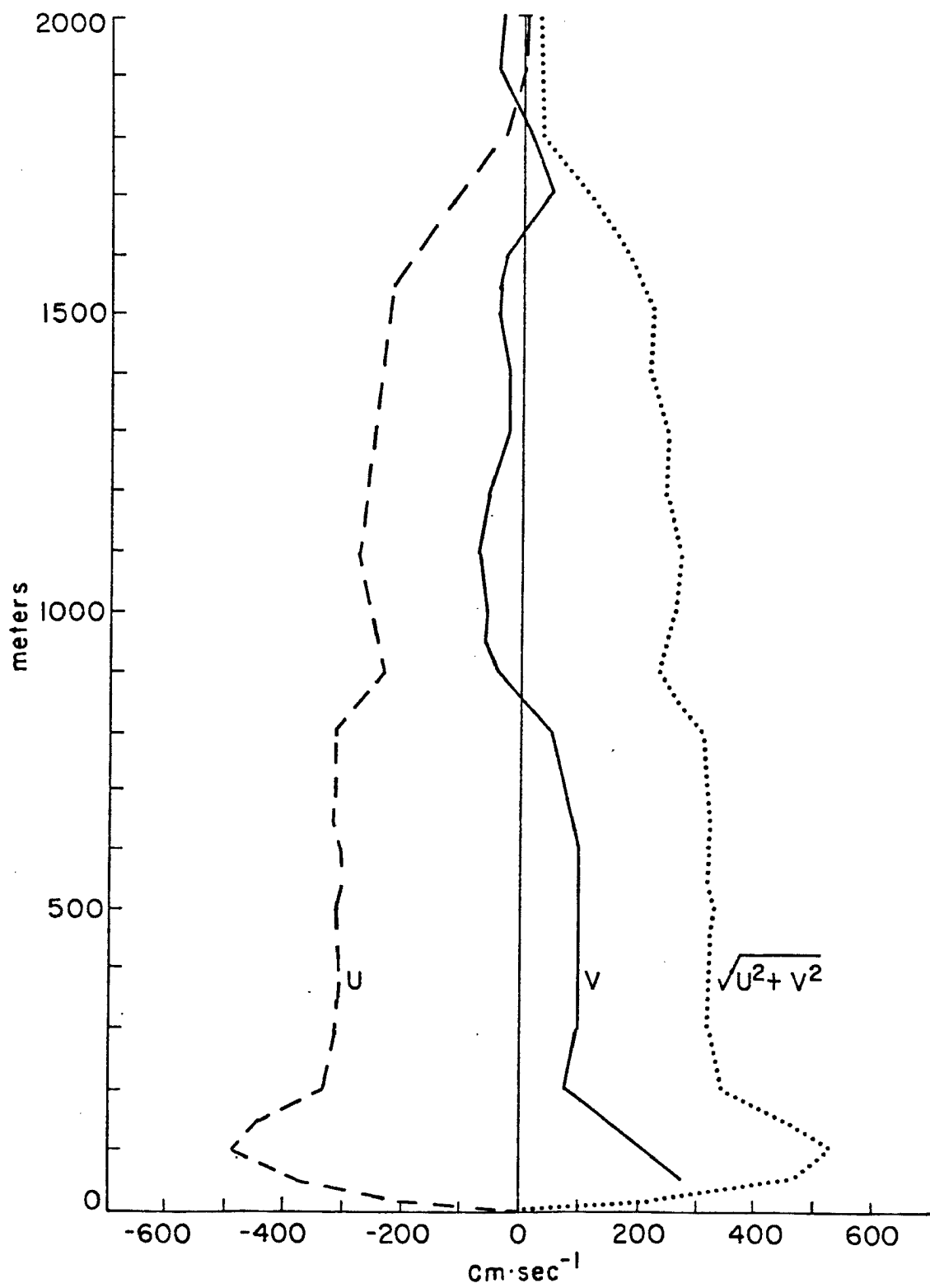


Figure 4-12a. Observed vertical profiles of the u and v components of the mean wind at 0600LST and 0900LST.

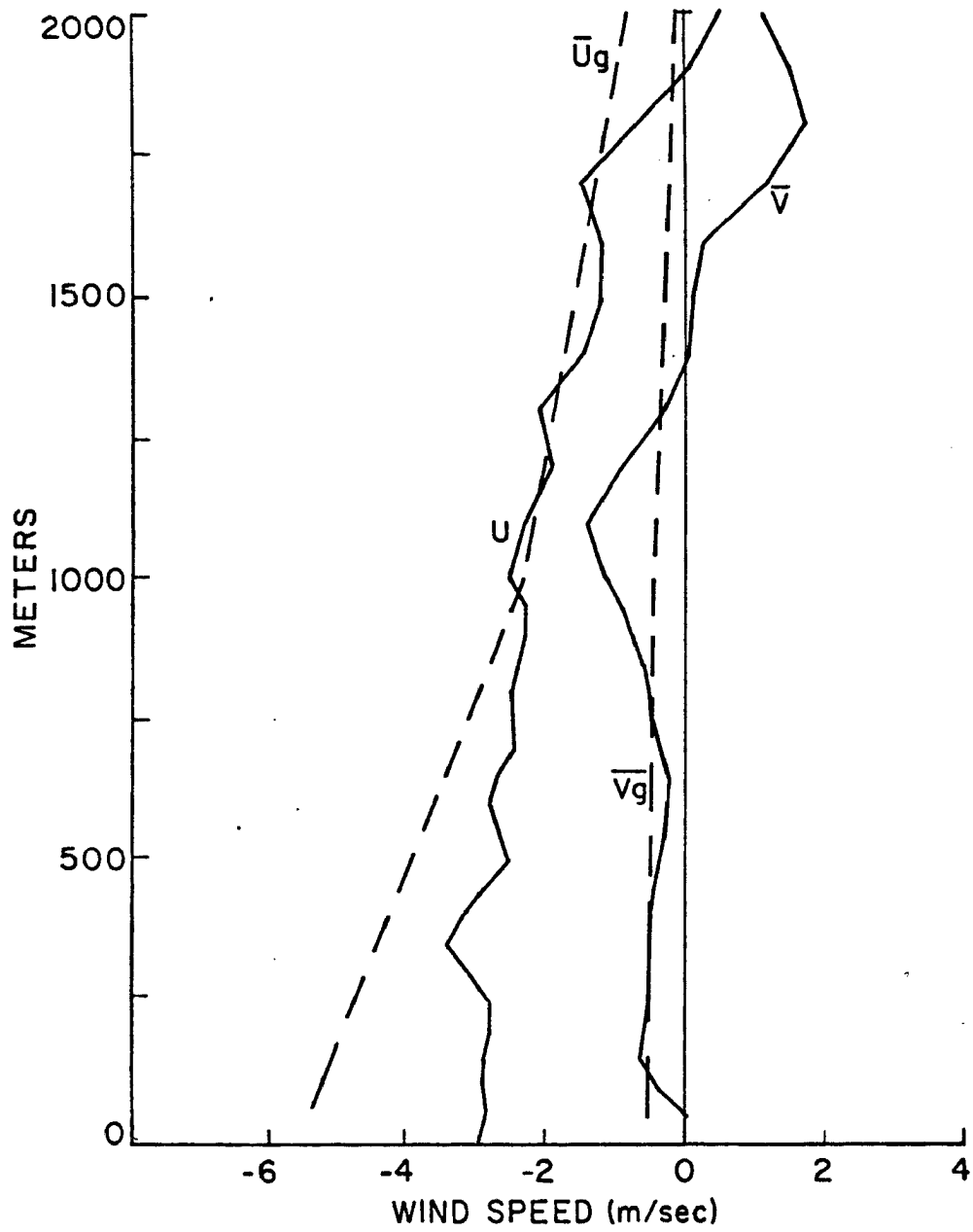


Figure 4-12b. Superimposed upon the 0900 profile is the vertical profile of the geostrophic wind derived from the observed thermal wind.

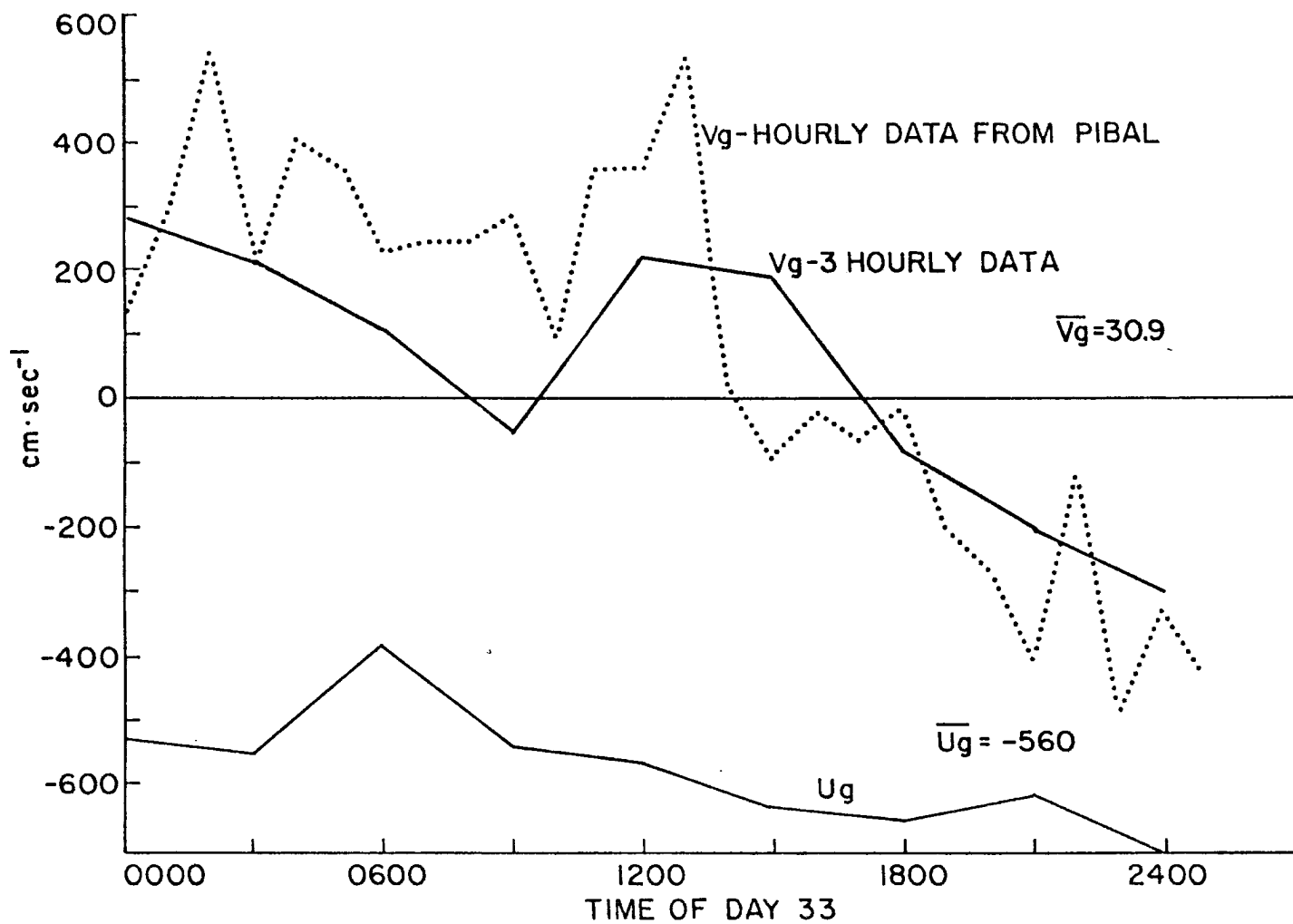


Figure 4-13. Observed time series of the observed surface geostrophic wind components for Day 33 of the Wangara Experiment.

The time and space variation of the observed mean easterly and northerly winds has been analyzed for a 48 hour period, beginning 0900L on Day 33. (See Yamada and Mellor, 1975) This analysis shows the column average (0 to 1.5 km) of the easterly component of the wind increasing from a magnitude of $3 \text{ m}\cdot\text{sec}^{-1}$ to greater than $8 \text{ m}\cdot\text{sec}^{-1}$ by 2100. The development of a nocturnal jet with a $12.8 \text{ m}\cdot\text{sec}^{-1}$ maximum between midnight and 0600L on Day 34 is also apparent. The development of the nocturnal jet occurred at a height of 100 to 500 m. The north-south wind component was generally southerly throughout the day, but of generally weak magnitude, $< 2 \text{ m}\cdot\text{sec}^{-1}$. Between 1800L and midnight, the wind direction became northerly first in the upper part of the layer and later through the depth of the layer. Eventually a magnitude of over $4 \text{ m}\cdot\text{sec}^{-1}$ was attained during the early morning hours of Day 34. The development of a low level wind maxima is evident during the hours of darkness. Yamada and Mellor (1975) claim that this nocturnal jet develops as a consequence of free inertial oscillations, as explained by Blackadar (1957), that occur after sunset when Reynolds stresses vanish.

4.3.2 Model Initialization

4.3.2.1 Profiles

The initial profiles of mean potential temperature and momentum for the model integration were taken from the 0600L central site temperature sounding. This was done in an attempt to eliminate problems with the initialization of flux profiles of momentum and temperature, and to more fully describe the evolution of the convective boundary layer. Other simulation studies of this day, e.g. Deardorff, Yamada and Mellor, Wyngaard and Cote, were initialized with the 0900 sounding, approximately

1 hour, 45 minutes after sunrise. Previous results with this model have shown that an hour or more of integration time was necessary to stabilize the flux profiles in a neutral atmosphere. Therefore it was tentatively concluded that the best method of initialization was to initialize the profiles in the absence of ongoing convective flux. Accordingly, profiles of second-moment quantities were set identically zero in the stable atmosphere prior to sunrise. The integration then began at sunrise, assumed to be 0715L, and continued until 2100L, 13.75 hours. No other initialization was attempted because: 1) no data were available in the presence of convection; and 2) 0-fields of the covariances and variances are the best estimate in a stably stratified atmosphere, since the stable stratification quickly and not nicely damps vertical momentum variance.

The geostrophic wind was taken to be constant over the time of integration with value of :

$$\begin{aligned}\bar{u}_g &= -5.5 \text{ m}\cdot\text{sec}^{-1} \\ \bar{v}_g &= +1.0 \text{ m}\cdot\text{sec}^{-1}\end{aligned}$$

These values were taken to be representative of Day 33 from Figure 4-13. This geostrophic wind with the initial wind profile from the 0600L sounding does allow inertial accelerations of the mean momentum field.

4.3.2.2 Model Forcing

Realistic simulation of the development of the planetary boundary layer necessitates proper modeling of not only the spatial characteristics of the forcing, but also the temporal.

As discussed previously, the lower boundary condition of this model is the Manton-Cotton surface layer parameterization scheme. However, realistic values of the momentum and heat flux must be obtained in order for this scheme to work. Further, the rate at which the boundary layer convectively warms and the inversion rises is directly dependent upon the time variation of the magnitude of the surface heat flux. Use of the Manton-Cotton scheme requires specification of the surface θ at a height of z_0 above the surface. Unfortunately, no measurements were made at this level during the Wangara Experiment. Deardorff in his simulation studies of this day found it necessary to formulate equations for the surface thermal energy balance in order to deduce the surface temperature. (see Deardorff, 1974). The difference between the surface roughness-length height, z_0 and the surface was then estimated using a formula established by Zilitinkevich (1970). Other simulation studies (e.g., Pielke and Mahrer, 1975 and Wyngaard and Cote, (1974) found it convenient to simply use Deardorff's results -- i.e. temporal profiles of surface temperature or surface heat flux to force their models. Use of the Zilitinkevich formula involves knowledge of the surface-layer heat flux; so that any attempt to incorporate, as other authors have done, Deardorff's balance-equation derived surface temperatures into the Manton-Cotton scheme would involve some iterative computational coupling of the Zilitinkevich formula with the equations (3.24) and (3.25). A simpler more straight-forward technique is to use the measured screen height temperature from the Wangara Data to deduce $\theta(z_0)$. This method has the advantage of eliminating any possible computational inconsistency that might occur in coupling

the Zilitinkevich formula with the Monin-Yaglom similarity functions. Briefly, the procedure is as follows:

For given values of the surface fluxes of heat and momentum, two points on each curve (equations 3.24 and 3.25) uniquely specify the distribution of heat and momentum in the surface layer. However, in equation 3.25, it is not necessary that one of the two specified temperatures be $\theta(z_0)$. It is possible to manipulate equation 3.24 so that the measured screen height temperature can be used instead, to uniquely determine the profile of potential temperature in the surface layer. Then knowing the profile, $\theta(z_0)$ can be deduced. Equations 3.24 and 3.25 can then be inverted by the interactive process described in section 3.3.2 to obtain new values of the surface fluxes of heat and momentum. The measured screen height-temperature can thereby be used to provide the external forcing for the Wangara Day 33 simulation.

4.3.3 Results of Integration

Figures 4-14 and 4-15 respectively show time plots of measured screen height (1.2m) temperature and model diagnosed surface θ (at $z=z_0$); and model diagnosed surface friction velocity and heat flux. These curves are predicted by the Manton-Cotton surface layer scheme using the time varying curve of measured screen height temperature as the model input. Of immediate interest is the one-to-one correspondence between the curves of surface θ and surface heat flux. The oscillatory peaks in the first four hours of integration are directly related; as are the smoothly varying trends of the next six hours. Peaks in the curve of surface θ can be seen to be directly related to changes in the slope of the screen height temperature. There is a strong implication that

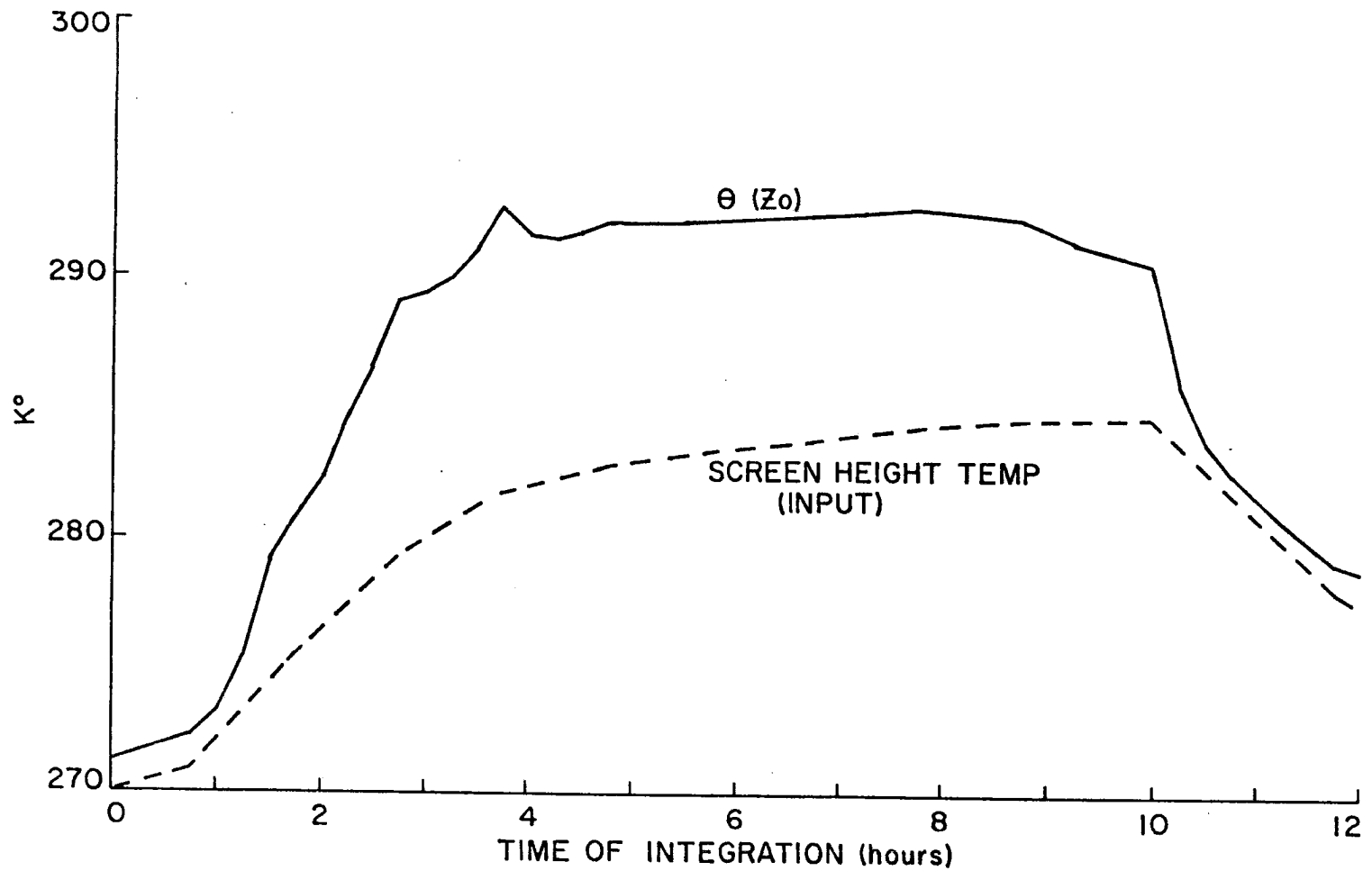


Figure 4-14. Variation of the diagnosed surface $\theta(z=z_0)$ and the observed screen height temperature as a function of time of integration. 0=0715LST.

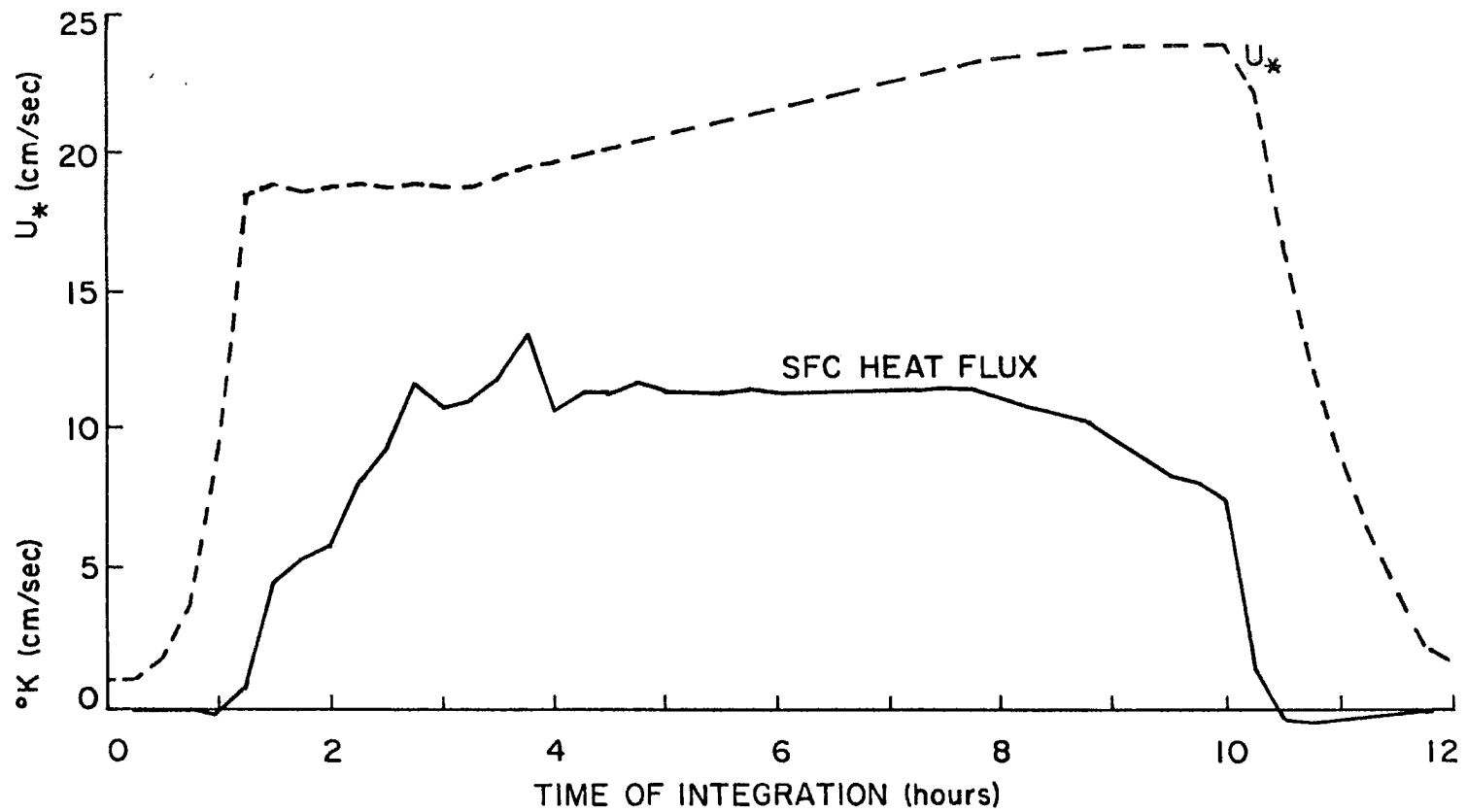


Figure 4-15. Variation of the diagnosed surface heat flux (solid) and friction velocity as a function of time of integration.

the time derivatives of screen height temperature and surface θ are not related linearly and that the peaks seen in surface θ are not real but due to abrupt though small changes in the time derivative of the screen height temperature. If screen height temperature was input as smoothly varying (i.e., the time derivative was continuous (mathematically) in time) as might be obtained from a sinusoidal or best fit curve, these abrupt changes in the time derivative of surface θ , and hence in the surface heat flux, would be eliminated.

The time variation of the surface stress is seen to be coupled with that of the surface heat flux but in a somewhat different manner. The friction velocity is seen to approach an equilibrium value in a comparatively shorter time than the heat flux (1.25 hrs.) and then is seen to hold that value during the next two hours of integration time, while the heat flux increases from essentially zero, to its equilibrium value. The trends then are again reversed. The surface heat flux holds its equilibrium until approximately mid-afternoon and then begins to drop off slowly until sunset, at which time, it drops rapidly to near zero or slightly negative. The friction velocity, in the meantime, increased linearly in time, while the heat flux was essentially constant (3 1/2 to 8 hrs.) and then increased at a decreasing rate when the heat flux began to decrease until sunset; then both drop rapidly to small values. This steady increase can be seen to be directly related to the slow increase of mean momentum in the well-mixed layer during the day. Figure 4-16 is a time plot of model predicted, \bar{u} , and \bar{v} at the lowest model grid point (ZM(1)). Comparing Figure 4-15 and Figure 4-16, the slow rise in u_* during the day can be directly attributed, in part, to the slow rise in the mean momentum of the layer. The change in the slope

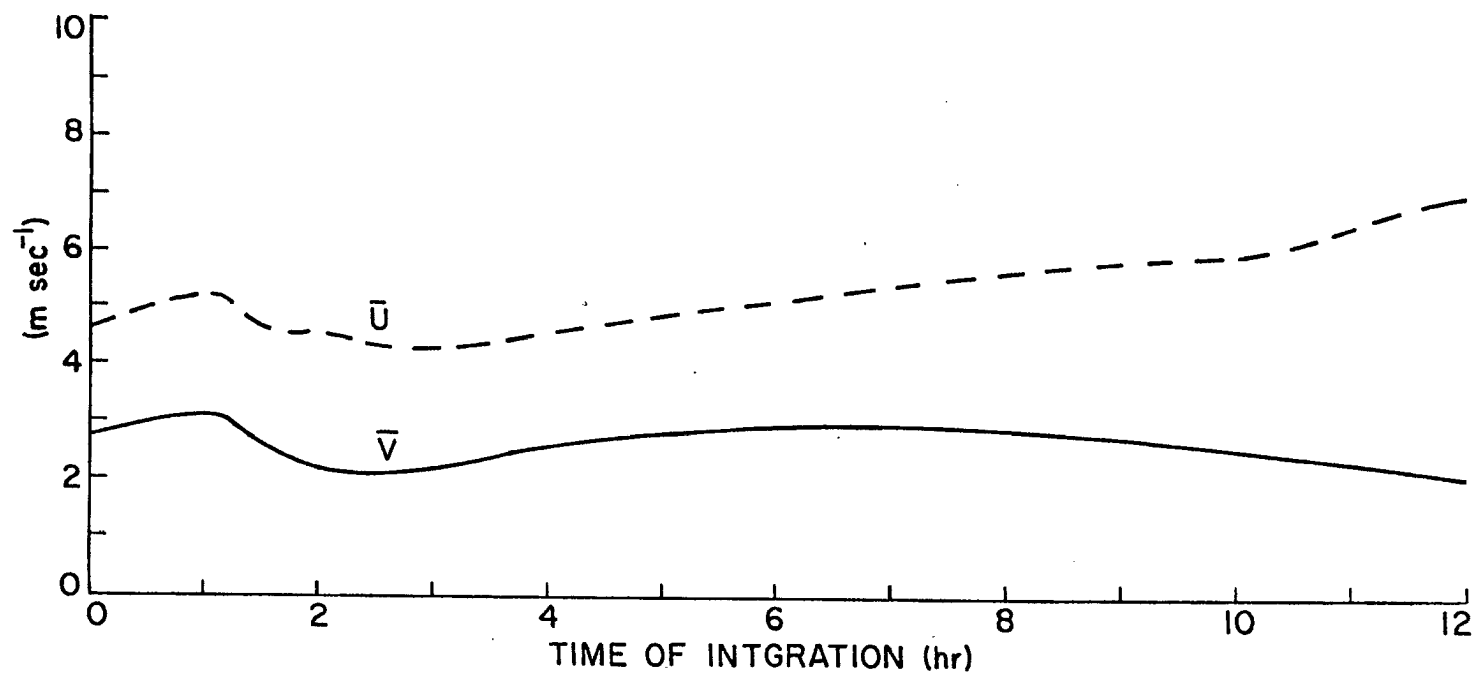


Figure 4-16. Computed mean/momentum components at $z=50\text{m}$ as a function of time of integration for the Wangara Experiment, Day 33 simulation.

of the curve for \bar{u} at $t=10$ hrs. can be related to the rapid decrease in surface stress after sunset. It can be interpreted as a lessening of the angle of frictional turning directly attributable to the rapid decrease in surface stress.

Figures 4-17 and 4-18, respectively, show vertical profiles of the mean wind, \bar{u} and \bar{v} , at various times. The mean east-west component is seen to increase steadily throughout the day. By early evening, it is easterly with a magnitude of over $7 \text{ m}\cdot\text{sec}^{-1}$. The mean southerly component, however, is seen to increase to a maximum during mid-afternoon and then to decrease to near its geostrophic value in early evening. In each profile, the presence of the inversion capping the well mixed layer is very apparent. Comparing the profiles at $T=10$ hours (at sunset and time of maximum surface stress) and at $T=13.75$ hours (early evening), the effect of the rapid drop in surface stress is easily seen in the change in the shape of the profile, as it has become more nearly constant with height. Since the model was not initialized to be in inertial balance, the large changes in \bar{u} and \bar{v} above the inversion can most likely be attributed to a large magnitude inertial oscillation. This inertial oscillation is also apparent below the inversion but of a different magnitude. However, the increase in magnitude of \bar{u} and \bar{v} during the time of daytime heating is primarily due to the heating of the layer.

The time evolution of the mean $\bar{\theta}$ profile is shown in Figure 4-19. The model was initialized with the 0600LST sounding and the integration began at sunrise (0712LST). The magnitude of the profile after 2 hours and 5 hours respectively agrees fairly well with the observed profiles at 0900 and 1200L. However, by 8 hours the warming of the layer does not keep pace with the observed warming. The predicted $\bar{\theta}$ was on the average

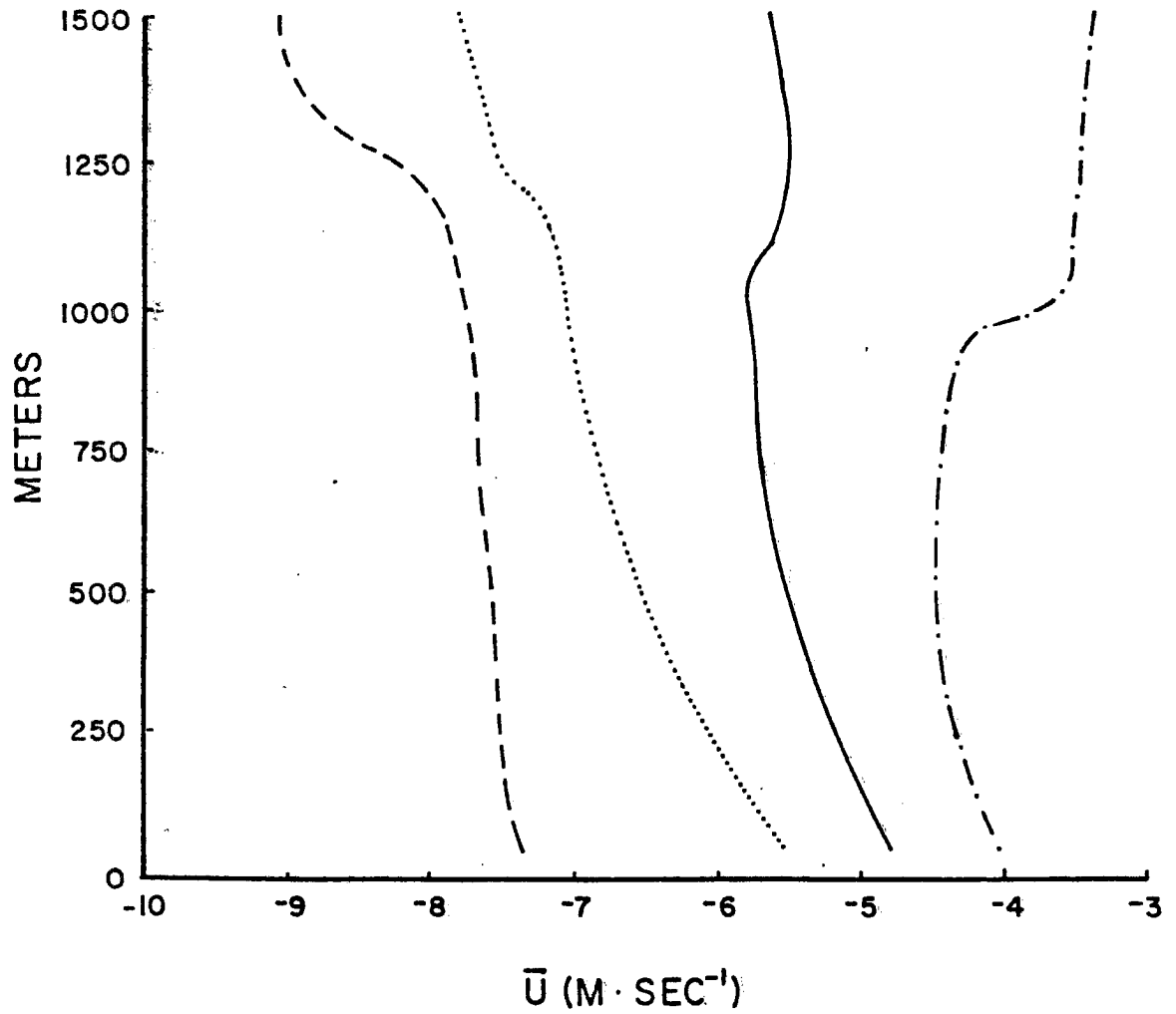


Figure 4-17. Computed vertical profiles of \bar{u} at $T=5$ hours (dash-dot), $T=7.5$ hours (solid), $T=10$ hours (dotted), and $T=13.75$ hours (dashed).

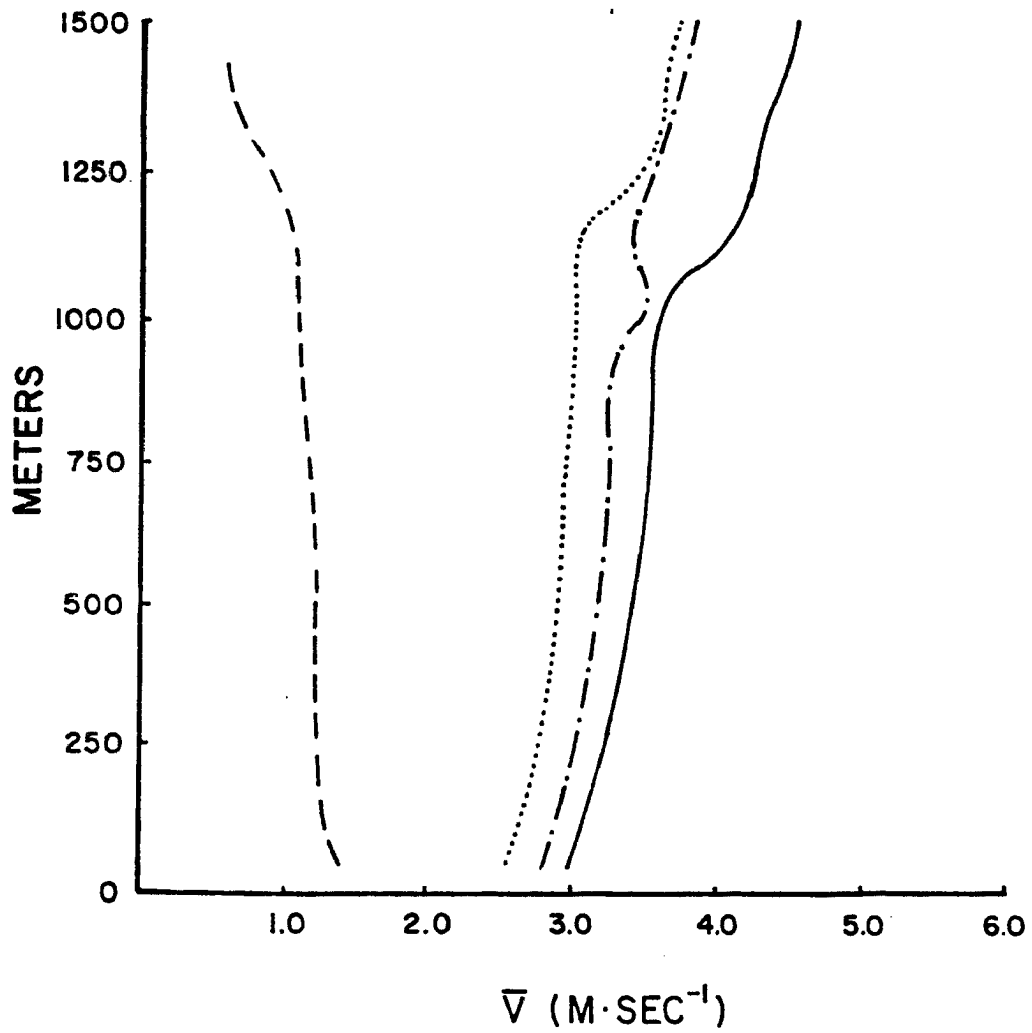


Figure 4-18. Same as in Figure 4-17, except for \bar{v} .

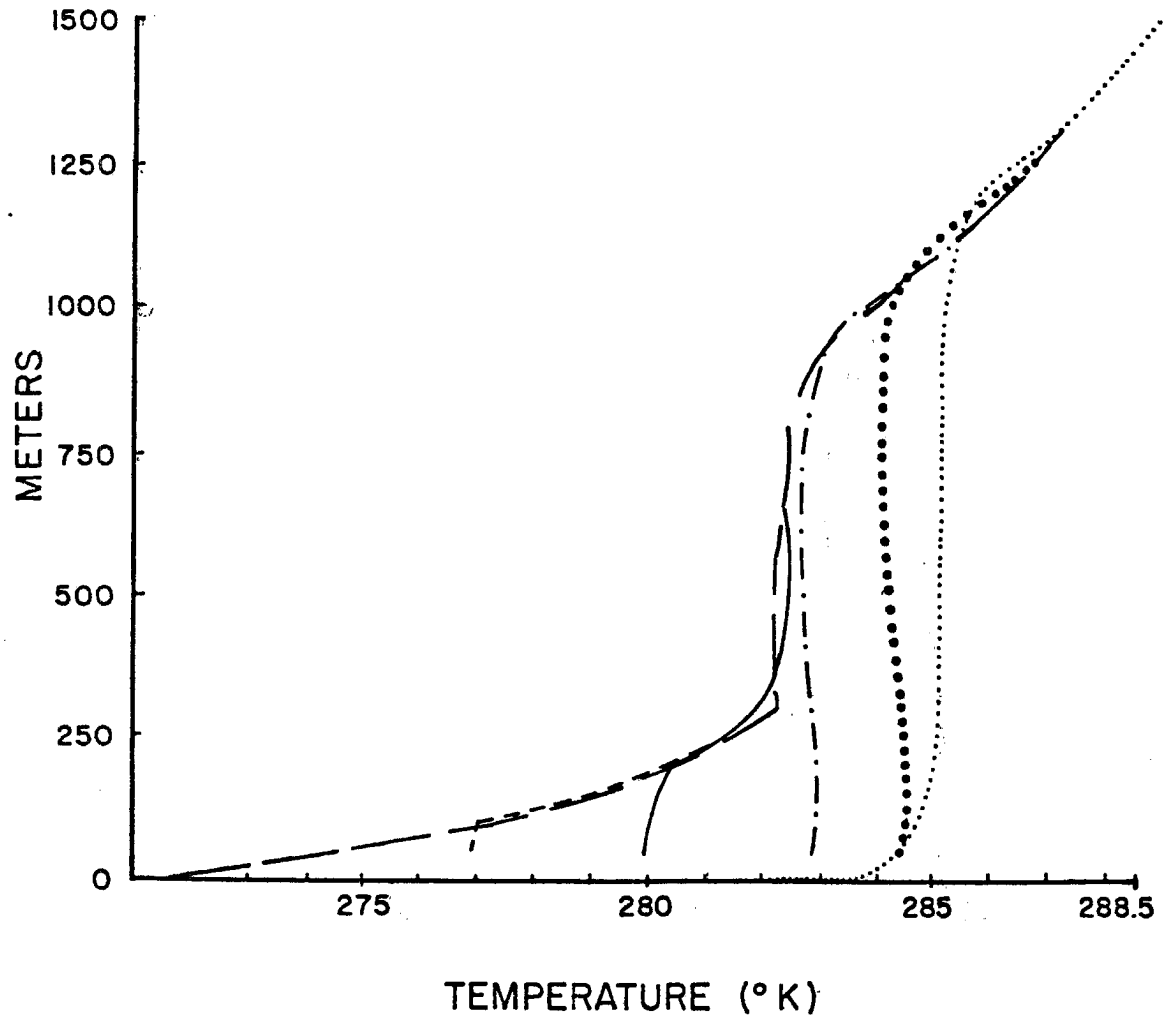


Figure 4-19. Initial (long-dash) and computed vertical profiles of mean potential temperature, θ , at T=2 hours (dashed), T=3 hours (solid), T=5 hours (dash-dot), T=8 hours (bold-dot) and T=11 hours (small-dot).

about a half degree C low at 1500LST and almost a full degree low at 1800LST, three quarters of an hour after sunset. Similar to Wyngaard and Cote (1974), the afternoon curves prior to sunset also show the tendency toward slight stability in the lowest few hundred meters. The observed sounding at 1200LST, exhibits cooling at a height above ground 1.0 to 1.2 km due, in large part, to entrainment of the warmer air above the inversion into the well mixed layer. The model response shows significantly less entrainment across the inversion, and in this author's opinion this is the primary causal mechanism for the under-prediction of the rate of height rise for the inversion. Figure 4-20 depicts model predicted turbulent flux profiles of θ . The most striking observation is the small magnitude of the negative flux at and above the inversion, approximately $0.25^\circ\text{Ccm}\cdot\text{sec}^{-1}$ at its greatest. The development of the slightly stable layer in the profiles of mean $\bar{\theta}$, can be seen to be caused by the decrease in slope of the flux profile in the bottom few hundred meters. The smoothness with which the flux profiles join with the diagnosed surface flux is very encouraging. Comparing the profiles at $T=10$ hours and $T=10.5$ hours, corresponding to sundown and sundown + 30 minutes, the smooth manner in which the predicted profile adjusts to the rapid drop in the surface flux is indicative of the model's internally consistent behavior.

Predicted flux profiles of momentum are shown in Figure 4-21. The profiles of $\overline{u''w''}$ are seen to be essentially linear during the day and then after sunset ($T=10$ hours) the bottom half of the profile is pulled back near zero. At the same time a positive magnitude in the interior of the layer is maintained which is seen to decrease gradually as the turbulence within the layer is dissipated. Above the capping inversion

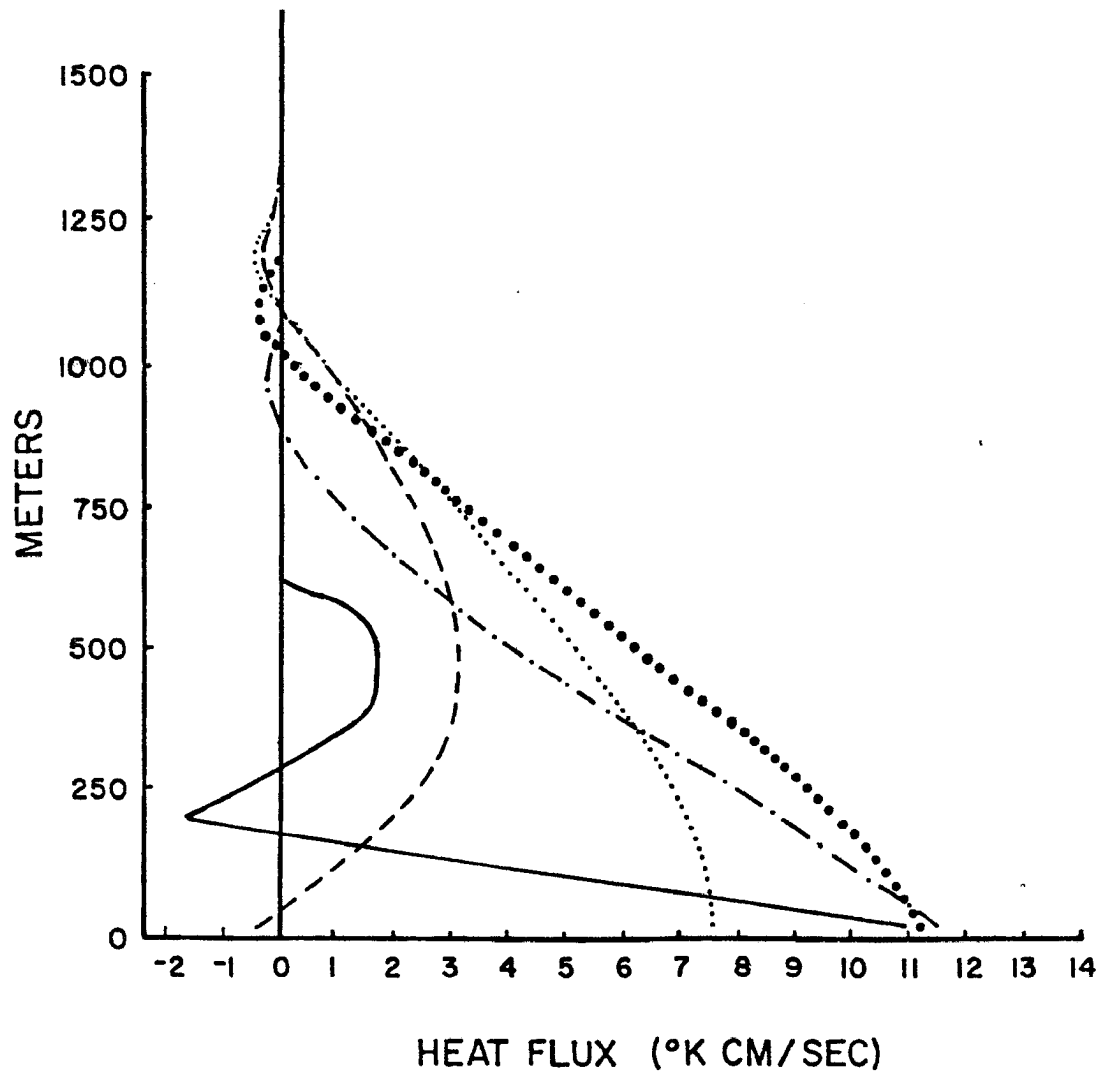


Figure 4-20. Computed vertical profiles of the vertical heat flux, $\theta''w''$ at T=3 hours (solid), T=5 hours (dash-dot), T=8 hours (bold-dot), T=10 hours (small-dot), and T=10.5 hours (dashed).

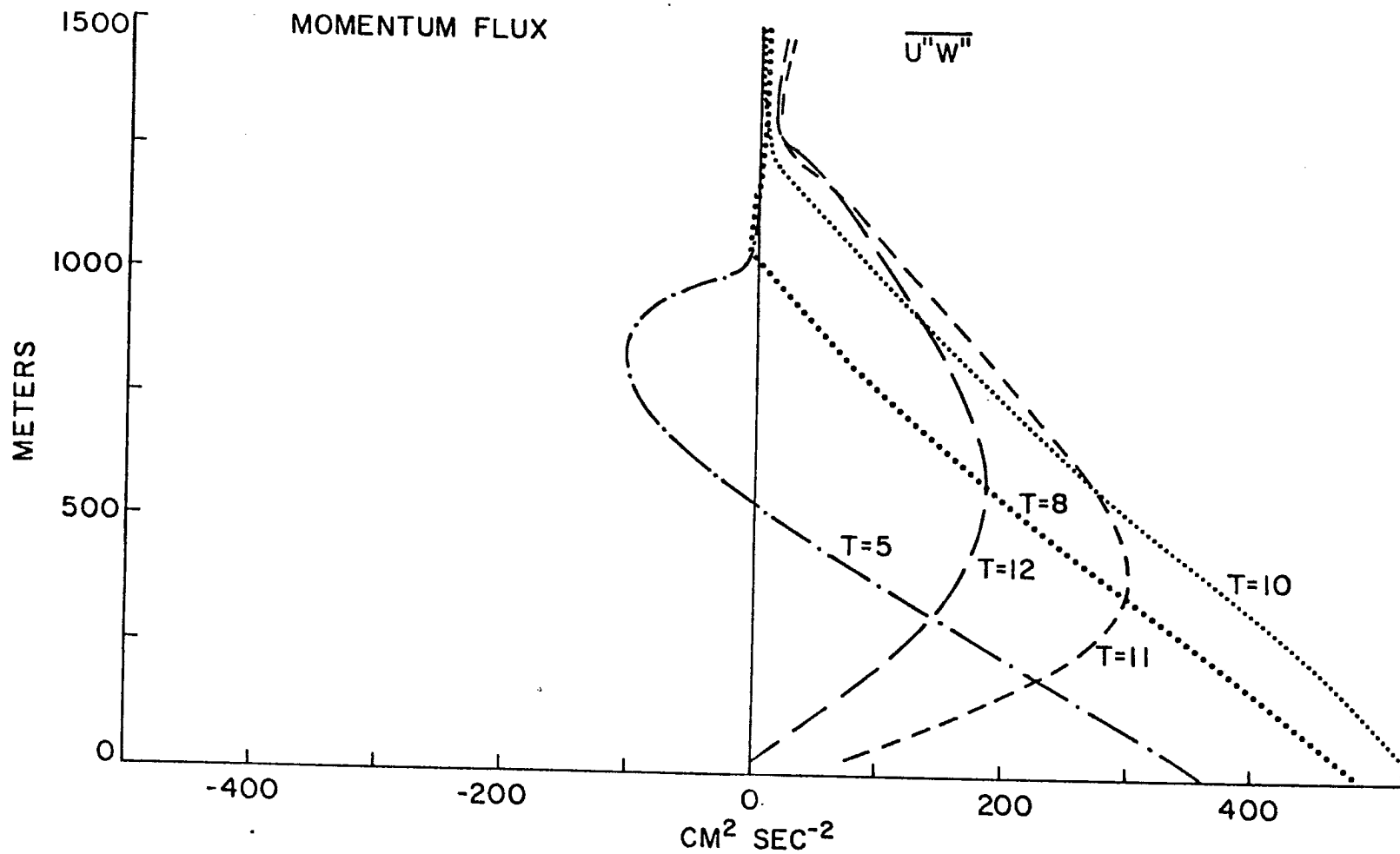


Figure 4-21a. Computed vertical profiles of turbulent momentum flux, $\overline{u''w''}$ at T=5 hours (dash-dot), T=8 hours (bold-dot), T=10 hours (small-dot), T=11 hours (short-dash) and T=12 hours (long-dash).

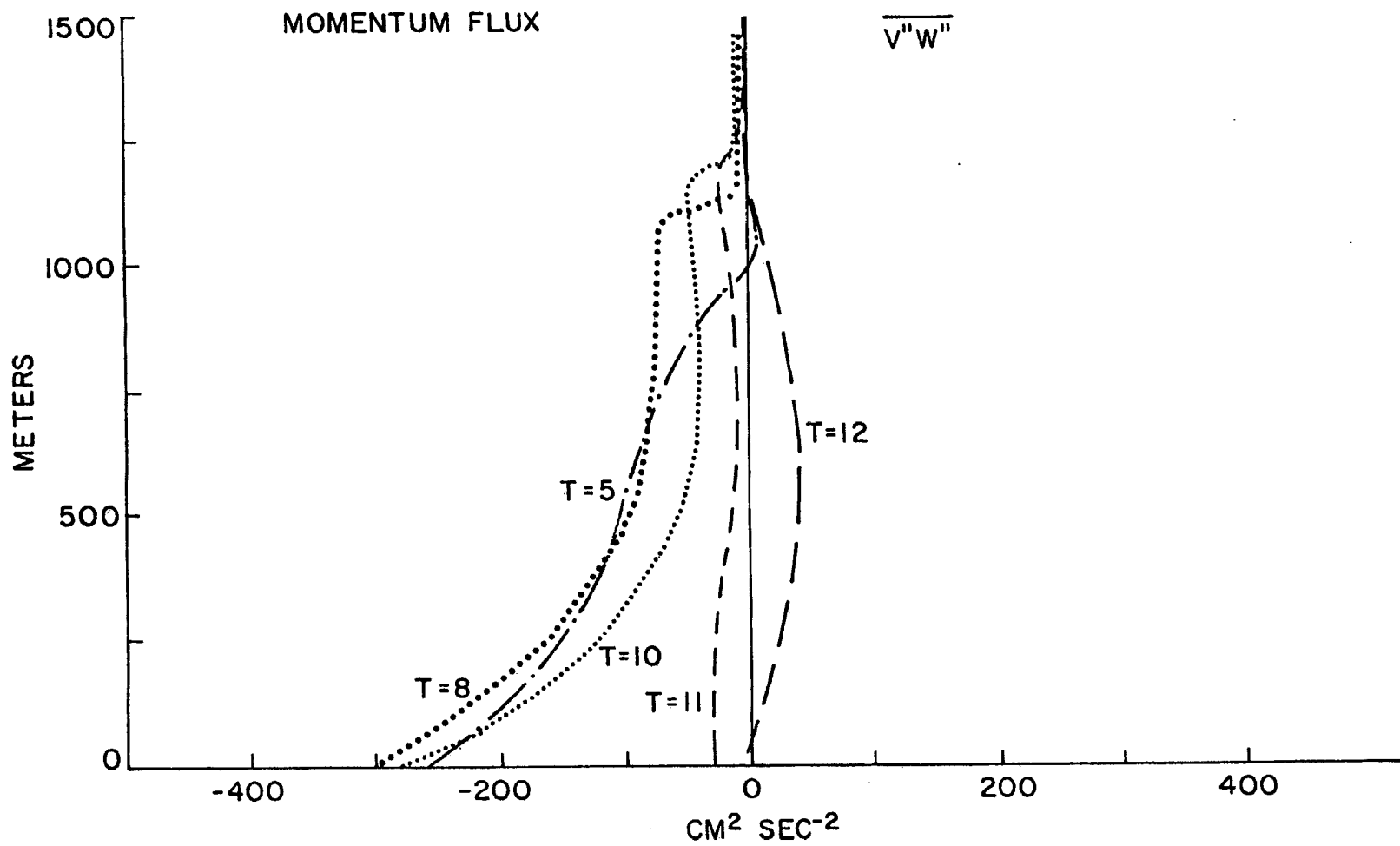


Figure 4-21b. Computed vertical profiles of turbulent momentum flux $\overline{v''w''}$ at T=5 hours (dash-dot), T=8 hours (bold-dot), T=10 hours (small-dot), T=11 hours (short-dash), and T=12 hours (long-dash).

the predicted profiles are seen to remain essentially zero. The effect of the inversion is seen only slightly in the shape of the curve for $\overline{u''w''}$; but, much more strongly in the profiles for $\overline{v''w''}$. The profiles of $\overline{v''w''}$ appear not to be linear in the well-mixed layer, but to decrease from the sub-inversion value slowly and then more rapidly to their surface values. After sunset, the profiles slowly decrease to zero and eventually change sign. Though zero at both the surface and inversion, the magnitude was seen to increase in the layer after sunset. The maintenance of a convergence zone of mean momentum in the well-mixed layer after sunset, as seen in the flux profiles of u and v is directly attributable to a sustained turbulent kinetic energy intensity in the layer, as shown in Figure 4-22. During the time of daytime heating, the profiles show a strong maximum at a height of approximately 200 meters which does not vary by more than 20% during the day. After sunset, the skewness of the curves is lost and the maximum is seen to move upward. The upper bound on the curves is again seen to be the inversion. Above the inversion, the curves decrease linearly from the value at the inversion. This is due to the diffusion of energy from below, since turbulent kinetic energy generation above the inversion is negligible. Figure 4-23 shows the horizontal and vertical components of the turbulent kinetic energy. Except near the inversion it is seen that the shape of the curves for the vertical and horizontal components are essentially the same with the horizontal less at all levels in the well mixed layer. At or just below the inversion, the magnitude of the vertical component is seen to be suppressed somewhat. This can be explained since the biggest generation term in the well-mixed layer is buoyancy which acts only in the vertical component. The

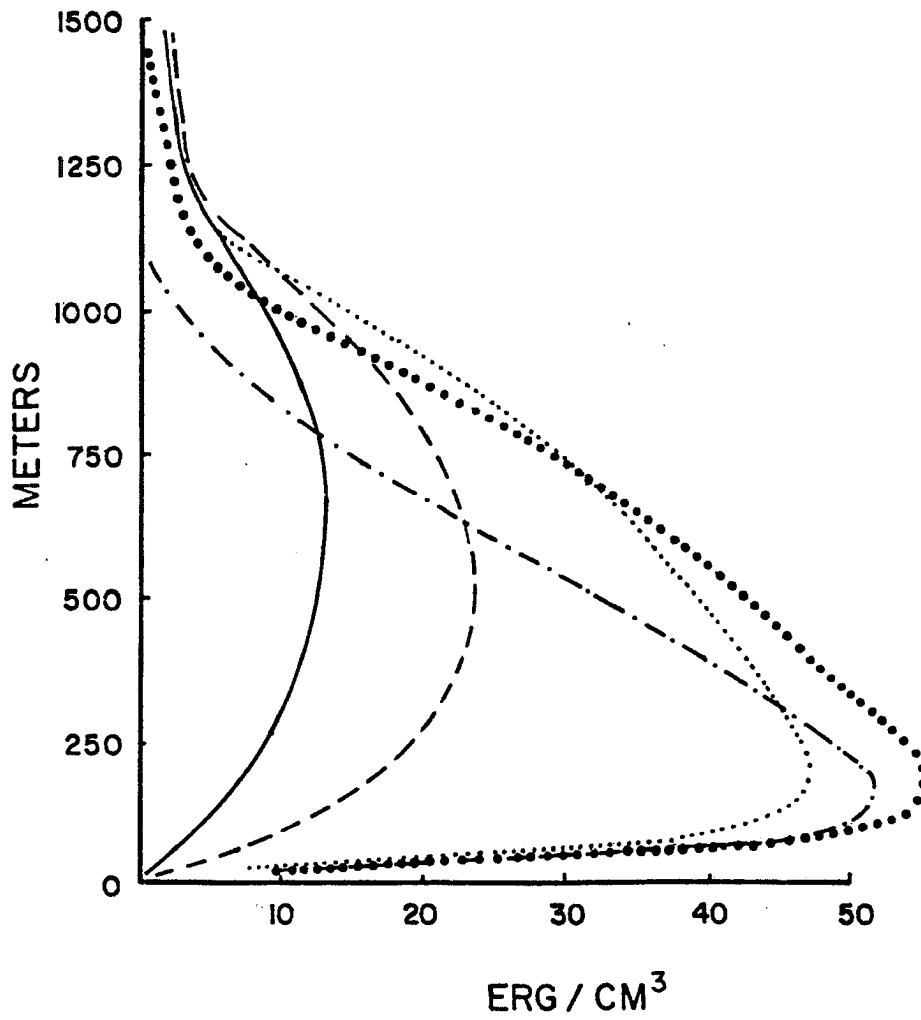


Figure 4-22. Same as in Figure 4-21 except for the Turbulent Kinetic Energy, $\rho_0 \overline{q^2}$.

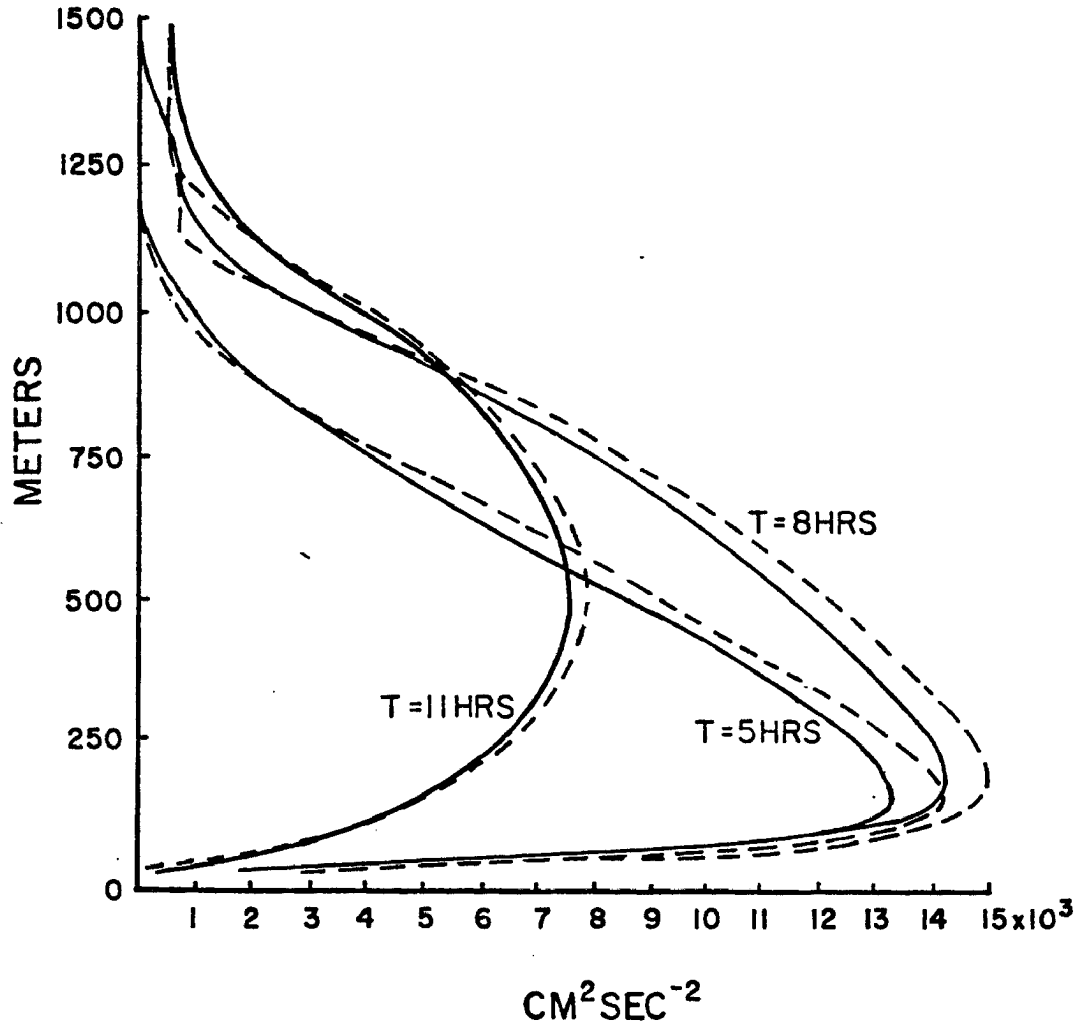


Figure 4-23. Predicted profiles of the vertical velocity variance, $w''w''$ (dashed) and horizontal velocity variance, $(u''u'' + v''v'')/2$ at T=5 hours (lowest maximum), T=8 hours (middle maximum) and T=11 hours (highest maximum).

mechanical generation term, which acts only in the horizontal, has magnitude only near the inversion since the greatest vertical shear of the horizontal wind shown in Figures 4-17 and 4-18 is at the inversion.

Figure 4-24 depicts profiles of predicted θ variance. During active convection these profiles show a pronounced bimodal structure in definite contrast to the momentum variance profiles which maintained a unimodal structure throughout the day. The existence of the lower maximum elevated several hundred meters above the surface appears to be unrealistic. The zeros in the vertical derivative of the θ variance profile are seen to correspond with the zeros in the vertical derivatives for the profiles of $\bar{\theta}$ and $\overline{\theta''w''}$. The existence, therefore of a lower maximum at a height above the surface must be due to a slightly stable layer above the ground in the presence of active convection. A more realistic shape would be for a maximum at the surface (i.e., in the surface layer). The post-sunset (T=11 hours) $\bar{\theta}$ profile is stable in the lowest few hundred meters due to surface cooling, but the corresponding variance profile shows its lower maximum at the surface. This is most likely because the surface heat fluxes are essentially zero at this time.

Profiles of the turbulent time scale are shown in Figure 4-25. Surface layer values are seen not to vary significantly during the time period of integration. The mixed layer values are surprisingly constant during the daylight hours. After sunset the development of the stable layer near the surface is reflected in the generation of secondary maximum at the second grid point above the surface layer. The fact that this lower maximum does not occur at the surface can be related to the "large" wind shear in the surface layer.

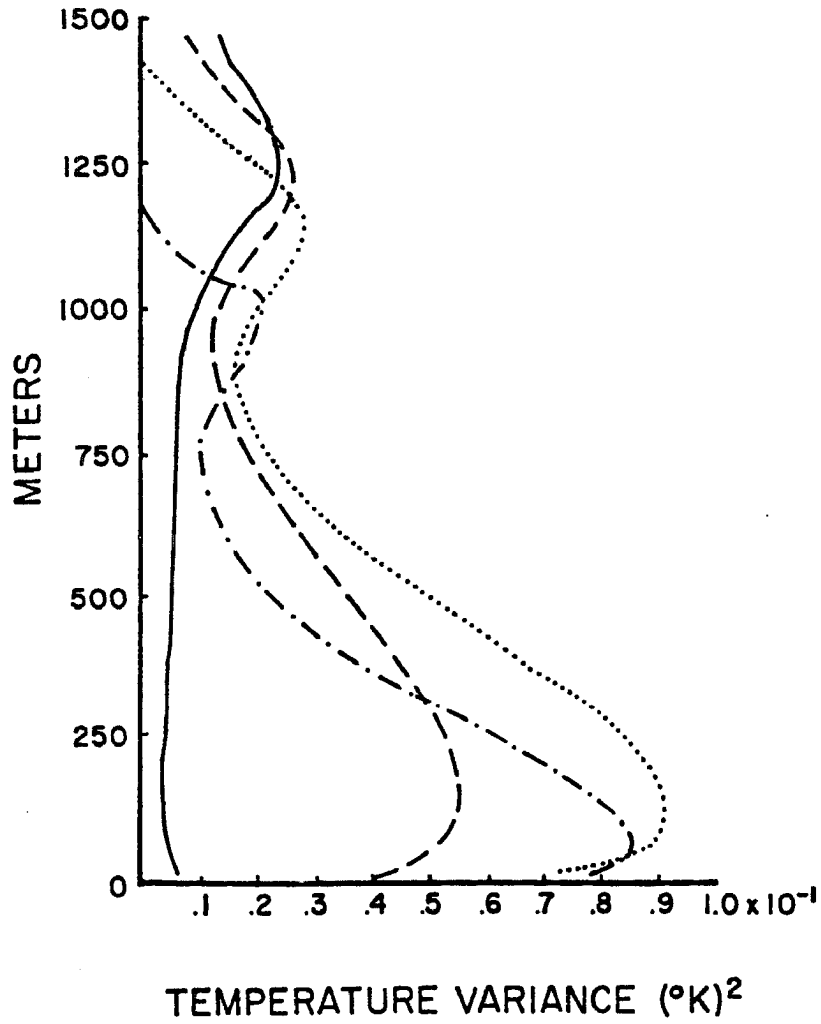


Figure 4-24. Computed profiles of temperature variance, $\theta''\theta''$ at T=5 hours (dash-dot), T=8 hours (dotted), T=10 hours (dashed) and T=11 hours (solid).

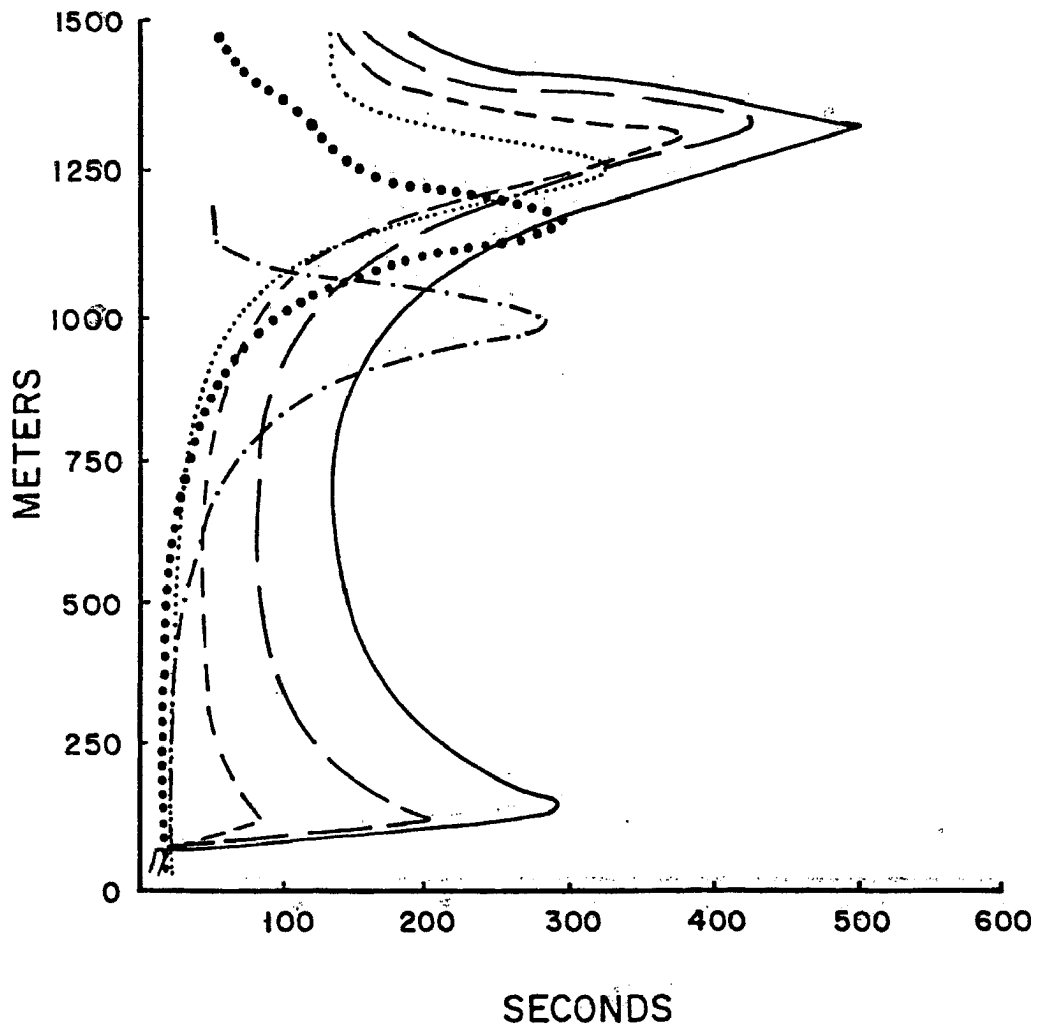


Figure 4-25. Computed profiles of the turbulent time scale at T=5 hours (dash-dot), T=8 hours (bold-dot), T=10 hours (small-dot) T=11 hours (short-dashed), T=12 hours (long-dashed) and T=14 hours (solid).

4.3.4 Comparison with Observations and Other Simulation Studies

The mean profiles of temperature and momentum are seen to agree reasonably well with the observed profiles shown in Figure 4-11.

The temperature profiles in the well mixed layer are progressively cooler than the observed during the course of the daytime heating but this can possibly be explained as a cumulative results of three causes. These causes are: (1) numerical error; (2) insufficient entrainment at the inversion and (3) insufficient surface heat flux.

- (1) Numerical error: Budget calculations show that the total integrated heating of the layer after approximately 5 hours of integration is approximately 4% less than the time integral of the surface heat flux. This 4% difference accounts for an average mean θ difference of close to $-.13^{\circ}\text{K}$ over a depth of 1200m. This possibly can explain 20% of the underpredicted layer heating at 1500L.
- (2) Insufficient entrainment: The unreasonable small values of downward heat flux at the inversion would lead to a definite underprediction of the well-mixed layer heating rate. However, it is not really possible to separate this problem from that of insufficient surface heat flux in arriving at a numerical estimate.
- (3) Insufficient surface heat flux: As stated in (2) above, before a reasonable estimate of insufficient surface heat flux can be made, it is necessary to properly simulate the downward entrainment of heat across the inversion. Estimates of downward heat flux at the inversion range from 10% to 20% of the surface heat flux. This model predicts the magnitude of the downward heat flux, at a maximum, to be only 2.6% of the magnitude of the surface value. Calculations show, however, that to obtain the additional heating necessary to bring the predicted $\bar{\theta}$ profile in line with the observed $\bar{\theta}$ profiles in the well-mixed layer, an additional $3\text{cm}\cdot\text{sec}^{-1}\cdot^{\circ}\text{K}$ over six hours is necessary. An increase in the downward heat flux from 3% to approximately 20% of the surface value would supply about an additional $1.7\text{cm}\cdot\text{sec}^{-1}\cdot^{\circ}\text{K}$ over 8 hours - approximately 75% of the necessary heat input. Therefore, increased surface heat flux is probably necessary, even with proper modeling of entrainment dynamics, to provide the necessary heat input in order to bring the computed profiles up to the observed profiles.

Figure 4-26 shows a time plot of surface heat flux for Day 33 computed from observed data (the 1-2m temperature difference) and an

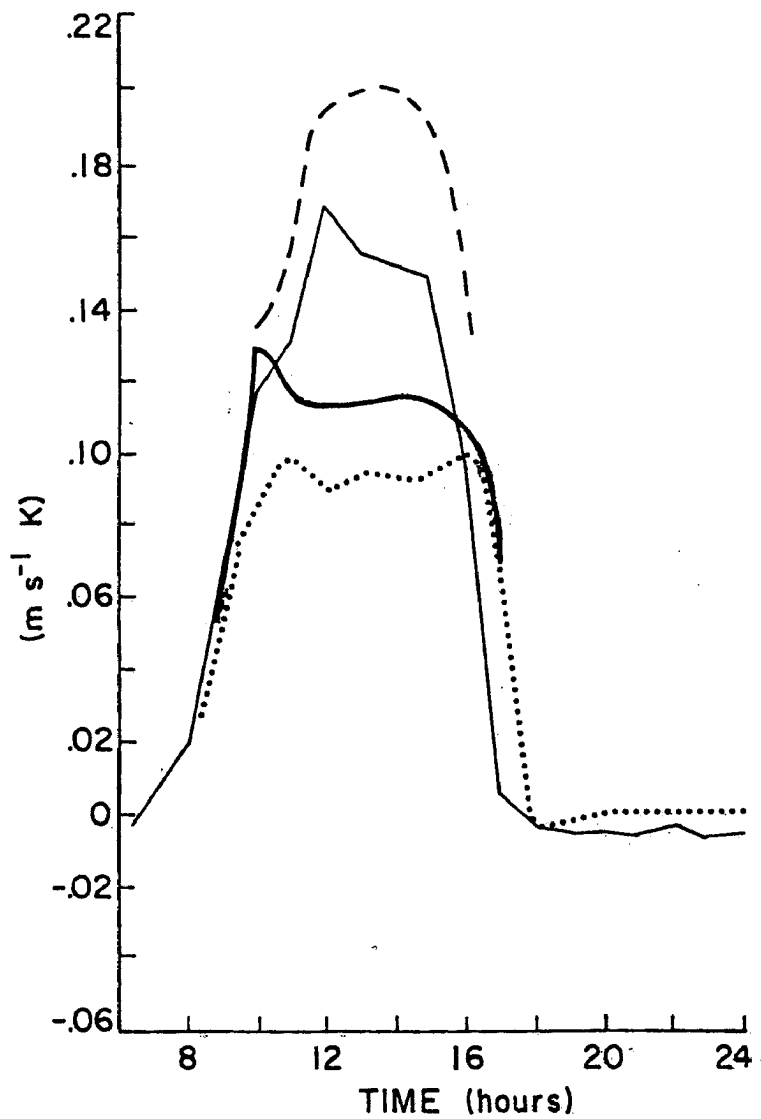


Figure 4-26. Hourly variation of the computed and observed surface heat flux as a function of time of Day 33 (dash-line), Deardorff (1974) (thin solid line), observed; (dotted), Yamada and Mellor (1975); and (bold-solid line), this study.

empirical temperature profile proposed by Businger et. al. 1971, (see Yamada and Mellor, 1975). Also shown are the surface heat flux as computed by Yamada and Mellor (1975), Deardorff (1974) and this study. As is seen this study falls in between the other two but still below the computed rate. However, it must be noted that the computed values are calculated for $z = 1.5\text{m}$, using the hypothesis of a constant flux surface layer. Model values are at $z = 25\text{m}$ also using a constant flux surface layer hypothesis. Since the model assumes a much deeper constant flux surface layer, 50m vs 2m , it is conceivable that the values are not inconsistent. Comparison of the surface heat flux with that of Wyngaard and Cote (1974) is not applicable, since they externally specified the surface heat flux.

Both Wyngaard and Cote (1974) and Deardorff (1974a) have published profiles of mean virtual potential temperature. The results of this model compare qualitatively quite well with both studies. The major discrepancy is in the amount of the heating seen to occur in the layer itself. This however, can be directly related to the substantially greater amount of surface heat flux generated in the Deardorff model. It is interesting to note that Wyngaard and Cote, even with inclusion of the buoyancy in the parameterization of the pressure-temperature correlations, were not able to eliminate the tendency toward stability near the surface in the θ profiles. This suggests that the problem is more complex than stated in section 2.3.2.

Further experimentation with this model has shown that the surface stability feature is not properly interpreted as a slight underprediction of the surface heat flux as a boundary condition on the predicted flux profiles, as Figure 4-20 might suggest. On the contrary large values of

surface heat flux ($\sim 30\text{cm}\cdot\text{sec}^{-1}\cdot\text{K}$) tend to enhance the prominence of this stability feature in the mean $\bar{\theta}$ profiles. This conclusion tends to support the reasoning of Wyngaard and Cote as given in section 2.3.2. Conversely lower magnitudes of surface heat flux tend to eliminate the stability feature. Profiles of heat flux from Wyngaard and Cote and Deardorff do not display the strong tendency to change their slope near the surface in the afternoon but maintain a nearly constant z -derivative. Yet in the case of Wyngaard and Cote, their profiles of mean θ still show the tendency toward slight stability near the surface, which seems somewhat inconsistent with their flux profiles. It's possible that the stability feature is due to a lower boundary problem with the θ -variance profiles.

At the inversion, both Deardorff and Wyngaard and Cote show substantially larger values (greater than 10% of the surface value) of downward heat flux, than does this simulation. Physically, this downward heat flux can be related to the "overshoot" of convective thermals into the strongly stratified atmosphere capping the well mixed layer. In the absence of explicit prediction for w'' , the appearance of this region of negative heat flux is due entirely to the turbulent transport terms: $\overline{w'' u_1'' u_j''}$, $\overline{w'' u_j'' \theta''}$ and $\overline{w'' \theta'' \theta''}$. These terms are modeled (see section 2.3.3) by a simple diffusion of turbulent kinetic energy or variance, with an effective diffusivity of $q^2 T$. Yamada and Mellor (1974) use an almost identical formulation for the turbulent transport term in their predictive equation for q^2 ; and their results show at most a downward heat flux of only 2% of the surface heat flux. This formulation leads to linearly decreasing profiles of momentum variance above the inversion, which this author believes to be

unrealistic. Further, artificially enhancing the diffusion by increasing the diffusion coefficient does not lead to the desired result (i.e., greater downward heat flux) but smears the inversion, rather than sharpens it as would be hoped. Clearly then the turbulent diffusion parameterization is adequate in this situation. There is also the strong implication that the diffusive model is inadequate whenever the energy transport is by the energy containing eddies. Zeman and Lumley (1976) assert that the simple gradient model for the turbulent transport terms predicts (1) a downward energy flux in the lower half of the boundary layer when in reality all the energy is fluxed upward and (2) a subdued entrainment activity and unrealistically small values of the downward heat flux at the inversion. They further conclude that the buoyancy-turbulence interaction couples the energy flux to the gradients of the vertical heat flux and temperature variance and permits counter-gradient transport of turbulent kinetic energy.

Yamada and Mellor (1975) using a level 3 model, described by Mellor and Yamada (1974), performed numerical simulation experiments on Days 33 and 34 of the Wangara Experiment. Beginning at 0900L on Day 33 they performed a 48 hour integration using time varying vertical profiles of geostrophic wind and were able to simulate with surprising accuracy the development of the observed nocturnal jet described in section 4.2.1. In contrast a similar experiment, Case B, described by the same authors, basically identical except the geostrophic wind was held as a constant showed a somewhat similar development in the mean wind except that a strong maximum was seen to develop in the free atmosphere above the inversion rather than in the well-mixed layer. Results with this model show good qualitative agreement with

the above mentioned, Case B. Therefore, this author has tentatively concluded like Yamada and Mellor, that accurate data on both the time varying structure and the thermal wind structure need to be specified to accurately simulate the mean wind structure. The attempt to be less specific can lead to strong spurious inertial oscillations. Hence the strong shear zone across the inversion seen in Figures 4-17 and 4-18 cannot be assumed to be realistic, but more probably due to different magnitudes in the inertial oscillation above and below the inversion.

5. SUMMARY AND CONCLUSIONS

5.1 Summary and Conclusions

The objective of this research is an evaluation of the Manton-Cotton theory of convective parameterization. The evaluation has been done using the framework of a dry horizontally-homogeneous planetary boundary layer, with and without convective forcing. Day 33 of the Wangara Experiment was chosen for the simulation study for two reasons:

- (1) it provides an observed data set meeting as closely as possible, the model assumptions of a dry horizontally homogeneous convectively driven planetary boundary layer, to which to compare simulated profiles; and
- (2) direct comparisons can be made with simulation studies by other authors who have used similar but not identical formulations.

Lower boundary conditions for the model are determined with the model-derived Manton-Cotton surface layer parameterization. The model was forced with measured time varying profiles of surface temperature. The geostrophic wind components u_g and v_g and the surface roughness height were introduced into the model as externally specified constants.

Results show that the model simulated quite well the development of the buoyancy driven planetary boundary layer on Day 33 during the daylight heating. With the onset of the evening, the decoupling of the well mixed layer from the surface and the beginning of the development of a nocturnal jet was also simulated. Profiles of momentum in the mixed layer are seen to be well mixed with almost complete de-coupling from the surface after sunset.

The decoupling was accomplished by the onset of the radiational cooling of the surface and the subsequent development of a shallow

surface-based stable layer. Fluxes of heat and momentum in the surface layer became negligible after sunset.

The dynamics of entrainment at the inversion were modeled poorly as evidenced by values of $-\overline{\theta''w''}_i / \overline{\theta''w''}_{sfc}$ of approximately 0.03.

In the absence of surface heating, model results resembled the traditional Ekman spiral. Surface stress, surface wind direction and surface wind were seen to fluctuate with a period of approximate $2\pi/f$, where f is the coriolis parameter, $2\Omega\sin\phi$. The magnitude of column averaged turbulent kinetic energy; surface stress, $\rho_0 u_*^2$; and frictional turning of the surface were seen to vary directly with the surface roughness parameter, z_0 . The degree of frictional turning was seen to agree reasonably well with that observed by Gray (1972) and Mendenhall (1967) from statistical analysis of large data sets. The degree of frictional turning was a factor of 3 less than that predicted by traditional first order modeling techniques.

The lack of a good first order dynamical model has led to the attempt to formulate a model at higher orders. The overall results of this evaluation, has led this author to conclude that the ensemble-averaged second-moment time-dependent model provides a powerful tool for describing the effect of turbulence on the mean vertical structure of the atmosphere. This method is not only viable but the statistical interpretation and dynamic modeling of the effects of buoyancy generated turbulence in the energy containing range is a valid attempt to dynamically simulate vertical transport and mixing in the atmosphere. Overall model results support this calculation.

Specific conclusions can be drawn concerning the modeling of the higher-order moments:

- (1) The simple diffusion model for the turbulent transport terms (the triple correlation products) is clearly inadequate. The maintenance of the shallow entraining layer at the top of the well-mixed layer is clearly a dynamically complex process and the vertical eddy transport of eddy momentum flux, eddy heat flux and eddy kinetic energy plays a major role. Further, this model predicts a downward turbulent flux of turbulence in the lower third of the well-mixed layer and a downward flux of temperature variance in the upper half, when in reality all transports are upward. In the extension of this model to convective parameterization through the depth of the troposphere, one can expect turbulent transport of eddy heat and momentum flux to be even more important. Hence inadequacy of the closure model suggests that it will be deficient in its extension to the more general task.
- (2) The model predicts realistic eddy flux profiles in the atmosphere, which couple very well with the values determined by the surface-layer scheme. However, profiles of variance do not. This result suggests that the equilibrium assumption in the surface-layer parameterization scheme is at least inconsistent with the assumption of the planetary boundary layer model or might even be invalid.
- (3) The calibration of the closure coefficients using surface layer observations leads to serious errors and inconsistencies. The extension of the surface layer calibration to the well mixed layer above was designed to be accomplished by the turbulent time scale. Figures 4-25 shows that in the presence of active convection, the time scale is essentially constant with height out of the surface layer into the well mixed layer above. This is due to the formulation of the time scale. Therefore, if dissipation and diffusion, as calibrated in the surface layer, are too great for the well-mixed layer above, then this formulation of the time scale does not account for such a difference as intended.

5.2 Suggestions for Further Research

The results of Wyngaard and Cote (1974), and later work by Zeman and Lumley (1975) lend direction to further research effort on the Manton-Cotton model. Specifically, this should be in two steps:

- (1) the inclusion of a buoyancy dependent term in the modeling of pressure-correlation terms; and
- (2) an expanded model for the turbulent transport of the variances and covariances. The work of Zeman and Lumley can serve as a guide for this effort.

Alternate formulations for the time-scale should be explored; from both the context of computational stability and physical modeling.

Serious thought should be given the validity of the equilibrium assumption used in the formulation of the surface layer parameterization. The surface layer, being a net exporter of turbulent kinetic energy, should be tied to the layer above by an additional means other than the gradients of mean temperature and momentum.

REFERENCES

- Arakawa, A., and W. H. Schubert, 1974: Interaction of a cumulus cloud ensemble with the large-scale environment, PART I, J. Atmos. Sci., 31, 674-701.
- Ball, F. K., 1960: Control of inversion height by surface heating, Quart. J. Roy. Meteor. Soc., 86, 483-494.
- Betts, A. K., 1973: Non-precipitating cumulus convection and its parameterization, Quart. J. Roy. Meteor. Soc., 99, 178-196.
- Blackadar, A.K., 1957: Boundary layer wind maxima and their significance for the growth of nocturnal inversions, Bull. Amer. Meteor. Soc., 38, 283-290.
- Businger, J. A., J. C. Wyngaard, Y. Izumi, and E. F. Bradley, 1971: Flux profile relationships in the atmospheric surface layer, J. Atmos. Sci., 28, 189-191.
- Carl, D. M., T. C. Tarbell and H. A. Panofsky, 1973: Profiles of wind and temperature from towers over homogeneous terrain, J. Atmos. Sci., 30, 788-794.
- Carson, D. J., 1973: The development of a dry, inversion-capped, convectively unstable boundary layer, Quart. J. Roy. Meteor. Soc., 99, 450-467.
- Clarke, R. H., A. J. Dyer, R. R. Brook, D. G. Reid and A. J. Troup, 1971: The Wangara Experiment: Boundary Layer Data, Tech. Paper No. 19, Div. of Meteor. Phy., Commonwealth Scientific and Industrial Research Organization, Melbourne, Australia, 350 pp.
- Cotton, W. R., 1975a: Theoretical cumulus dynamics, Rev. of Geo. and Spa. Phy., 13, 419-447.
- _____, 1975b: On parameterization of turbulent transport in cumulus clouds, J. Atmos. Sci., 32, 548-564.
- _____, 1975c: Modeling of convective storms, Proceedings of SESAME Opening Meeting, Boulder, Colorado, prepared by NOAA, ERL, Boulder Colorado 80203.
- Daly, B. J., and F. H. Harlow, 1970: Transport equations in turbulence, Phys. Fluids, 16, 157-158.
- Deardorff, J. W., 1969: A numerical study of three-dimensional turbulent channel flow at large Reynolds numbers, J. Fluid. Mech., 41, Part 2, 453-480.
- _____, 1974a: Three dimensional numerical study of the height and structure of a heated planetary boundary layer, Boundary-Layer Meteor., 7, 81-106.

REFERENCES (cont'd)

- Deardorff, J. W., 1974b: Three dimensional numerical study of turbulence in an entraining mixed layer, Boundary-Layer Meteor., 7, 199-226.
- _____, G. E. Willis, and D. K. Lilly, 1969: Laboratory investigation of non-steady penetrative convection, J. Fluid Mech., 35, 7-31.
- Donaldson, C. DuP., 1972: Calculation of turbulent shear flow for atmospheric and vortex motions, AIAA, 10, 4-12.
- _____, 1973: Construction of a dynamic model of the production of atmospheric turbulence and the dispersal of atmospheric pollutants, Workshop on Micrometeorology, Amer. Meteor. Soc., 313-392.
- Dutton, J. A., 1976: The Ceaseless Wind. An Introduction to the Theory of Atmospheric Motion, McGraw-Hill Inc., New York, N.Y. 579, pp.
- _____, and G. H. Fichtl, 1969: Approximate equations of motion for gases and liquids, J. Atmos. Sci., 26, 241-254.
- Gray, William M., 1972: A diagnostic study of the planetary boundary layer over the oceans, Atmos. Sci. paper, No. 179, Dept. of Atmos. Sci., Colorado State University, Fort Collins, Colorado 80523.
- Haltiner, G. J., 1971: Numerical Weather Prediction, John Wiley and Sons, Inc., New York, N.Y., 317 pp.
- Hanjalic, K., and B. E. Launder, 1972: Fully developed asymmetric flow in a plane channel, J. Fluid Mech., 52, 609-638.
- Hess, G. D., and R. H. Clarke, 1973: Time spectra and cross-spectra of kinetic energy in planetary boundary layer, Quart. J. Roy. Meteor. Soc., 99, 130-153.
- Klebanoff, P. S., 1955: Characteristics of turbulence in a boundary layer with zero pressure gradient, NCAR Report 1247.
- Lenschow, D. H., 1974: Model of the height variation of the turbulent kinetic energy budget in the unstable planetary boundary layer, J. Atmos. Sci., 31, 465-474.
- Lewellen, W. S., and M. Teske, 1973: Prediction of the Monin-Obukhov similarity functions from an invariant model of turbulence, J. Atmos. Sci., 30, 1340-1345.
- _____, and _____, 1976: Second-order closure modeling of diffusion in the atmospheric boundary layer, Boundary-Layer Meteor., 10, 69-90.

REFERENCES (cont'd)

- Lilly, D. K., 1968: Models of cloud topped mixed layers under a strong inversion, Quart. J. Roy. Meteor. Soc., 94, 292-309.
- Lipps, F. B., 1977: A study of turbulence parameterization in a cloud model, J. Atmos. Sci., 34, 1751-1772.
- Lumley, J. L., and B. Khajeh-Nouri, 1974: Computational modeling of turbulent transport, Proc. Second IUTAM-IUGG Symposium Turbulent Diffusion in Environmental Pollution, Charlottesville, VA., Advances in Geophysics, 18A, 169-192.
- Mahrt, L., and D. H. Lenschow, 1976: Growth dynamics of the convectively mixed layer, J. Atmos. Sci., 33, 41-51.
- Manton, M. J., and W. R. Cotton, 1977a: Parameterization of the atmospheric surface layer, J. Atmos. Sci., 34, 331-334.
- _____, and _____, 1977b: Formulation of the approximate equations for modeling moist deep convection on the mesoscale, Atmos. Sci. paper No. 266, Department of Atmospheric Science, Colorado State University, Fort Collins, Colorado 80523.
- Matsuno, T., 1966: A finite difference scheme for time integrations of oscillatory equations with second-order accuracy and sharp cut off for high frequency, J. Meteor. Soc., Japan, 44, 86-88.
- Mellor, G. L., 1973: Analytic prediction of the properties of stratified planetary surface layers, J. Atmos. Sci., 30, 1061-1069.
- _____, and T. Yamada, 1974: A hierarchy of turbulence closure models for the planetary boundary layer, J. Atmos. Sci., 31, 1791-1806.
- Mendenhall, B. R., 1967: A statistical study of frictional wind veering in the planetary boundary layer, Atmos. Sci. paper No. 116, Department of Atmospheric Science, Colorado State University, Fort Collins, Colorado 80523.
- Monin, A. S., and A. M. Yaglom, 1973: Statistical Fluid Mechanics, Vol. 1, the M.I.T. Press, 769 pp.
- Ng, K. H., and D. B. Spaulding, 1972: Turbulence model for boundary layers near walls, Phy. Fluids, 15, 20-30.
- Ogura, Y., and N. A. Philips, 1962: Scale analysis of deep and shallow convection in the atmosphere, J. Atmos. Sci., 19, 173-179.
- Ooyama, K., 1971: A theory on parameterization of cumulus convection, J. Meteor. Soc. Japan, 46, 178-201.

REFERENCES (cont'd)

- Paulson, C. A., 1970: The mathematical representation of wind speed and temperature profiles in the unstable atmosphere, J. Appl. Meteor., 9, 857-861.
- Pielke, R. A., 1974: A three dimensional numerical model of the sea breezes, Mon. Wea. Rev., 102, 115-139.
- _____, and Maher, Y., 1975: Representation of the heated planetary boundary layer in mesoscale models with coarse vertical resolution, J. Atmos. Sci., 32, 2288-2308.
- Rotta, J., 1951: Statistische Theorie Nichthomogener Turbulenz, Z. Phys., 129, 547-572.
- Smagorinsky, J., 1963: General circulation experiments with the primitive equations: Part I, the basic experiment, Mon. Wea. Rev., 91, 99-164.
- So, R. M. C., and G. L. Mellor, 1972: An experimental investigation of turbulent boundary layers along curved surfaces, NASA CR-1940.
- Sommeria, G., 1976: Three-dimensional simulation of turbulent processes in an undistributed trade wind boundary layer, J. Atmos. Sci., 33, 216-241.
- _____, and J. W. Deardorff, 1977: Subgrid-scale condensation in models of non-precipitating clouds, J. Atmos. Sci., 34, 344-355.
- Tennekes, H., 1970: Free convection in the turbulent Ekman layer of the atmosphere, J. Atmos. Sci., 27, 1027-1034.
- _____, and J. L. Lumley, 1972: A First Course in Turbulence, The M.I.T. Press, 300 pp.
- _____, 1973: A model for the dynamics of the inversion above a convective boundary layer, J. Atmos. Sci., 30, 558-567.
- _____, 1978: Turbulent flow in two and three dimensions, Bull. Amer. Meteor. Soc., 59, 22-28.
- Wilson, N. R., and R. H. Shaw, 1977: A higher-order closure model for canopy flow, J. Appl. Meteor., 16, 1197-1205.
- Wyngaard, J. C., O. R. Cote, and Y. Izumi, 1971: Local free convection, similarity, and the budgets of shear stress and heat flux, J. Atmos. Sci., 28, 1171-1182.
- _____, and _____, 1974: The evolution of a convective planetary boundary layer - A higher order closure model study, Boundary-Layer Meteor., 7, 289-308.

REFERENCES (cont'd)

- _____, _____, and K. S. Rao, 1974: Modeling the atmospheric boundary layer, Proceedings Second IUTAM-IUGG Symposium on Turbulent Diffusion in Environmental Pollution, Charlottesville, VA., Advances in Geophysics, 18A 193-212.
- Yamada, T., and G. L. Mellor, 1975: A simulation of the Wangara atmospheric boundary layer data, J. Atmos. Sci., 32, 2309-2329.
- Zeman, O., and J. L. Lumley, 1976: Modeling buoyancy driven mixed layers, J. Atmos. Sci., 33, 1974-1988.
- _____, and H. Tennekes, 1977: Parameterization of the turbulent energy budget at the top of the daytime atmospheric boundary layer, J. Atmos. Sci., 34, 111-123.
- Zilitinkevich, S. S., 1970: Dynamics of the Atmospheric Boundary Layer, Hydro-meteorological Publishing House, Leningrad, 291 pp.

APPENDIX A

The Manton-Cotton surface layer parameterization.

Given: u^* and H

$\zeta = z/L$; $L =$ the Monin-Obukhov length.

$z = ZT(1)$, the effective model height of the surface layer.

Define:

$\eta = \zeta/\phi_m(\zeta)$, where ϕ_m is the Businger-Dyer equation for momentum.

$$\psi^2 = \frac{(1-3.21\eta)(1-2.18\eta)}{(1-2.86\eta)}$$

$$\phi = .74(1-2.18\eta)/1(1-2.86\eta)$$

$$Q^* = \frac{2(1-\eta)}{\psi} a_1$$

$$a_1 = \frac{2b_1}{(2+3b_1^2)}$$

$$b_1 = 1.69$$

then:

$$\overline{v''v''} = a' \cdot Q^{*2} \cdot u^*, \text{ where } a' = \frac{1}{3}(1 - \frac{a_1}{b_1})$$

$$\overline{u''u''} = \overline{v''v''} + \frac{2u^{*2}}{\psi b_1}$$

$$\overline{w''w''} = \overline{v''v''} - \frac{2 \cdot \eta \cdot u^{*2}}{\psi b_1}$$

$$\overline{\theta''\theta''} = \frac{2H^2}{\psi a_2 u^{*2}}, \quad a_2 = 0.78$$

$$\overline{\theta''u''} = \frac{H(1+\phi)}{\psi b_2}, \quad b_2 = 1.25$$

APPENDIX B

Businger-Dyer profile for heat:

$$\phi_h = \begin{cases} 0.74 + 4.7\zeta & \zeta \geq 0 \\ \frac{.74}{\sqrt{1-9\zeta}} & \zeta < 0 \end{cases}$$

momentum:

$$\phi_m = \begin{cases} 0.47 (-\zeta)^{-1/3} & \zeta \leq -0.5 \\ (1-15\zeta)^{-1/4} & -.05 < \zeta \leq 0 \\ 1+4.76\zeta & \zeta > 0 \end{cases}$$

Paulson Equations for:

momentum:

$$\psi_M = \begin{cases} 21\ln\left(\frac{1+x}{2}\right) + \ln\left(\frac{1+x^2}{2}\right) - 2\tan^{-1}(x) + \pi/2 \\ \text{where } x = (1-15\zeta)^{1/4}, \zeta \leq 0 \\ -4.7\zeta, \zeta > 0 \end{cases}$$

heat:

$$\psi_H = \begin{cases} 21\ln\left(\frac{1+x}{2}\right), \text{ where } x = \sqrt{1-9\zeta}, \zeta \leq 0 \\ -6.35\zeta, \zeta > 0 \end{cases}$$

BIBLIOGRAPHIC DATA SHEET	1. Report No. CSU-ATSP-304	2.	3. Recipient's Accession No.
4. Title and Subtitle An Evaluation of a Second Moment Time Dependent Turbulence Model		5. Report Date December, 1978	
7. Author(s) Frederick Toepfer		6.	
9. Performing Organization Name and Address Department of Atmospheric Science Colorado State University Foothills Campus Fort Collins, Colorado 80523		8. Performing Organization Rept. No. CSU-ATSP-304	
12. Sponsoring Organization Name and Address National Science Foundation 1800 "G" Street N.W. Washington, D.C. 20550		10. Project/Task/Work Unit No.	
15. Supplementary Notes		11. Contract Grant No. NSF Grant ATM 77-09770 NSF Grant DES 75-13310	
16. Abstracts <p>The Manton-Cotton approximate equations governing dry convection are studied. These equations are numerically integrated on a horizontally homogeneous vertical finite difference grid of the planetary boundary layer. The integration is both forced and unforced by a time varying profile of surface temperature for approximately 1/2 of a diurnal cycle. The resulting profiles of mean momentum and temperature, momentum and temperature flux, and momentum and temperature variance are then studied with the dual objective of determining the capability of the model to describe the dry planetary boundary layer and to evaluate its intended objective of modelling deep tropospheric convection in a mesoscale model. Model results in the forced case are compared with observations from Day 33 of the Wangara Experiment.</p> <p>Results suggest that the model does well in describing the dry planetary boundary layer, in spite of apparent inadequacies in the formulation of the unified closure assumption employing a turbulent time scale. The rate of entrainment of the inversion is underpredicted by an order of magnitude. Flux profiles couple nicely with those diagnosed by the surface layer parameterization scheme. Profiles of variance suggest that the local equilibrium assumption for the surface layer scheme may be invalid. Overall model results suggest the need for including buoyancy in the closure approximation for the turbulent transport triple correlation products prior to extending the model to deep tropospheric convection.</p>		13. Type of Report & Period Covered Master's Thesis	
17. Key words and Document Analysis. 17a. Descriptors Planetary Boundary Layer Turbulence Model Higher-order Modelling Higher-order Time Dependency		14.	
18. Availability Statement		19. Security Classification Report CONFIDENTIAL X	20. No. of Pages 99
17c. COSATI Field/Code		21. No. of Pages	